Toward Deployable Origami Continuum Robot: Sensing, Planning, and Actuation

A DISSERTATION PRESENTED
BY
JUNIUS SANTOSO
TO
THE ROBOTICS ENGINEERING PROGRAM

IN PARTIAL FULFILLMENT OF THE REQUIREMENTS
FOR THE DEGREE OF
DOCTOR OF PHILOSOPHY
IN THE SUBJECT OF
ROBOTICS ENGINEERING

WORCESTER POLYTECHNIC INSTITUTE
WORCESTER, MASSACHUSETTS
NOVEMBER 2019

Approved by:

_____
Prof. Cagdas D. Onal, Advisor, Worcester Polytechnic Institute (WPI)

_____
Prof. Jing Xiao, Committee Member, Worcester Polytechnic Institute (WPI)

_____
Prof. Loris Fichera, Committee Member, Worcester Polytechnic Institute (WPI)

_____
Prof. Jamie Paik, Committee Member, École polytechnique fédérale de Lausanne (EPFL)

Thesis advisor: Professor Cagdas D. Onal Junius Santoso

Toward Deployable Origami Continuum Robot: Sensing, Planning, and Actuation

Abstract

Continuum manipulators which are robot limbs inspired by trunks, snakes, and tentacles, represent a promising field in robotic manipulation research. They are well known for their compliance, as they can conform to the shape of objects they interact with. Furthermore, they also benefit from improved dexterity and reduced weight compared to traditional rigid manipulators. The current state of the art continuum robots typically consists of a bulky pneumatic or tendon-driven actuation system at the base, hindering their scalability. Additionally, they tend to sag due to their own weight and are weak in the torsional direction, limiting their performance under external load. This work presents an origami-inspired cable-driven continuum manipulator module that offers low-cost, light-weight, and is inherently safe for human-robot interaction. This dissertation includes contributions in the design of the modular and torsionally strong continuum robot, the motion planning and control of the system, and finally the embedded sensing to close the loop providing robust feedback.

Contents

List of Figures

List of Tables

List of Symbols

$(\mathbf{A})^{\vee}$ Operator to construct a 3×1 vector from non-zero elements of a skew symmetric matrix $\mathbf{A}$

α Offset angle

β Maximum bending angle

ε_{λ} A number to quantify the size of the singular region

ε_{dz} Small dead-zone around zero for bending plane direction measurement

γ Bending rate

κ Module curvature

$\kappa_i(t)$ Instantaneous curvature of i^{th} module

κ_{max} Maximum module curvature

κ_{mi} m^{th} module's curvature when transitioning from desired i^{th} to $(i+1)^{th}$ path segments

λ_{damp} Damping coefficient for damped least-squares Jacobian

λ_{max} Upper limit on λ

λ_{path} Scaling factor for e_{path}

λ_{tip} Scaling factor for e_{tip}

$\mathbf{\Theta_n}$ Robot tip rotation matrix in $SO(3)$

$\mathbf{I}$ Identity matrix

$\mathbf{J'}$ Jacobian transpose

$\mathbf{J^{\omega}}$ Rotational component of Jacobian matrix

$\mathbf{J^{v}}$ Linear component of Jacobian matrix

$\mathbf{J_{damped}}$ Damped least-squares Jacobian

$\mathbf{J}$ Full Jacobian in $\Re^{6\times 3n}$ for n-module robot

$\mathbf{T}_{\mathbf{n}}^{\mathbf{n}+1}$ Homogenous transformation matrix from n^{th} to $(n+1)^{th}$ frames

ω Angular velocities of the bending plane orientation

φ Bending plane direction

$\varphi_i(t)$ Instantaneous bending direction of i^{th} module

Φ_n Desired bending direction for the n^{th} path segment

φ_{mi} m^{th} module's bending direction when transitioning from desired i^{th} to $(i+1)^{th}$ path segments

ρ Radius of curvature

σ_{min} Smallest singular value of J obtained from singular value decomposition

$\tau_{resultant}$ The amount of torque can be supported by the actuated base module connected to 3 adjacent modules

$\tau_{torsion}(n)$ Torque applied to the base module for the torsional loading

$\tau_{transverse}(n)$ Torque applied to the base module for the transverse loading

θ Bending angle

$\Theta_n(i,j)$ The i^{th} row and j^{th} column element of matrix $\mathbf{\Theta_n}$

$\vec{\Psi}_n$ Robot tip position vector in $\Re$

$\vec{b_n}$ Base plate normal direction vector

$\vec{e_o}$ Orientation error

$\vec{e_p}$ Position error

$\vec{p_b}$ Base plate position vector

$\vec{p_t}$ Tip plate position vector

$\vec{q_L}$ Vector of tendon length

$\vec{q_L}^i$ Vector of tendon length at i^{th} iteration

$\vec{q_S}$ Vector of arc parameters (s, θ, φ)

$\vec{q_{S_{desired}}}$ Vector of desired arc parameters describing a desired path for the robot

$q_{\vec{Smin}}, q_{\vec{Smax}}$ Vector of minimum and maximum curvature and bending direction

$\vec{t_n}$ Tip plate normal direction vector

B_x, B_y, B_z Magnetic flux strength in X,Y, and Z axis

$D_{,x}$ Partial derivative of D with respect to x

e_{path} Path error

e_{tip} Tip error

g Gravitational acceleration constant

K_n Desired curvature for the n^{th} path segment

L_0 Minimum module/tendon length

l_1, l_2, l_3 Cable lengths solution given by inverse kinematics solver

l_{1c}, l_{2c}, l_{3c} Final cable lengths converted to motor commands

l_{1m}, l_{2m}, l_{3m} Cable lengths obtained through conversion of the measured configuration parameters

L_{bend} Moment arm of the bending base module

$l_{i1\_prev}, l_{i2\_prev}, l_{i3\_prev}$ Tendon lengths for the i^{th} module obtained in previous iteration

l_{i1}, l_{i2}, l_{i3} Tendon lengths for the i^{th} module

L_{max} Length of a fully extended origami module

$l_{payload}$ The moment arm of the payload suspended at the tip of the last (4^{th}) module

m_{mod} Mass of the origami module

$m_{payload}$ Payload mass can be supported by an actuated base module

q_{Lmin}, q_{Lmax} Minimum and maximum tendon lengths

r Distance from the center of the mounting plate to the cable attachment point (module radius)

s Arc length

s_d, θ_d, φ_d Desired arc parameters

S_n Desired arc length for the n^{th} path segment

w_o Scalar weighting for the orientation error term

w_p Scalar weighting for the position error term

This dissertation is dedicated to mom and dad.

Acknowledgments

This work is supported by the National Science Foundation CAREER award program (NSF CMMI-1752195).

I would like to thank my advisor, Professor Cagdas D. Onal, for his mentorship, guidance, and support throughout my doctoral study. I also would like to thank my committee members, Professor Jing Xiao, Loris Fichera, and Jamie Paik for their valuable comments and feedback.

My colleagues at WPI Soft Robotics Laboratory whom I have worked with and had the privilege of knowing. I am grateful to be a part of a knowledgeable and highly motivated group of people.

I would also like to thank my friends, Ann Marie Votta and Binod Giri for their thoughtful comments and feedback on the final draft.

Finally, I would like to thank my beloved family for their patience and unconditional support which makes this culmination of research work possible.

1

Introduction

1.1 Motivations

Traditional robots are typically confined behind the safety cages, but certainly, that is not the case anymore as robotic technology becomes more and more ubiquitous in our daily lives. Early robotic development has improved industrial throughput, especially in the product assembly. However, there is increasing interest in human-robot collaboration as a way to compromise for the currently limited robot capabilities. Industrial sectors hope to benefit from the combined capabilities of human and robots while researchers continue to incrementally improve the latter. Stemming from this, there is a need for a safer robotic platform that will minimize potential threats against fatal injury and loss of life due to unintended robot action.

Soft robots offer a solution for applications in which human presence is crucial for example in a hospital setting. Even though soft robots will never be as strong (with few exceptions such as work in [1]) or as precise as the rigid counterparts, they offer an alternative to offload the high bandwidth computation and sensing normally required in rigid robots. Instead, soft robots rely on their inherent mechanical compliance when exposed to external forces. The challenge then is to create selective and, more ideally, controllable compliance. Soft robots are typically fabricated with rubber materials which are inherently compliant. Pneumatic artificial muscle (PAM) and fluidic elastomer actuator (FEA) are the two common types of soft actuators. The PAM or also known as McKibben muscle is fundamentally consisted of an inflatable elastic tube and a braided mesh that provides a radial constraint. Due to the radial constraint and incompressibility of the (rubber) tube then it is expected that the PAM actuators will undergo elongation or contraction when inflated. On the other hand, FEA consists of a molded air chamber made of rubber and an inextensible constraint layer to achieve the bending motion. Other motion primitives such as extending, contracting, and twisting are also possible depending on the actuator design.

Although pneumatically driven soft robots are inherently safe and capable of providing strong actuation force (proportional to the operating pressure), they are limited by the additional required hardware (e.g. air compressor, pressure regulators, and valves) which are typically bulky. It is also well known that pneumatically driven soft robots are prone to the rupture problem when exposed to sharp objects. In fact, there are research efforts that try to explore the self-healing capabilities of soft robots [2,3]. Tendon driven actuators, on the other hand, suffer from low motor efficiency but allow for a lighter and more portable system.

Kinematically redundant robots are advantageous as they allow for avoidance of singularities, joint limits, and obstacles in the environment. Continuum robots, which lack rigid joints and soft robotics is a subset of, are capable of very large deformation. Thus they are highly dexterous compared to traditional rigid robots (Figure 1.1). Instead, they possess elastic backbones providing form

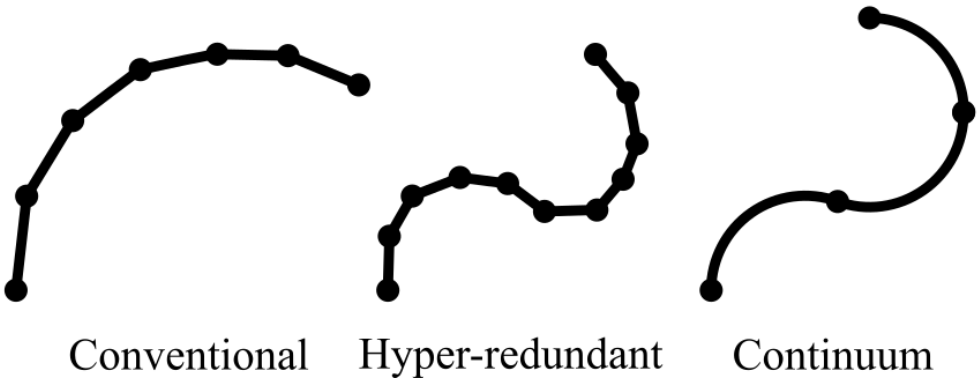

Figure 1.1: Various robotic manipulator types with increasing degrees-of-freedom.

and support. Due to their unique properties, continuum robots have been utilized for various applications ranging from medical surgeries to search and rescue operations. Specifically, continuum robots enable navigation through tortuous paths. Furthermore, their inherent compliance facilitates safe human-robot interaction and collaboration. Tendon and fluid-driven are the two most common actuation methods for continuum robots. Combinations of internal forces generated from pulling tendons or expanding elastic members are responsible for controlling the robot shape through elongation and bending.

Despite numerous continuum robot designs, the current existing continuum robots suffer from excessive twisting due to offset external load. The non-controllable twist is not desirable as it negatively affects the accuracy of the continuum robots. Most research efforts do not attempt to address this even though modeling with the assumption of no torsion is not uncommon[4,5,6,7]. In my best knowledge, the work by Neppalli et al. is the first one that clearly shows a significant twist happening on the continuum robot as shown in Figure 1.2[8]. Research work which attempts to measure the torsional twist of a concentric-tube robot exists and is presented in[9], but no attempt to mitigate the effect of twist directly. On the other hand, continuum robots that appear capable of handling the twist are significantly heavier.

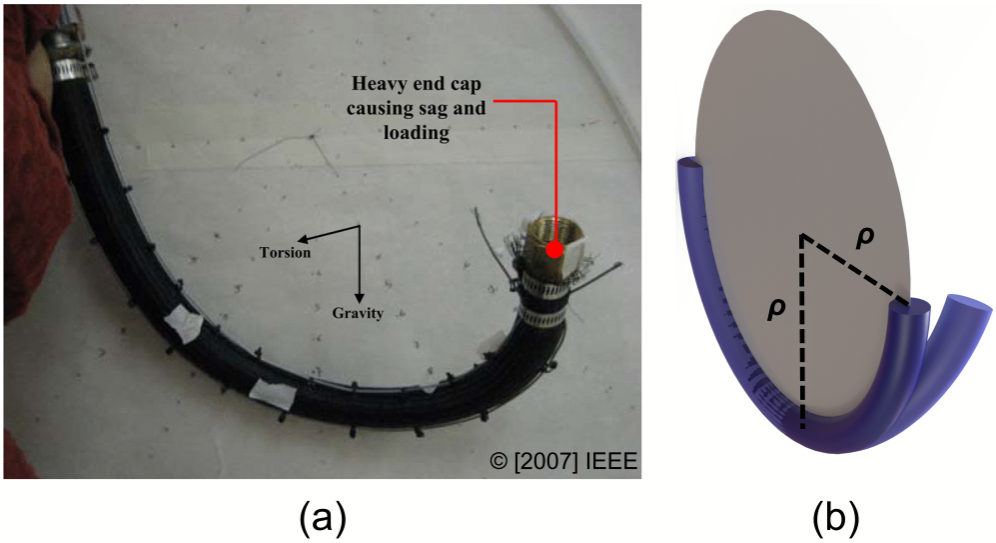

Figure 1.2: (a) The research work by Neppalli et al.[8] which first highlights the problem of twisting on continuum robots caused by an offset load. (b) A continuum section twisting out of plane due to torsional load thus affecting its accuracy.

Octopus arms and elephant trunks are remarkable examples of very capable animal appendages. They can actively control the stiffness of their arms and trunks by utilizing muscular hydrostat. The muscular structure is composed of 3 different muscle groups: longitudinal, transversal, and oblique. The longitudinal and transversal groups are responsible for the appendage's elongation and contraction while the torsional stiffness is actively controlled using the oblique muscles[10]. Drawing the inspiration from the muscular structure, several researchers have designed soft actuators that are capable of providing actuation in torsional direction[11,12,13]. However, it is unclear if the actuators are also capable of providing bending motion, hence limiting their potential as an actuator for continuum robots. In contrast, we utilize an origami structure capable of compression and bending while also passively-resisting torsion.

Additionally, the majority of continuum robots employ a centralized structure so scalability is not straightforward, while this work's modular approach helps to overcome that bottleneck. Modularity can also improve the robustness of the system against failure, which is beneficial (for a deploy-

able system). Portable and deployable robotic platforms are essential to demonstrate the robots' full potential outside of laboratory settings. This goal is attainable by the integration of highly efficient actuators, light-weight and fast control software, and embedded sensing. Highly efficient actuators are important to allow for a longer duration of the robot operation given a limited power source. Light-weight and fast control software is necessary to reduce the computational power needed by the robot's computer. Lastly, embedded sensing would allow the robot to sense its internal state without depending on the typically stationary sensor infrastructure in the laboratory environment.

Sensorization of continuum robots is challenging and still an active research effort due to the absence of discrete mechanical joints at which measurement can easily be made as in traditional rigid robots. This challenge is further complicated for the continuum robots that are capable of significant extension or compression. A common sensing technique such as resistivity measurement may not be suitable anymore as it typically works only in a small range of mechanical deformation (strain). Similarly to other robots, continuum robots would benefit from having sensors to compensate for errors in the system model, achieving more accurate behavior.

The motivations of this dissertation work can be summarized as follows:

- There is increasing interest in human-robot collaboration thus requiring a safer robotic platform.
- Continuum robot is a potential solution due to its inherently safe and highly dexterous nature.
- Current continuum robots suffer from excessive twisting due to external load, thus negatively impact their accuracy.
- Highly efficient actuators, light-weight, and fast control software, and embedded sensing are crucial for a fully deployable robotic system.

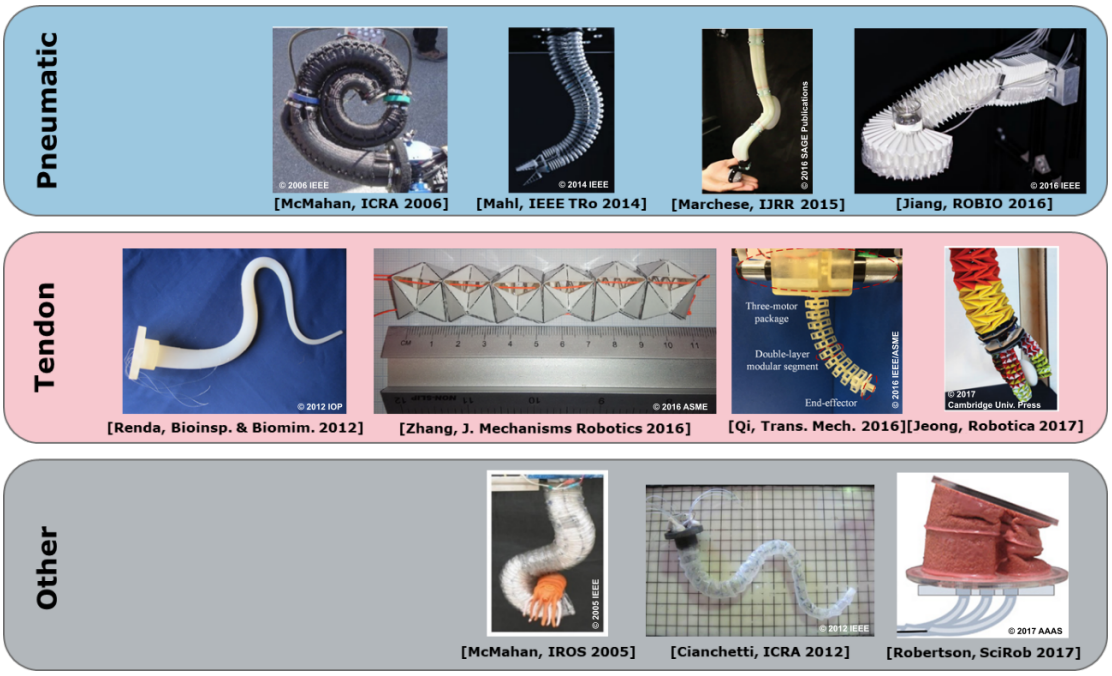

Figure 1.3: Representatives of current state of the art continuum robots. Pneumatic - from left: OctArm[14], Festo Bionic Handling Assistant[15,16,17], a soft spatial fluidic elastomer manipulator[18], Honeycomb Pneumatic Networks (HPN) based continuum robot[19]. Tendon Driven - from left: conically shaped continuum soft robot[20], extensible continuum Robot with integrated origami parallel modules[21], continuum robot with serially connected double-layer planar springs[22], continuum robot arm with twisting tower origami structure[23]. Other/hybrid - from left: Air-Octor[24], shape memory alloy driven continuum robot[25], vacuum-powered soft pneumatic actuator (V-SPA)[26]. Used with permission of IEEE, ASME, SAGE, IOP, AAAS, and Cambridge University Press; permission conveyed through Copyright Clearance Center, Inc.

1.2 Related Work

We list the representatives of the current state of the art for continuum robots in Figure (1.3). The list is not exhaustive by any mean but intended to showcase various continuum robots which are relevant to my work and which I am familiar with. In general, continuum robots are actuated using a pneumatic or a tendon driven system. However, some continuum robots employ other actuation methods such as shape memory alloy (SMA) or vacuum. Ian Walker's group developed an intrinsically and pneumatically actuated continuum robot called OctArm[14]. The OctArm bending

modules are constructed through a parallel arrangement of McKibben actuators. These bending modules are then connected in series to create the three to four-segment continuum robot. Festo Bionic Handling Assistant, on the other hand, is fabricated using the selective laser sintering (SLS) additive manufacturing technique to create a bellow-like structure that is extensible and compliant in bending [15,16,17]. Marchese et al. developed a completely soft continuum manipulator from a low-durometer elastomer [18]. Jiang et al. utilized Honeycomb Pneumatic Networks (HPN) actuator to create a five-segment continuum manipulator [19]. Renda et al. developed a conically shaped soft continuum robot that is made of silicone rubber and is driven with cables [20]. Zhang et al. utilized origami waterbomb parallel structure and steel helical compression springs to create an extensible continuum segment [21]. On the other hand, Qi et al. connected double-layer planar springs in series to create an extensible continuum segment [22]. Jeong et al. developed a continuum arm based on the origami twisting tower structure [23]. The Air-Octor continuum robot developed by McMahan et al. utilized a hybrid pneumatic and tendon actuation system. The compliant body of Air-Octor is constructed from dryer hoses [24]. Cianchetti et al. developed the conically shaped continuum segment that is driven with shape memory alloy (SMA) actuators [25]. Lastly, Robertson et al. developed vacuum-actuated continuum modules (V-SPA) consisted of off-the-shelf foam core and thinly brushed-on layers of silicone rubber [26].

Origami, the Japanese traditional art of paper folding, remarkably allows for the construction of 3-D objects solely from folding patterns on 2-D flat surfaces. It was theoretically proven that any arbitrary 3-D object can be folded from a single sheet of paper [27]. Origami-inspired engineering designs have been utilized in a wide range of fields and scales, from outer space [28] to medical applications [29,30]. Some origami research groups focus on the self-folding [31] and reconfigurable [32,33,34] aspects of origami, while others focus on the creation of compliant mechanisms through origami-inspired designs [35,36]. In the field of robotics, the origami-inspired design has shown to offer benefits in creating self-assemble [37], deployable [38], adaptable [39], impact-resistant and light-weight robots [40,41].

A comprehensive review of origami robots can be found in the work by Rus et al.[42]. The selective compliance in axial and bending directions of an origami-inspired tubular structure, provides necessary behavior of continuum module. This dissertation work focuses on utilizing a well-known origami folding pattern to create a continuum bendable body capable of resisting the torsional load.

1.3 Contributions

To summarize, the goal of this research work is to address the limitations of existing continuum robots and to facilitate a more deployable system. The thesis encompasses all the aspects of a robotic system including actuation, planning, and actuation subsystems. The proposed work aims to make the continuum robot available for field use by using electric actuators instead of pneumatic, incorporating modular design to ease scalability and replacement of broken modules, and developing a proprioceptive sensing methodology to achieve improved control of the robot. Additionally, this work strives to provide a continuum robot platform for different flexible appendage-related research. The contributions can be summarized as follows:

- Torsionally stiff origami continuum modules that are modular and scalable.
- A smoothness preserving inverse kinematics solver.
- A grow-to-shape algorithm for the planning of the robot traversing tortuous path typically challenging for rigid robots.
- Development of a proprioceptive magnetic-based shape sensing suitable for extensible continuum robots.
- Machine learning predictive models to estimate the robot shape parameters.
- Validation of the sensor accuracy both with and without external load.
- A bio-inspired application of the origami modules by the creation of the 3-D origami snake.
- Experimental investigation of transferable simulation-to-real object classification with continuum wraps.

1.4 Thesis Outline

This dissertation is structured as follows, the next chapter will introduce the proposed origami continuum module that is the foundation of this research work. From there, I will discuss the usage of the continuum modules for a general-purpose manipulator application which includes the development of an inverse kinematics solver, feedback control implementation, and grow-to-shape algorithms. Next, I will present the proprioceptive sensing methodology to estimate the robot shape. Lastly, I present two promising applications of the origami robot for locomotion and touch-based object classification. The dissertation is concluded with the summary in the last chapter and accompanied by possible research directions for future work.

2

Origami Module - Initial Work, Design, and Characterization

This chapter is dedicated to the preliminary work necessary for the realization of the origami continuum module. The chapter focuses on the design, fabrication, characterization, and control of a single segment origami continuum robot. Furthermore, the proof-of-concept for the multi-segment continuum manipulator is presented.

The material presented in this chapter is adopted from the following self-authored publication: **J. Santoso**, E. H. Skorina, M. Luo, R. Yan, C. D. Onal, in Proceedings of the 2017 IEEE/RSJ International Conference on Intelligent Robots and Systems (IROS) (IEEE, 2017), pp. 2098–2104.[43]

2.1 Background and Related Work

The field of robotics has recently been gaining momentum and rapidly evolving to be ubiquitous in our daily life. Most of the present robotics applications focus on the effort to tackle dirty, dull, and dangerous jobs for human. However, some applications such as service robotics, medical surgical, and rehabilitation are still heavily dependent on human intervention. In this case, robot should augment human capability instead of completely replacing them. Soft robots have recently showed promising results in minimally invasive surgery [44], rehabilitation [45], explorations and rescue [46]. The potential is attributed from inherent compliance, fault tolerance, and reduced weight. Various capabilities of current soft robots are reviewed in [47,48]. However soft robots are still lacking compared to the rigid robot counterparts in terms of accuracy attributed to the non-linear behavior of the structures or materials.

Continuum robots, inspired by snakes, tentacles, and elephant trunks, have attracted researchers to imitate the remarkable capabilities of the animal counterparts. A continuum robot/manipulator is generally composed of serially connected sections with infinite passive degree-of-freedom, each capable of planar or spatial bending. Recent literature presents continuum manipulators that utilize different actuation methods including pneumatic [14,17,18,49], tendon driven [21,22,50,51], shape-memory-alloy [25,52,53], vacuum [26], and hybrid [24,54]. A comprehensive review of continuum robots can be found in [55].

Continuum robots capable of extraordinary change in length have already existed e.g. OCTOPUS [52] with 41.3 %, Air-Octor [24] with 246.2 %, and up to 25000 % as described in [56]. However it is unclear if those systems are capable to resist torsional load. Torsional resistance is important to mitigate the effect of offset load. Furthermore, majority of the continuum robots utilize a centralized actuation system in contrast with our modular and decentralized approach. Researchers have acknowledged benefits of modularity in soft robots [26,57,58,59]. Modular approach will allow for simpler

control schemes as each module can be controlled independently. Furthermore, since the modules are independent and connected together on a communication bus, they can be scaled up to achieve functional redundancy without modification to the overall system architecture, and failed modules can be easily replaced.

Origami, the paper folding art from Japan, has been a source of inspiration for scientists and engineers alike, ranging from DNA-folding [29] to foldable solar array [28]. Origami allows the construction of complex 3-D objects from planar sheet. In the field of robotics, origami-inspired design has shown to offer benefits in creating self-assemble [37], deployable [38], adaptable [39], impact-resistant and light-weight robots [40,41]. A comprehensive review of origami robots can be found in [42]. Selective compliance in axial and bending directions of an origami-inspired tubular structure, provides necessary behavior of continuum module. To be more specific we can create origami bellows capable to facilitate actuation, while also light weight and torsionally stiff. Our work is most similar with [21] and [51], however it is unclear from those previous work if they can withstand significant torque and no modularity was presented. To the best of our knowledge only the work in [22] reported the measure of torsional stiffness. Furthermore, our origami robot utilize the axial stiffness of the module itself to provide restoring force instead of relying to springs as done in [21].

This research work introduces a new modular cable-driven origami continuum manipulator, combining the three distinct main components previously discussed as shown in Figure 2.1. Each identical module of the manipulator is fully integrated with three electric motors (fully-actuated), encoders, a communication bus, and a microcontroller unit (MCU) with encoder counter chips. The motors provide each module with two bending degrees-of-freedom (DoF) and a single axial DoF, allowing it to expand and retract. Each fully assembled origami module weighs about 110 g, with the motors being the heaviest part. The proposed continuum module is resistant to torsion, a characteristic that helps maintain the module shape under offset loads. When under an offset load, a continuum manipulator with low torsional stiffness would twist excessively, degrading its ability

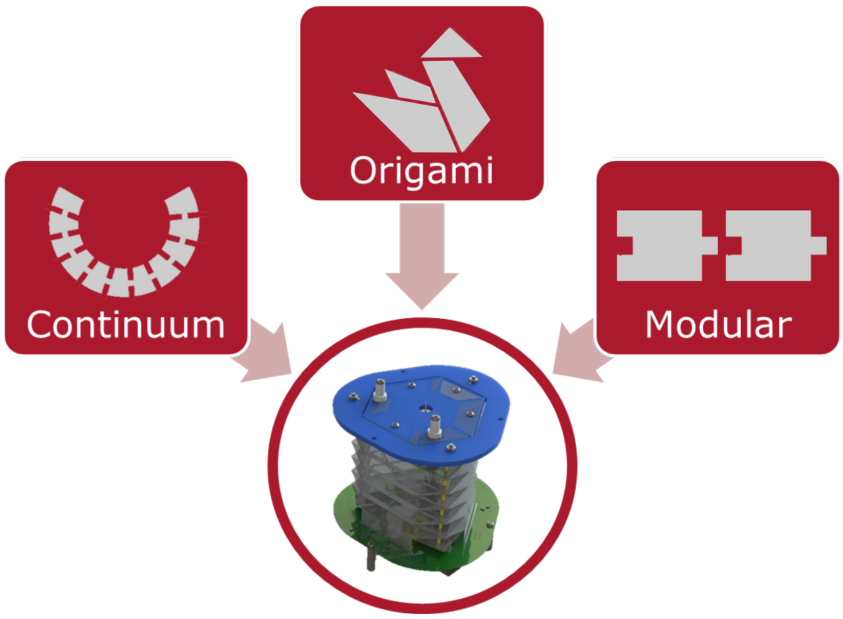

Figure 2.1: Proposed work combining three main components: continuum, origami, and modularity.

to manipulate objects. This key feature will allow for additional grasping techniques that are not normally available or favorable. For example, whole-arm grasping with a continuum arm in the horizontal plane can only be achieved with a torsionally strong design [14].

In summary, the contribution of the work in this chapter is the development and analysis of a new approach to continuum manipulation that:

- Uses an origami-inspired mechanism as its body, allowing for significant extension/contraction and bending motions.
- Has high torsional strength, allowing it to resist undesired twisting deformations in 3-D space.
- Is composed of self-contained modules, whereby the addition of modules requires minimal design changes.

The rest of the chapter will discuss the design and fabrication of the proposed origami manipulator, kinematic modeling, control approach, and finally the results to show some insights of the

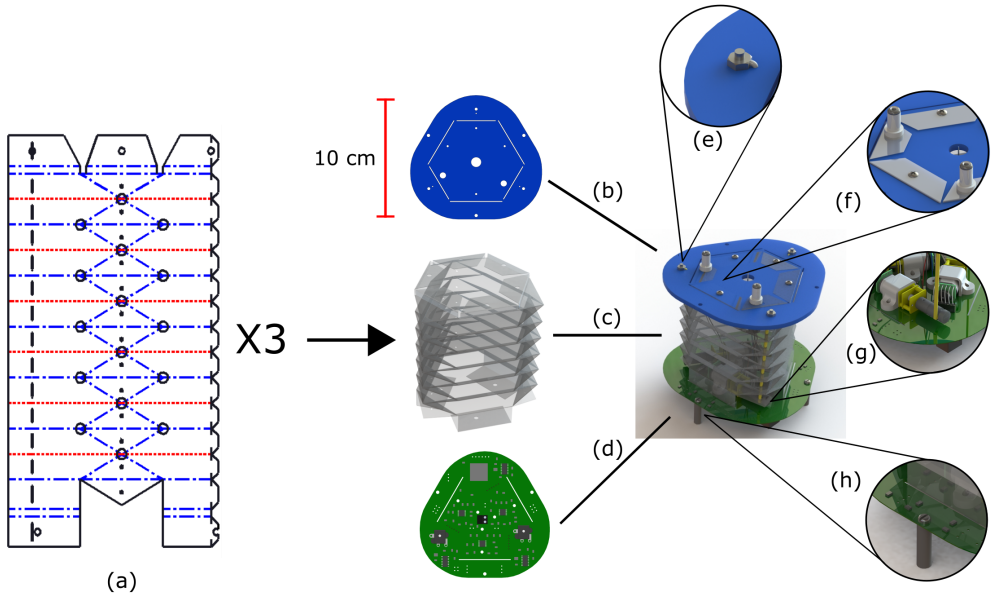

Figure 2.2: Components of the first generation origami continuum module. Yoshimura crease pattern used for the collapsible part, red dashed lines indicate the valley folds, blue dash-dot lines indicate the mountain folds and black lines indicate the cuts, three independent folded sections allows for: (a) a more uniform module, (b) acrylic top plate, (c) folded collapsible part, (d) printed circuit board (PCB) acting as bottom plate at which the motors and the collapsible part are attached to. (e) Closer view of the interface between the top plate and nylon strings. Strings are secured with screws and nuts. (f) Two barrel jack connectors for logic and motors power to the next origami module. (g) Closer view of the interface between the motors and nylon strings, the yellow line indicates the nylon string. (h) 3-D printed standoff to connect to the previous origami module.

proposed work.

2.2 Design and Fabrication

The proposed continuum module consists of three main parts: a foldable origami body, brushed DC micro-motors (12 V, Pololu 150:1 gear ratio and Pololu magnetic encoder with 12 counts per revolution [60]) with pulley systems, and a controller board that offers on-board sensory measurements, feedback control, and module-to-module communication (Figure 2.2). The complete list of the motor parameters are given in Table 2.1 and three possible motor arrangements are shown in

Figure 2.3. Three motors are used for each module to generate bending in 2 axes and compression along the module length. We chose the motor arrangement shown in Figure 2.3(b) as it gives the best balance between the radial dimension and an open area in the middle that is utilized to route the power and communication wires. While the motor arrangement shown in Figure 2.3(c) looks similar to the former, it requires a larger radial dimension to account for possible mechanical interference of the motor encoders. Furthermore, the close arrangement of the magnetic motor encoders shown in Figure 2.3(c) could lead to a magnetic interference between them. Although an origami module with a smaller radial dimension can be achieved with the motor arrangement shown in Figure 2.3(a), this configuration will also increase the minimum length (fully compressed) of the module. Moreover, a more complex force transmission system may be necessary for the arrangement in Figure 2.3(a) while the two other motor arrangements allow for easy force transmission system (a single spool cable system for each motor). Alternatively, a parallel arrangement of single motor actuators with each independent origami bodies is also possible. This is similar to the design of the OctArm continuum robot which utilizes parallel arrangement of the McKibben muscle actuators. However, to keep the design simple we settled on using a single origami body with 3 motors for each module.

Table 2.1: Pololu DC brushed micro-motor parameters (extracted from the Pololu micro metal gear-motors datasheet).

Motor parameters	**Value**	**Unit**
Maximum power	1.0	Watts
Torque at maximum power	88.26	N.mm
Efficiency at maximum power	22	%
Current at maximum power	0.39	Amperes
No load current	0.06	Amperes
Stall current	0.72	Amperes

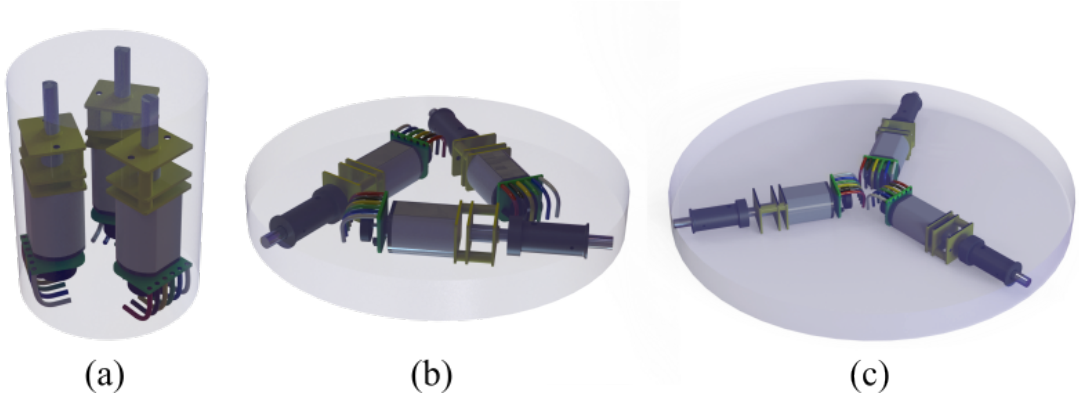

Figure 2.3: Possible motor arrangements with cylindrical volumes indicating the minimum inextensible part of the origami continuum module: (a) smallest, (b) medium, (c)largest dimension.

The foldable body is constructed based on the Yoshimura crease pattern inspired by the work in[61]. This unique structure is capable of bending in two directions and extending/retracting, while maintaining its structure and resisting torsion. Polyethylene terephthalate (PET) films were chosen as the substrate material due to their high strength to weight ratio and low cost. The crease pattern used for this structure was designed in Solidworks and machined using an Epilog Zing laser-cutter. The pattern is shown in Figure 2.2(a), where different colors indicate a variety of folds and cut. Fold lines were laser machined using a perforation pattern to reduce the stiffness so the film could be folded more easily and precisely, while preventing tears[61,62]. The collapsible body was manually folded into 3-D following the crease pattern and later joined into an approximate triangular tube. The use of three different folded sections to create one origami module enables the module to uniformly bend in all directions. The trapezoidal sections at the right side of the crease pattern are used to lock the folded sheet, when inserted in thin slots (tab-slot lock features[41]), hence creating the hollow triangular shape shown in Figure 2.2(c). More details about the origami body fabrication is shown in Figure 2.4. The radial dimension of the origami body is limited by the available motor size and the chosen motor arrangement. We chose the smallest possible radial dimension as it allows for higher possible curvature and bending angle to be attained by the origami continuum module[63].

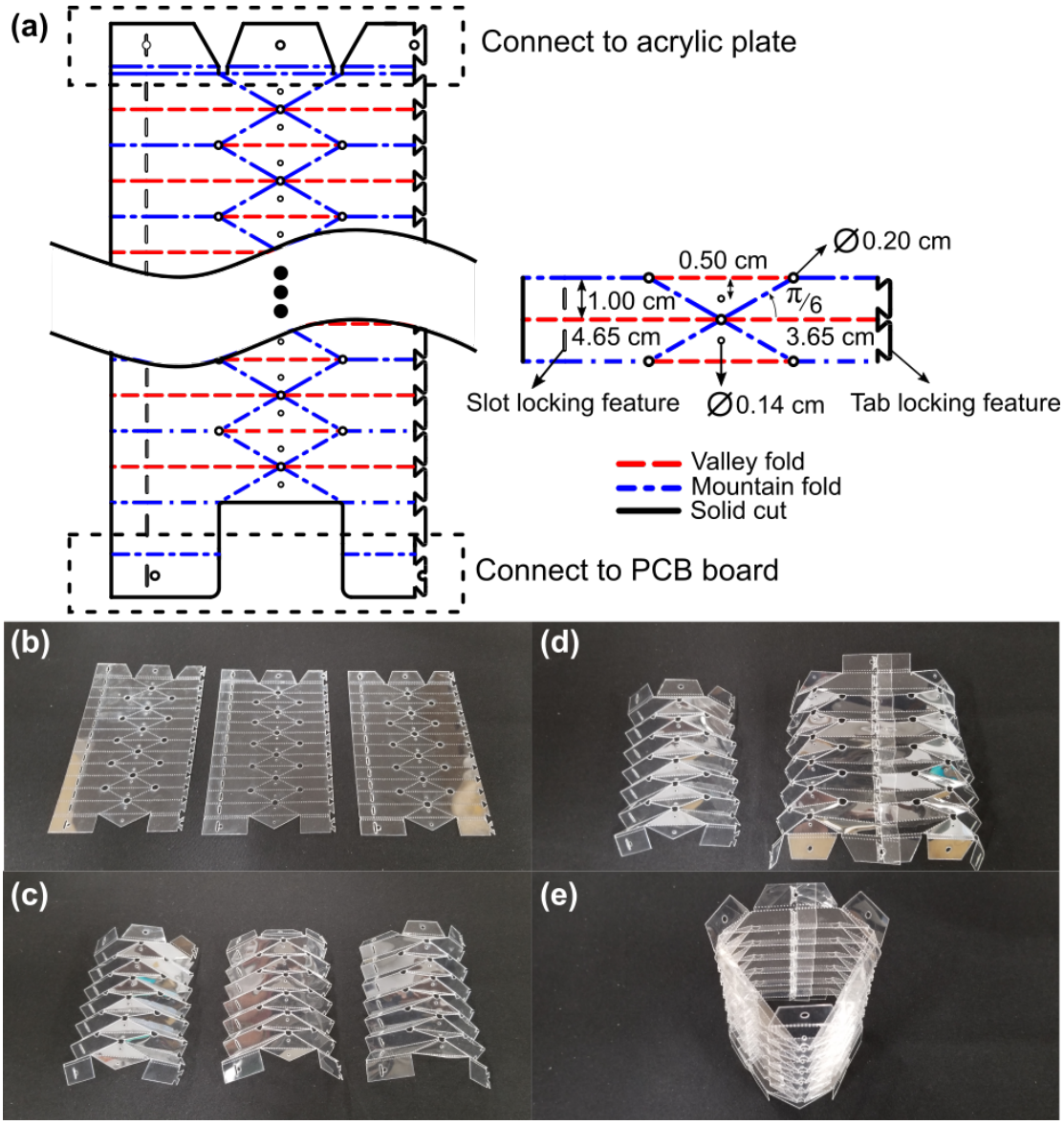

Figure 2.4: Details on the origami body fabrication. (a) Yoshimura crease pattern of the origami module with annotated dimension. (b) Perforated pattern on PET sheet engraved with laser cutter. The speed and power settings for the laser cutter are 100% and 6% respectively. The perforated pattern allows for ease of folding. (c) Folded origami sections required to construct the origami compliant body. (d) Two folded sections combined using the slot-tab locking feature. (e) Finished compliant origami body constructed from three folded sections.

The tubular structure constructed from the crease pattern presented in this paper has a length of about 8 cm without external load. Appropriately sized-holes are cut to secure the foldable structure to the blue acrylic plate on the top and to the PCB on the bottom where the motors are secured, as shown in Figure 2.2(b) and 2.2(d). Additional holes are included for the three thin nylon cables used to drive the segment which span the length of the structure along the edges. These cables are attached to pulleys mounted on miniature motors at one end and secured with screws and nuts on the acrylic plate at the other end. Each motor is equipped with a magnetic encoder for low-level position control.

Each module is controlled by a custom printed circuit board (PCB) that uses the 8-bit Atmel ATmega1280 microcontroller unit (MCU). The control board is also equipped with three DRV8801 motor drivers from Texas Instruments, capable of a peak current output of 2.8 A and three US Digital LS7366R encoder counter chips. The main task of the control board is to receive motor commands as control inputs, record the motor positions using encoders, and perform local feedback motion control. The control boards communicate using inter-intergrated circuit (I2C) protocol with different modules. An Arduino Mega 2560 board is used as an interface between the control boards and an external computer (through I2C) that handles inverse kinematics calculations for the origami module as well as data collection by an OptiTrack motion capture system.

The interface between origami modules includes two power barrel connector plugs mounted at the top (acrylic plate) of the preceding module which will connect to the female jacks soldered onto the bottom side of the PCB of the next module. In addition, the modules are secured using standoffs and screws connecting the acrylic plate of the lower module to the PCB of the upper one.

2.3 Kinematic Model

2.3.1 Forward Kinematics

Different formulations of continuum manipulator forward kinematics exist including arc geometry, D-H parameters, Frenet-Serret frames, integral representation, and exponential coordinates as summarized in [55]. The arc geometry representation with constant curvature assumption is chosen for this work due to its simplicity. A continuum module can be assumed to be a circular arc with constant curvature in 3-D space. The posterior point is located at the origin while the distal point is located in 3-D space. As shown in Figure 2.5(a), the homogeneous transformation from the origin frame at O to the frame attached to the tip of the segment at T can be derived as a rotation about Z axis by the angle φ and in-plane transformation (rotation about rotated Y axis (Y') and translation $p = [\rho(1 - \cos(\theta)), 0, \rho\sin(\theta)]^T$). If we define the curvature of the continuum module to be κ and the length of the segment to be s, then $\rho = 1/\kappa$ and $s = \theta/\kappa$. The tip position of the continuum section is then given by

$$[\rho\cos(\varphi)(1 - \cos(\theta)), \rho\sin(\varphi)(1 - \cos(\theta)), \rho\sin(\theta)]^T$$

while the orientation is given by the product of the rotation matrix about the Z and Y' axes of φ and θ magnitudes.

In other words, each continuum segment can be fully described by three configuration parameters κ, φ, and s as shown in Figure 2.5(a). Using the derived forward kinematics we are able to find the distal point of each continuum segment given a set of configuration parameters. This information is especially necessary when multiple origami modules are combined in series (i.e. the distal point of the previous origami module will be the posterior point of the next module). In practice, a separation due to the end connectors between modules need to be considered in multi-segment forward kinematics. Furthermore, the configuration parameters can be represented as a function of

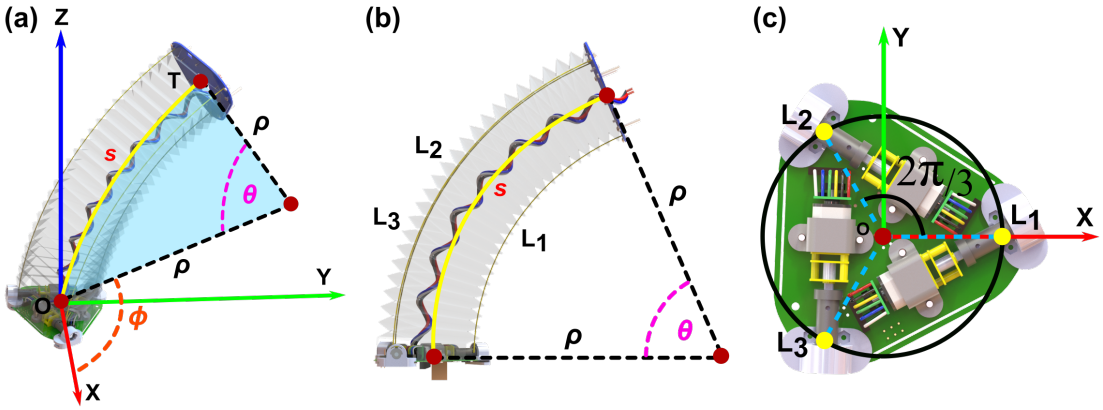

Figure 2.5: (a) Isometric view of the origami continuum robot with its joint configuration annotated: arc length s, bending angle θ, radius of curvature ρ, and bending direction φ. (b) The robot's base frame is defined with the shown triad. Side view of the origami continuum robot. The tendon lengths associated with a particular robot's shape are denoted by L1, L2, L3. (c) Top view of the custom-made controller board. Tendon attachment points are indicated by the yellow dots.

tendon lengths as derived in [64].

$$\rho = \frac{(3L_0 + l_1 + l_2 + l_3)r}{2\sqrt{l_1^2 + l_2^2 + l_3^2 - l_1 l_2 - l_1 l_3 - l_2 l_3}}, \tag{2.1}$$

$$\theta = \frac{2\sqrt{l_1^2 + l_2^2 + l_3^2 - l_1 l_2 - l_1 l_3 - l_2 l_3}}{3r}, \tag{2.2}$$

$$\varphi = arctan\left(\frac{\sqrt{3}(l_3 - l_2)}{l_2 + l_3 - 2l_1}\right), \tag{2.3}$$

where l_1, l_2, l_3 are the tendon length variation, L_0 is the minimum module/tendon length, and r is the module radius. As investigated in [63] the maximum curvature can be found when the tendon configurations are given by $(l_{max}, l_{min}, l_{min})$ and $(l_{min}, l_{max}, l_{max})$. Thus by substituting these values to Equation (2.2) we can obtain the maximum bending angle of the module.

2.3.2 Inverse Kinematics

In order to control the origami module, it is necessary to develop a relationship between the configuration parameters and cable lengths. The detailed derivation for inverse kinematics of a continuum section is presented in[65]. The relationship between the cable lengths and the configuration parameters can be written as:

$$\begin{aligned} l_1 &= 2n \sin\left(\tfrac{\kappa s}{2n}\right)\left(\tfrac{1}{\kappa} - r\sin(\varphi)\right) \\ l_2 &= 2n \sin\left(\tfrac{\kappa s}{2n}\right)\left(\tfrac{1}{\kappa} + r\sin\left(\tfrac{\pi}{3} + \varphi\right)\right) \\ l_3 &= 2n \sin\left(\tfrac{\kappa s}{2n}\right)\left(\tfrac{1}{\kappa} - r\cos\left(\tfrac{\pi}{6} + \varphi\right)\right) \end{aligned} \tag{2.4}$$

where l_1, l_2, and l_3 are the lengths of cables 1, 2, and 3 respectively, s, κ, φ are the configuration parameters as defined previously, r is the distance from the center of the mounting plate to the cable attachment point, and n is the number of sections within the larger continuum manipulator. Note that, since each origami module is operated independently, $n = 1$ for our system.

2.4 Results and Discussion

2.4.1 Torsional and Axial Stiffness

In order to assess the structural properties of the proposed origami module, we conducted two experiments. The first experiment was to identify the torsional stiffness of the module, and involved loading the origami actuator with a known couple moment and measuring how much it deformed. We achieved this by fixing the actuator on one end and using suspended weights to apply equal and opposite forces on each side of the centroid, offset so as to create a pure torsional bending moment. We performed this experiment on three modules each of 0.127 mm (5 mil) and 0.178 mm (7 mil) thick PET with external torques up to 0.429 Nm, using an IR marker-enabled motion tracking system (OptiTrack) to record the twist angles.

The results are summarized in Figure 2.6(a). The results show that the thicker module offers

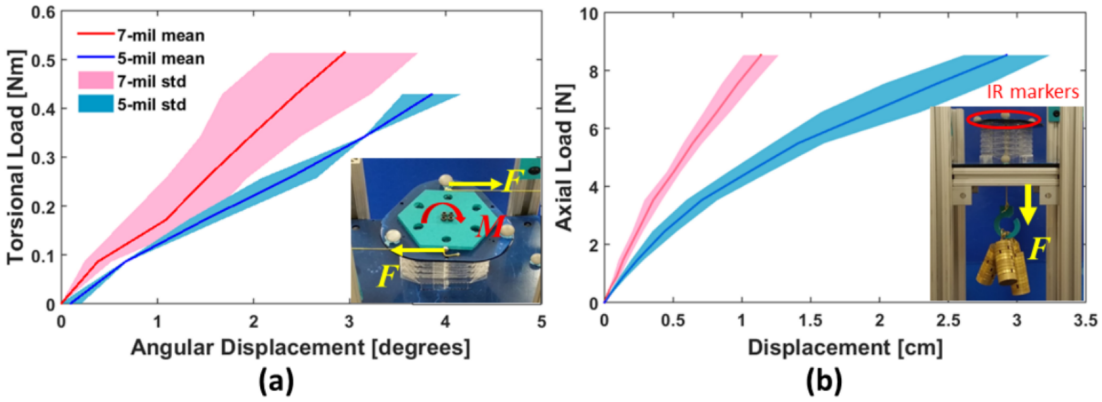

Figure 2.6: (a) The mean and standard deviation of torsional loading capability of the 7 and 5 mil origami modules. The data for 5 mil module was only obtained up to 0.429 Nm as the module started to twist excessively and reaching the point of failure. (b) The mean and standard deviation of torsional loading capability of the 7 and 5 mil origami modules. The modules were tested until buckling started to occur.

higher torsional stiffness while a thinner sheet yields a lighter structure without much decrease in torsional strength. However, the thinner material started to twist excessively at the maximum moment of 0.429 Nm, hence the experiments were not continued beyond this torque. This failure mostly happened in the regions where the origami structure was not attached to the acrylic plates. The actuators constructed with thicker PET films did not show signs of failure up to 0.515 Nm, a relatively large torque compared with the weight of the origami film. The average torsional stiffness for 7 mil and 5 mil modules are 0.128 Nm/deg and 0.110 Nm/deg, respectively.

Axial loading experiments were conducted by keeping the modules upright clamping the bottom end-plate and using known payloads up to 0.87 kg for both 7 mil and 5 mil film. The known payload was attached to the top acrylic plate of the actuator hence compressing the origami structure. In this experiment, the load was increased until the actuator started to buckle. In contrast to the torsional stiffness profile, Figure 2.6(b) reveals that the axial stiffness varies more significantly with changing film thickness. This was expected because origami folds act like springs, whereby thinner substrates offer lower stiffness. Moreover, the 5 mil modules exhibit more nonlinear behavior

Table 2.2: Origami module parameters.

Properties	Value	Unit
Mass	110	gram
Origami structure radius	3.5	cm
Uncompressed length	6.5	cm
Fully compressed length	3.0	cm
Maximum bending angle	38.2	degree
Axial stiffness	7.482	N/cm
Torsional stiffness	7.311	Nm/rad

compared to the 7 mil ones.

By calculating the slope of the graph we can determine an average spring constant of the origami body in the axial direction. This translates to the payload capability of the modules without additional springs. The average spring constants were found to be 7.482 N/cm and 2.877 N/cm for film thicknesses of 7 mil and 5 mil, respectively. From these initial findings, 7 mil modules offer better performance to be used in a continuum manipulator, where its higher torsional and axial stiffness allows the module to better withstand external forces. A full list of module parameters can be found in Table 2.2.

2.4.2 Bending Stiffness

We investigated the bending stiffness of our module by applying loads in a horizontal cantilever configuration. The orientation of the acrylic plate at the free end with respect to the vertical plane is defined as the bending angle and measured using the OptiTrack tracking system. First, we investigated the module behavior without compensation, where we fixed each cable at a constant length and applied payloads. It should be noted that due to the lack of backdrivability in the motors, this is similar to an entirely passive response. We tested this for three separate actuation lengths, results of this experiment can be seen in Figure 2.7(a). Assuming the amount of bending increases linearly as

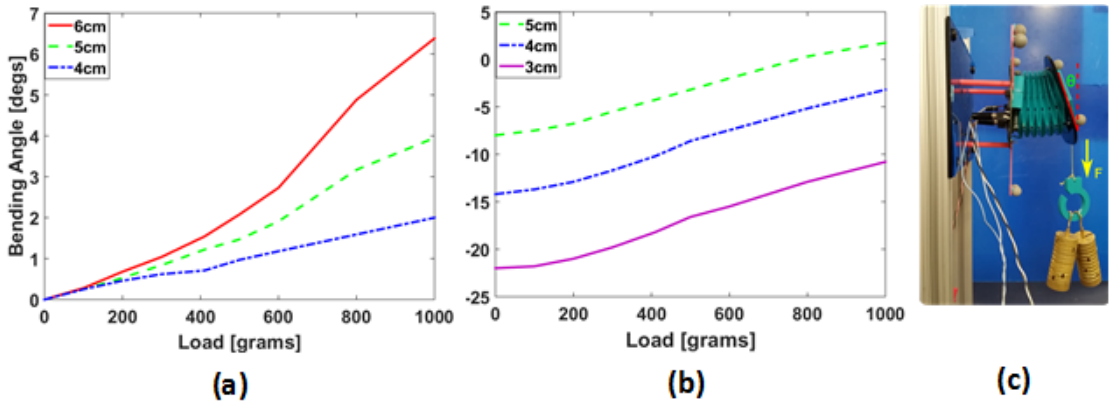

Figure 2.7: Result for an origami module with 3 actuated motors: (a) forming a straight continuum section, (b) with only 1 (top) motor actuated forming a curved section, (c) experimental setup where the origami module is loaded in a cantilever configuration.

a function of load, we can use a linear fit of the curves to find the bending stiffness. The estimated bending stiffness values are then 0.0020, 0.0040, and 0.0065 deg/gram for 4, 5, and 6 cm modules, respectively. We found that when fully extended, the module will bend by 6.38 degrees under a load of 1 kg. This configuration represents a worst-case scenario, with a fully extended, passive actuator. This load is equivalent to about 3 additional modules mounted serially.

We also investigated the ability of the manipulator to compensate for these loads by actuating in opposition to the force as shown in Figure 2.7(c). We actuated a single cable to a specific length, which bent the actuator in the opposite (negative) direction, and repeated the same bending experiment, the results of which are shown in Figure 2.7(b). This allows the actuator to stay level under greater forces, but with the trade-off of losing some control on the module shape or range of controllable motion. The estimated bending stiffness values found using a linear fit of the curves are 0.0121, 0.0117, and 0.0104 deg/gram for bent modules with 3, 4, and 5 cm shortest actuated tendon length, respectively.

2.4.3 Scalability and Deployability Quantitative Measures

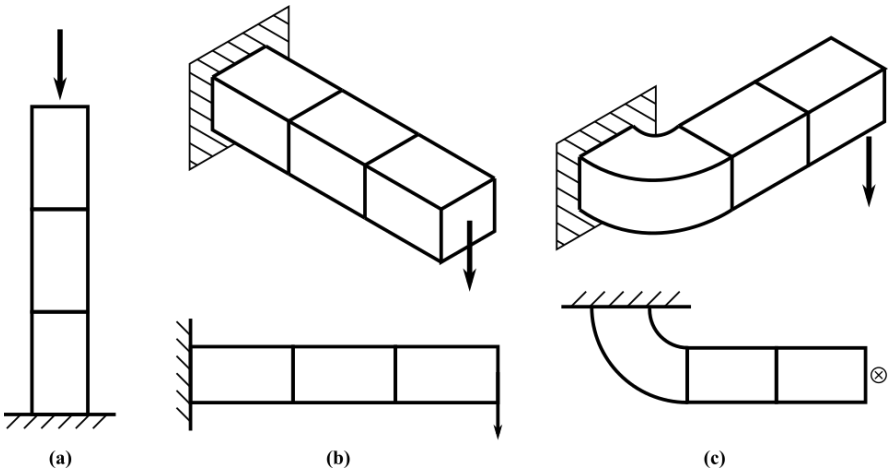

Figure 2.8: Different loading condition on a multi-segment robot: (a) axial, (b) transverse, and (c) torsional. Based on the stiffness properties and weight of the module we calculate the maximum number of adjacent modules can be supported by the base module for a given maximum displacement.

One quantitative measure of scalability is to analyze how many modules can realistically be connected before the whole robot cannot support its own weight. Based on the stiffness properties (axial, bending, and torsional) and mass of each module we can calculate the maximum number of adjacent modules that can be supported by the base module. For the axial loading case (Figure 2.8(a)), the base module is theoretically capable of supporting 7 modules with calculated axial displacement of 1 cm. For the transverse and torsional loading cases, we assume that the center of mass for each module is located halfway of the module's length ($L_{max}/2$). In reality, the module's center of mass should be closer to the base of a corresponding module ($< L_{max}/2$) since the majority of the mass is contributed by the motors and the PCB located at the base. The equation describing torque applied at the base for the transverse loading (Figure 2.8(b)) is,

$$\tau_{transverse}(n) = m_{mod}\, g\, ((nL_{max}/2 + n!L_{max})) \tag{2.5}$$

where n is the number of adjacent modules and n! is n-factorial, L_{max} is the module's length when fully extended, m_{mod} is the mass of the module, and g is the gravitational acceleration constant. Given that, $L_{max} = 0.065\ m$, $m_{mod} = 0.11\ kg$, and $g = 9.81\ m/s^2$, then the base module can support up to an additional 3 modules with angular displacement of 6.38 degrees. That is for the case of a passive and un-actuated base module. We can increase the number of modules that can be supported by bending the module upward. This would compensate for the bending caused by the external load (additional modules connected in series). In this case, suppose that the base module is bent upward with 3 cm shortest tendon length and the moment arm of 4.75 cm (halfway between 3 and 6.5cm). From Figure 2.7(b), we can find the amount of load that can be supported by the bent base module for 6.38 degrees displacement by extrapolating the curve for 3 cm length. The extrapolated load is found to be 2.4178 kg which translates to 1.1266 Nm torque at the base. This value of torque is larger than the torque exerted by 3 adjacent modules but smaller than the torque applied by 4 adjacent modules as given by Equation 2.5. Thus we can find the amount of extra load ($m_{payload}$) that can be carried in addition to connecting 3 adjacent modules as shown below,

$$\begin{aligned} m_{payload} &= \tau_{resultant}/(l_{payload} * g) \\ &= (1.1266 - 0.5261)/((0.0475 + 3 * 0.065) * 9.81) \\ &= 0.252\ kg \end{aligned}$$

where $\tau_{resultant}$ is the amount of torque can be sustained by the actuated base module connected to 3 adjacent modules. This value is obtained by subtracting the extrapolated torque value from Figure 2.7(b) by the torque calculated using Equation2.5 for $n = 3$. Furthermore, $l_{payload}$ is the moment arm of the payload suspended at the tip of the last (4^{th}) module. Note that, the number of modules that can be supported would increase even further if all the adjacent modules are actuated as well.

Similarly, the equation for describing torque applied at the base for the torsional loading (Figure 2.8(c)) is defined as,

$$\tau_{torsion}(n) = m_{mod}\, g\, ((nL_{bend} + nL_{max}/2 + (n-1)!L_{max})) \tag{2.6}$$

where L_{bend} is the moment arm of the bending base module (assumed to have 90 degrees bending angle). Given that $L_{bend} = 0.0413\ m$ then the base module can support 5 additional modules with angular displacement of 16.3 degrees (assuming that no bending displacement occurs on all the modules). In contrast with the transverse loading case, we cannot actively increase the torsional stiffness as this feature is passively contributed by the origami structure.

Another measure of scalability is to measure how much load a single module can handle based on the motor specifications. This dictates how many passive modules can be supported by a single module. Given that each motor is capable of providing 9 kg.mm torque at maximum power and the diameter of the 3-D printed spool is 7 mm, we found that a single module (with 3 motors) can lift up to 7.71 kg payload which translate to roughly 70 modules. The I2C communication protocol with 7-bit addresses used in this research work, limits module connection up to 128 devices. However, in practice the maximum number of modules can be connected in series is mainly dictated by the power requirement. The current module's interconnect/interface is capable of withstanding 20 A current, which translates to powering 9 modules in series (taking into the consideration of 0.72A stall current for each motor). A larger interconnect and thicker power wires would be necessary to overcome this limitation. The maximum number of modules can be connected in series given various limiting cases/factors is summarized in Table 2.3.

Furthermore, we found that using the current crease pattern design and folding technique we can make an origami body as small as a thumb while the current robot's radial dimension is about the size of an adult human arm. Theoretically, there is no maximum limit on the module size except

Table 2.3: Maximum number of adjacent modules can be connected in series given various limiting cases. Additional modules can be connected for the case of transverse loading if all the adjacent modules are actuated instead of just the base module.

Limiting cases	**Maximum no of adjacent modules**	**Expected displacement**
Axial loading	7	1 cm
Transverse loading w/ un-actuated base module	3	6.38 degrees
Transverse loading w/ actuated base module	3 (+252 gram load)	6.38 degrees
Torsional loading	5	16.3 degrees
Maximum motor torque	70	-
I2C communication	128	-
Module's interconnect current rating	9	-

due to the dimension of the laser cutting area. The scalable design allows for various size actuators tailored to their intended applications. Additionally, one can explore various actuator arrangements to achieve improved performance e.g. stacking multiple modules in parallel to create a stiffer robot base.

A typical measure for robot deployability is to consider its maximum duration of operation enabled by a portable power source. Suppose that we have deployed a 3-segment origami continuum robot powered with 11.1 V, 2200 mAh LiPo battery. Depending on the deployment scenario we can estimate the total current consumption by defining certain time percentages at which the robot is in particular modes. An example is given below,

$$\begin{aligned} \textit{Total current}\,(1\,\textit{motor}) &= 70\%\ \textit{maximum power} + 20\%\ \textit{idle} + 10\%\ \textit{unintended stalling} \\ &= 0.7 \times 0.39\,A + 0.2 \times 0.0\,A + 0.1 \times 0.72\,A \\ &= 0.345\,A. \end{aligned}$$

In that case, we can expect the robot to last for 42.5 minutes. An addition of a solar-charging subsystem would allow for the robot to regain its energy when deployed for a long-duration mission.

We can also consider the compression ratio the origami module as another measure of deploya-

bility. This dictates the minimum length of compressed modules that needs to be accommodated during the deployment. A high module compression ratio is important in outer space applications for example since it would allow for compact storing of devices/mechanisms which to be deployed for later use. The modular structure of the origami arm presented in this work also can be considered to be a deployability measure as highly critical missions would benefit from a system that can be swapped out rapidly when failed.

2.4.4 System Response

To evaluate the performance of the proposed origami module, we conducted step response experiments with both open and closed-loop control shown in Figure 2.9. The experiments commanded the actuator to reach a certain configuration parameter set: arc length (s), θ, and φ, as described in the kinematic modeling section, using a low-level proportional-integral-derivative (PID) controller on the motor encoder position.

To evaluate the performance of the origami continuum manipulator module in terms of its capability to reach a desired set of configuration parameters, we performed experiments in a custom motion capture environment, comprising four OptiTrack IR cameras. These cameras track passive IR markers attached to the top and bottom end connectors of the module to experimentally measure the configuration of the origami continuum module. The measurements were transferred to a desktop computer through an Ethernet connection for processing.

The configuration parameters were found from the centroid and orientation of the bottom and top plates of the module. Assuming that the origami module only experiences bending in a plane, angle θ is equal to the dot product between the frames attached to the bottom and top plates. Once θ is determined, we calculate the value of ρ using the cosine rule, and curvature κ is defined as $1/\rho$. Lastly, the bending plane angle φ is determined using trigonometry.

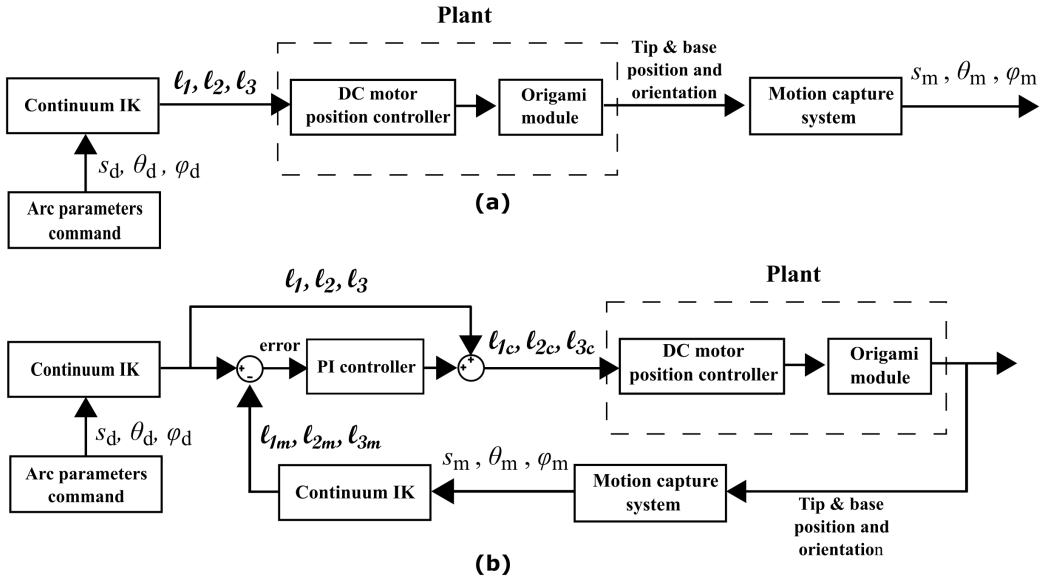

Figure 2.9: Control architecture for: (a) open-loop, (b) closed-loop.

$$
\begin{aligned}
\theta &= \tan^{-1}\left(\frac{\|\vec{t_n}\times\vec{b_n}\|}{\vec{t_n}\cdot\vec{b_n}}\right) \\
l &= \|\vec{p_b} - \vec{p_t}\| \\
\rho &= \sqrt{\frac{l^2}{2(1-cos(\theta))}} \\
\kappa &= \frac{1}{\rho} \\
\varphi &= \tan^{-1}\left(\frac{p_{ty}-p_{by}}{p_{tx}-p_{bx}}\right),
\end{aligned}
$$

where $\vec{t_n}$ is the tip plate normal (Z) direction vector, $\vec{b_n}$ is the base plate normal (Z) direction vector, $\vec{p_b} = [p_{bx}, p_{by}, p_{bz}]$ is the base plate position vector, $\vec{p_t} = [p_{tx}, p_{ty}, p_{tz}]$ is the tip plate position vector. Since the motion capture system is capable of tracking the position of the markers with sub-millimeter resolution, even a slight difference in tip and base positions will result in a non-zero φ reading. Thus, we implemented a simple filter that utilizes a small dead-zone ε_{dz} around zero.

The open-loop control of the origami actuator is based on the inverse kinematics of a continuum

section which we used to find the required cable lengths (l_1, l_2, l_3), that will shape the module into the desired configuration (s_d, θ_d, φ_d), as shown in Figure 2.9. The cable lengths are converted into encoder positions, which are then sent to the low-level controller as reference signals. The closed-loop control takes into account the difference between the desired cable lengths generated from the inverse kinematics (l_1, l_2, l_3) and the cable lengths obtained through a conversion of the measured configuration parameters (l_{1m}, l_{2m}, l_{3m}). A proportional-integral (PI) controller that regulates the errors between the desired and measured cable lengths is added to the open-loop feed-forward commands, producing final motor commands (l_{1c}, l_{2c}, l_{3c}).

Figure 2.10 shows the results of step response for both open and closed-loop control, at which the configuration parameters were tracked. The results show that the closed-loop control is able to bring the system to reach the desired configuration. No overshoot is observed and the rise times are 0.5 s for both control schemes. These results also imply that the inverse kinematics model was successful in bringing the actuator close to the desired configuration.

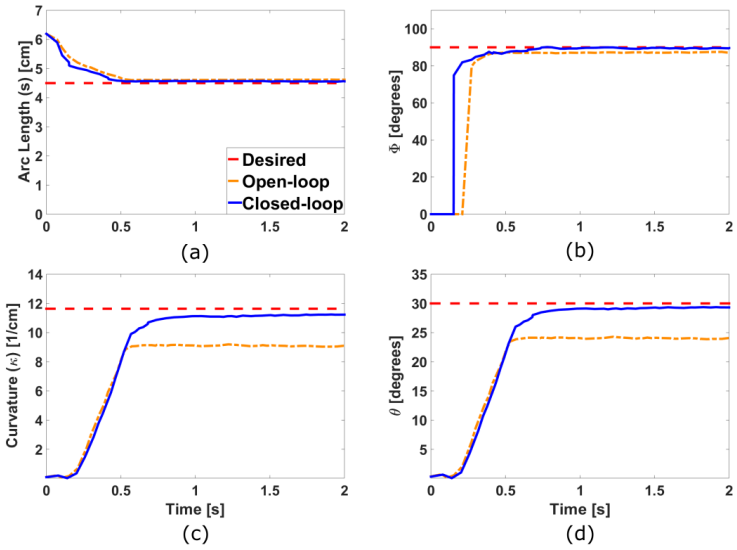

Figure 2.10: Step response of a single module given a configuration: (a) s = 4.5 cm, (b) φ = 90 degrees, (c) κ = 11.64, and (d) θ = 30 degrees. Results shown for both open and closed-loop control.

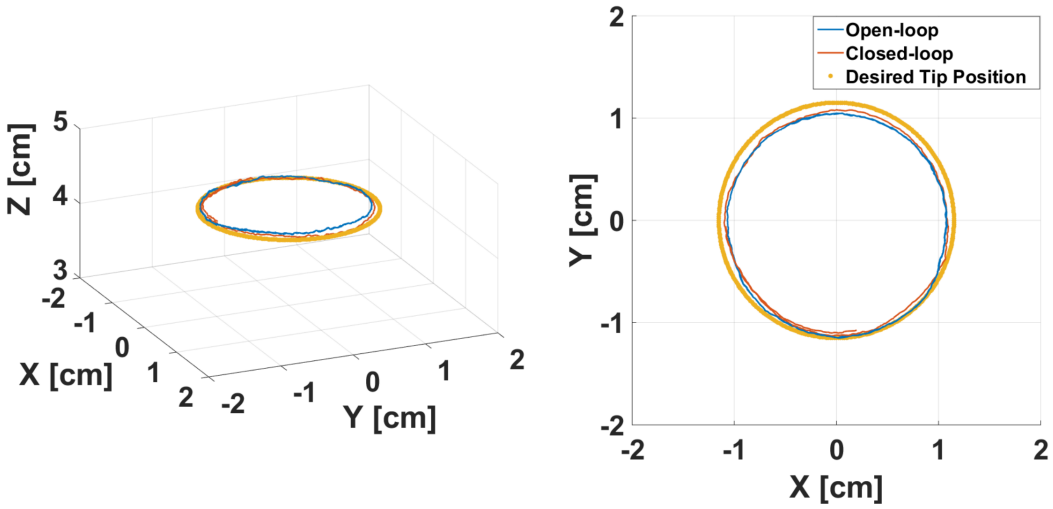

Figure 2.11: Circular tracking with the proposed origami continuum module using open and closed-loop control.

Table 2.4: Single module circle tracking results.

	Open Loop	Closed Loop
Max Horizontal Error	1.237 mm	1.097 mm
RMS Horizontal Error	0.734 mm	0.681 mm
Max Vertical Error	0.970 mm	0.820 mm
RMS Vertical Error	0.579 mm	0.373 mm

2.4.5 Circle Tracking

The dynamic response of the proposed module was evaluated by performing a circle tracking experiment. A circular trajectory was generated varying the φ values over the range of $[0, 2\pi]$ while keeping the desired arc length and curvature constant. For this experiment we kept the same values of arc length and curvature as the ones used in the step response experiment in Figure 2.10. The tip position of the actuator was tracked using motion capture as explained earlier and compared to the desired trajectory. Figure 2.11 displays the results of this experiment with the desired and tracked tip trajectories in 3-D (left) and in 2-D (right), with quantitative results summarized in Table 2.4.

These results indicate that our system is well-calibrated and open-loop control may provide suc-

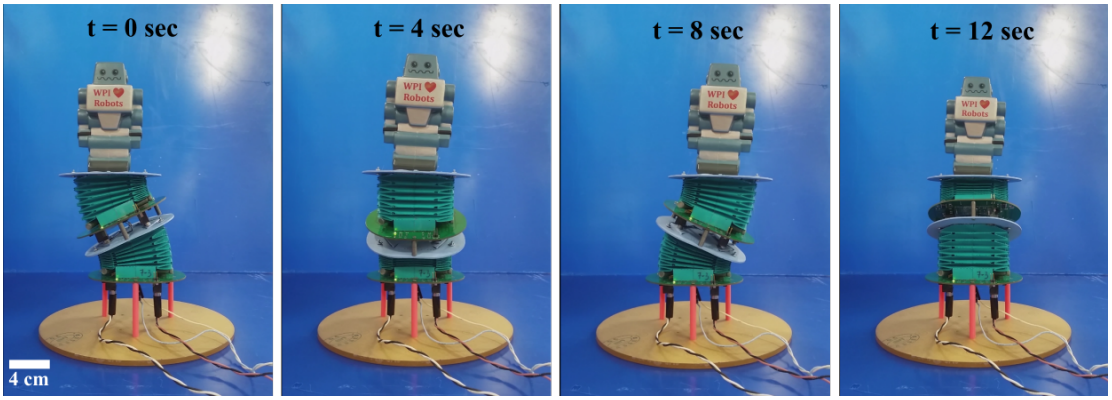

Figure 2.12: Two combined actuators executing circle follow trajectory while keeping the top plate parallel to the ground, a small doll was placed on top of the plate and was able to stay balanced.

cessful tracking of desired paths under no disturbances, but feedback will likely be required to compensate for modeling errors and disturbances during system operation. Moreover, the larger error difference observed on the step response (especially on κ and θ) compared to the error for the circle follow experiment also suggest that the system can still reliably reach the desired task-space goal despite a relatively large error on the configuration space.

2.4.6 Multi-module Motion Evaluation

As a proof-of-concept case study, two origami modules were connected in series, as shown in Figure 2.12. This figure displays snapshots of the combined two-module system following a circular tip trajectory while keeping the top plate parallel to ground, allowing for an object to be placed on top and kept from falling. This maneuver was achieved by keeping the arc length and θ for both modules to be the same and sweeping the φ values over the range of $[0, 2\pi]$ with an offset of π. Independent control of each origami module was demonstrated without any modification of the system architecture.

2.5 Conclusion and Future Work

This chapter focuses on a novel approach for an origami-inspired modular continuum manipulator with torsional strength. Origami modules were designed and analyzed for their axial, torsional, and bending deformations. The continuum module is both extensible up to 116 % its original length and capable of resisting torsion about 20 times higher than the current state of the art continuum robot while still being light-weight. Furthermore, the modular approach of the origami continuum robot allows for easy extension of the system and rapid replacement of failed modules. An analysis was presented to justify our claims on the module scalibility and deployability. Both open and closed-loop step responses of the proposed continuum modules were investigated. When exposed to a step input, the origami module is able to go to the desired configuration and reach a steady state within 1 s. A circle following routine was tested on a single module, and the results show that the actuator is capable of following the commanded trajectory within reasonable error bounds. No significant improvement was observed when a closed-loop control scheme was introduced to the system because the feed-forward term generated from the inverse kinematics of a continuum section was able to bring the actuator close to the desired configuration parameters. However, further testing involving external disturbances and faster tracking velocities will be appropriate to test the response of the closed-loop control.

One possible future research direction is to explore different morphology of the origami structure. For example, one may investigate the performance of the module with a tapered shape origami body that more resembles octopus arms or an elephant trunk. A more complex crease pattern would be neccesary to create this structure, but it should be possible as theoretically any polygonal shape can be created from origami folds. Additionally, it would be beneficial to explore parallel arrangements of the actuator to investigate its performance benefits.

3

Origami Manipulator

The following chapter presents the next step of this dissertation work, including improvements made to the origami continuum module, development of an inverse kinematics solver followed by implementation of feedback control for the multi-segment manipulator. Additionally, grow-to-shape algorithms to plan for robot motion following tortuous path are proposed and evaluated. Lastly, we showcase various applications of the continuum robot for pick-and-place, inspection/exploration, and robotic art application.

3.1 Background and Related Work

Inverse kinematics formulation is essential to achieve low-level robot motion, by finding necessary joint configurations that will produce desired pose in task space. The inverse kinematics solution is often non-trivial even for conventional rigid robots and is further complicated by the highly non-linear nature of continuum robots. In general there is no closed-form solution; nevertheless, several quantitative and qualitative based methods to solve for multi-section continuum inverse kinematic problems have been presented recently[66,67,68,69]. However, the solution proposed by Neppalli et al. does not allow for decoupling of the desired tip position and orientation of the robot[66]. Thuruthel et al. proposed using multi-layer perceptron to develop global inverse kinematics solution on the position level[67]. This approach would require retraining for extension of the system and finding appropriate tolerance in training samples. Another popular approach is to use accurate forward kinematics models and use an optimization method to solve the inverse kinematics problem[68,69]. We follow a similar methodology to the latter, and focus on the effect of cost functions on the precision of the robot pose. In contrast to similar works, we provide a complete solution that accounts for both position and orientation. We show that maximizing the smoothness of the low-level motor commands avoids exciting vibrations of the long and slender soft robotic body and results in more precise positioning performance.

Applications such as minimally invasive surgeries, search-and-rescue, and structure inspection, demand robots to successfully traverse through tortuous a path. Due to their highly redundant and compliant natures, continuum robots promise a suitable solution for this particular requirement. Choset and Henning[70] realized the potential of serpentine robots to navigate through a tortuous path by specifying the robot body to follow the path traced by the head, hence the term follow-the-leader motion was coined. This routine translates to appropriately selecting tube pre-curvatures and deployment sequences in the context of a concentric tube robot[71], or finding robot joint con-

figurations that advances its tip to the desired position along the path while minimizing deviation from the path previously traversed[72,73], or even through mechanical design that intrinsically guides the robot to follow its tip motion[74]. Non-extensible continuum robots typically require an additional feed-in/insertion system to achieve follow-the-leader motion more effectively. In contrast, extensible continuum robots e.g. those proposed in this dissertation, are more advantageous as they can approximate the path more accurately through contraction to their minimum lengths (ideally to 0 length) and extending while maintaining the same curvatures. In this work we propose a heuristic method which we term "grow-to-shape" algorithm and compare its performance to the optimization-based methods used by Palmer et al. and Neumann et al.[72,73]. We extend the heuristic approach with selective optimization and present results both in simulation and experimentally.

In summary, we propose a smoothness maximization method to solve for inverse kinematics and to achieve task-space control of the robot. Furthermore, we evaluate the performance of our origami continuum robot following the calculated inverse kinematics trajectories with and without feedback control. We also develop grow-to-shape algorithms to highlight the superior capability of continuum robot in navigating through a tortuous path. Last, we showcase the robot's capabilities in various experimental scenarios employing the proposed methods.

The novel contributions presented in this chapter are:

- A smoothness preserving inverse kinematics solver for a multi-segment continuum robot.
- A grow-to-shape algorithm for planning the robot motion to navigate a constrained environment, thus further highlighting the benefit provided by continuum robots compared to the rigid robots.

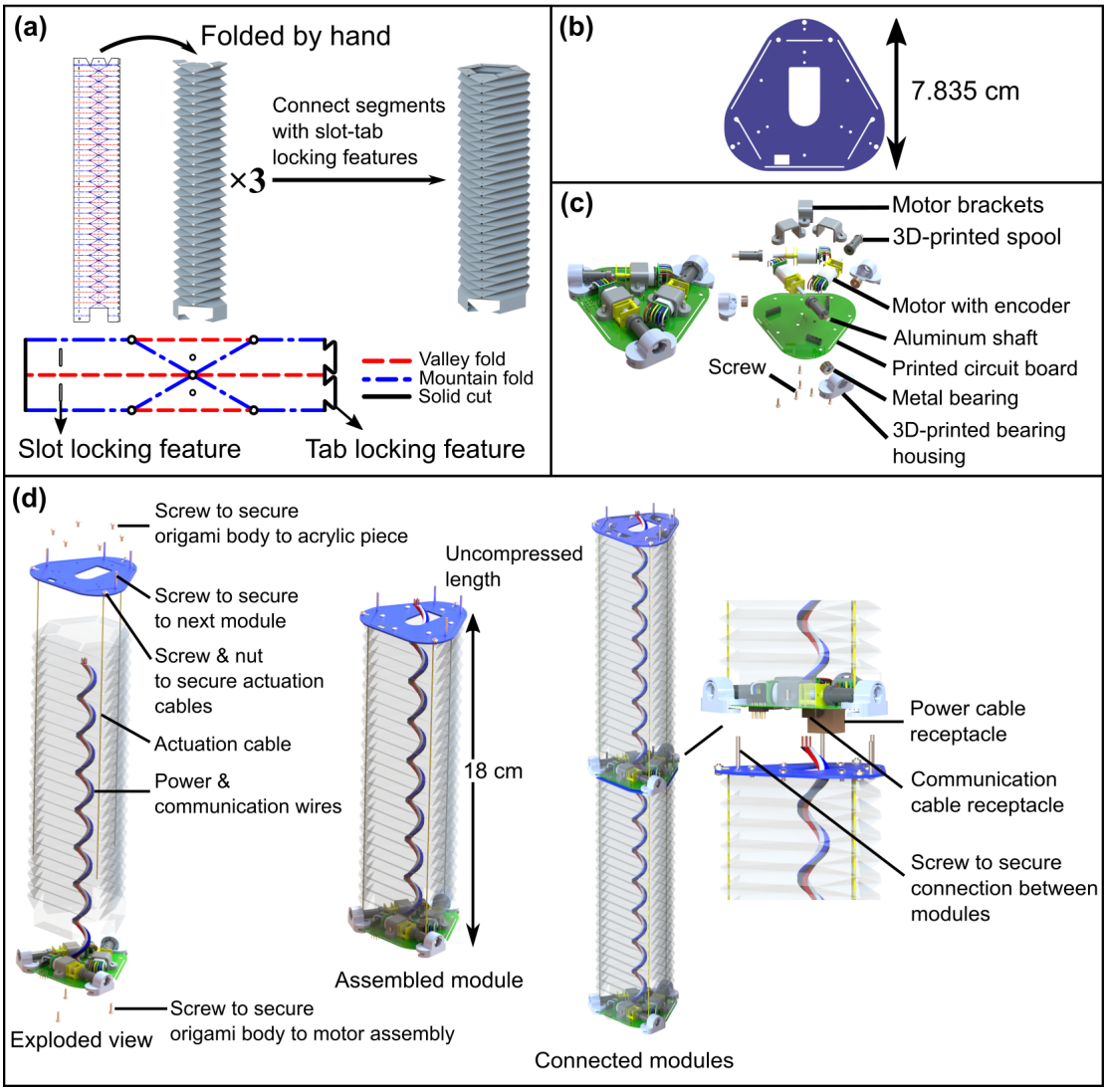

Figure 3.1: (a) Origami body assembly, (b) acrylic top plate, (c) motor assembly, (d) origami module assembly.

3.2 Second Generation Origami-Inspired Continuum Module

In the previous chapter, we introduced a tendon-driven modular continuum robot capable of significant length change (about 1.25 times its original length) and highly resistant to torsion. These two characteristics are enabled by the tubular accordion-like structure fabricated from a thin sheef of Polyethylene Terephthalate (PET) following the well known Yoshimura origami crease pattern. We increased the overall length of the origami body to enlarge the workspace of the module (Figure 3.1(a)). The current module is also equipped with a new controller board with reduced dimension due to smaller micro-controller chip (Atmel, ATmega32U4) being used. Additionally, we improved the module design to reduce its overall profile e.g, radial size and interface between the modules (Figure 3.1(b)). Additionally, metal bearings and appropriate 3-D printed bearing housings are introduced in this iteration of the module to provide additional support for the motor shaft (Figure 3.1(c)). This will reduce the adverse effect of lateral loading on the shaft caused by the actuation cable. The assembly process for connecting multiple modules does not change from the previous iteration (Figure 3.1(d)). A total of 4 electric wires are needed for each origami module for power and I2C communication. The interface between origami modules includes connecting these wires to the appropriate receptacles present on the control board of the proceeding module. In addition, the modules are mechanically secured using screws. The current module properties are summarized in Table 3.1.

Origami module stiffness characterization

In order to verify that the improved module possesses similar compliance properties to its previous version, we conducted axial and torsional stiffness measurements with the test setups shown in Figure 3.2 and Figure 3.3. To determine the axial stiffness of the origami compliant body, we fixed one end of the origami body to a motorized linear slide and the other end to a load cell (Sparkfun,

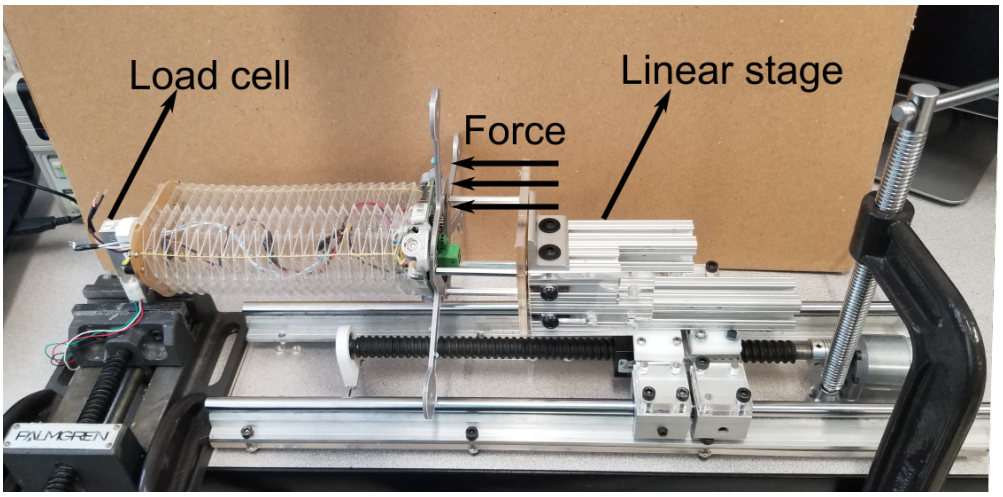

Figure 3.2: Axial loading experimental setup. The origami module was mounted to a linear stage on one end and to a load cell on the other end. The linear stage was driven using combination of a ball screw and a DC brushed motor. The linear displacement was measured using the embedded encoder attached to the motor.

TAL220) secured to a table-top vise (Figure 3.2). The linear stage was used to compress and decompress the origami body at a rate of 7.25 mm/sec. For each experiment we repeated the loading cycle for five times and over three different origami bodies. Force readings at 10-80 mm with 10 mm increment were then extracted from the raw data and processed to obtain mean and standard deviation. The axial stiffness is determined by the slope of the graph (Figure 3.4(a)).

A similar setup was used to evaluate the torsional stiffness of the origami body (Figure 3.3) for which the linear slide provided known torsional load. However, for this experiment we connected strings to the top plate of the origami structure at distance of 2.565 cm from the plate's centroid (moment arm). They were then routed appropriately and their ends tied to the load cell which mounted to the linear slide as well. The axial force provided by the linear slide was transformed to twisting moment due to the moment arm. We programmed the linear slide to provided force in the range of 4.45-44.5 N with 4.45 N increments, which corresponds to 0.1141-1.141 Nm. The amount of twisting (rotational displacement) was measured using the OptiTrack tracking system. We repeated the experiment three times for each of three modules. The same experiment was

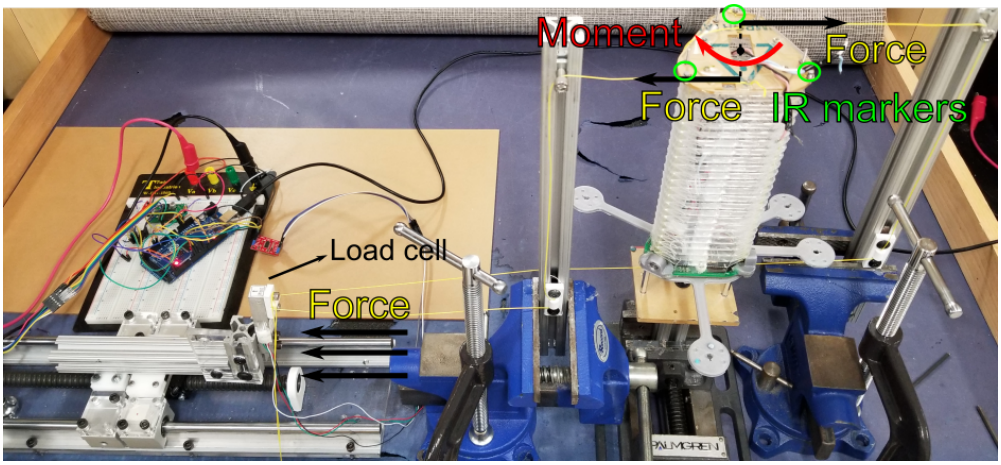

Figure 3.3: Torsion loading experimental setup. The origami module was fixed using a vise as shown. A linear stage provides known axial forces which were transmitted to the origami module through cable routing. Due to the cable routing, the origami module experienced a twisting moment. The twist angle was measured using the OptiTrack motion tracking system with the infra-red (IR) reflective markers attached to the origami end plate.

conducted on a single silicone rubber (Ecoflex-30) actuator up to 0.434 Nm torque. We then extracted the mean and standard deviation of the torsion-angular displacement from the raw data (Figure 3.4(c)). The slope of the curve represents the torsional stiffness of the bodies.

The tubular origami structure discussed in this chapter has a longer axial dimension while maintaining the same radial size as the previous version. We measured 261.25 N/mm and 0.448 Nm/deg for the axial and torsional stiffness as shown in Figure 3.4(a) and 3.4(c). Furthermore, the resilience of the module was evaluated through axial cyclic loading of 1000 cycles, from which the force and linear displacement data were collected. For each cycle we calculated the axial stiffness by linearly fitting the force-displacement data points. We observe a maximum change of 3.14 % (Figure 3.4(b)) in the axial stiffness suggesting that no significant degradation due to plastic deformation is present. In order to better contrast the torsional stiffness of the origami module to the typical soft actuator, we also conducted torsional loading experiment on a 3-chamber bending actuator developed in [75], with radius of 15.5 mm and made of Ecoflex-30 silicone rubber (Figure 3.4(d)). As shown in Figure 3.4(c), we observe about 73 times higher torsional stiffness in the origami module compared to

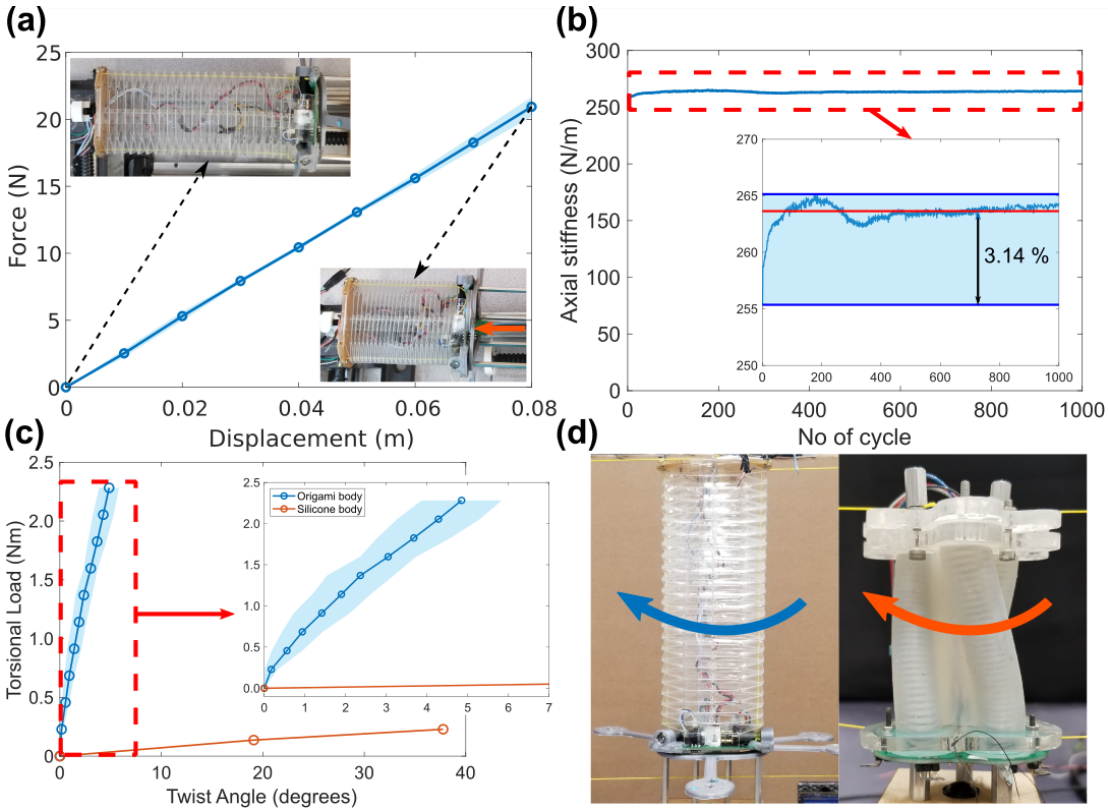

Figure 3.4: (a) Axial stiffness of origami actuator, (b) evolution of origami module's axial stiffness over 1000 loading cycles, (c) torsional stiffness of origami and silicone actuator, (d) origami and silicone actuator under torsional load.

the silicone counterpart and 70 times higher (2.71 rad/Nm) than reported in[76], despite its comparatively low mass. The summary of the origami module's property is presented in Table 3.1.

3.3 Multi-Section Inverse Kinematics

In the previous chapter, it was shown that we can control the shape of the origami continuum module by tracking appropriate tendon lengths. Furthermore, we connected two origami modules in series and commanded them to follow a circular tip trajectory while keeping the top plate parallel to the ground, only using simple control inputs. Expanding from that, we need a way to generalize the solution for an n-module continuum robot. To the best of our knowledge, there is currently no

Table 3.1: Physical properties and performance of second generation origami module.

Properties	Value	Unit
Size		cm
Diameter	8.0	cm
Uncompressed length	18.0	cm
Fully compressed length	8.0	cm
Total module weight	135.0	gram
Origami body	48.0	gram
Motors	38.1	gram
Printed circuit board	36.5	gram
Wires & others	12.4	gram
Maximum bending angle	95.5	deg
Axial stiffness	261.25	N/m
Torsional stiffness	0.448	N.m/deg

closed-form solution for the inverse kinematics of a multi-section continuum robot due to its highly redundant nature. Velocity-based and numerical methods have been promising as a solution for inverse kinematics of traditional rigid robots. For the velocity-based approach, one can construct the robot's Jacobian as done in [64] and utilize it to incrementally bring the robot to its desired pose.

A continuum section can be represented as a circular arc in 3-D space with its center in the X-Y plane. The proximal point is located at the origin while the distal point is located in 3-D space. Each continuum segment can be fully described by three configuration parameters: arc length s, bending angle θ, and bending direction φ. The forward kinematics relating the configuration and task spaces of a single continuum segment can be defined with homogeneous transformation matrix $\mathbf{T}(s, \theta, \varphi)$.

$$\mathbf{T} = \begin{bmatrix} C_\varphi C_\varphi C_\theta + S_\varphi S_\varphi & C_\varphi S_\varphi (C_\theta - 1) & C_\varphi S_\theta & C_\varphi (1 - C_\theta)/\kappa \\ C_\varphi S_\varphi (C_\theta - 1) & S_\varphi S_\varphi C_\theta + C_\varphi C_\varphi & S_\varphi S_\theta & S_\varphi (1 - C_\theta)/\kappa \\ -C_\varphi S_\theta & -S_\varphi S_\theta & C_\theta & S_\theta/\kappa \\ 0 & 0 & 0 & 1 \end{bmatrix} \tag{3.1}$$

where $C_x = \cos(x), S_x = \sin(x)$. The mathematical model describing the forward kinematics of continuum robots involves non-linear terms with cosine and sine functions. This results in computationally intensive calculations when finding the Jacobian by taking partial derivatives. Furthermore, when translated to joint configuration (tendon lengths), singularity is reached when all the lengths are equal. Godage et al. proposed to approximate the trigonometry terms with Taylor series which results in polynomial terms that are easily differentiable[64]. In this work, we approximated the terms with 10^{th} degree Taylor series that corresponds to a maximum error of 0.05 % given a maximum bending angle of π radians. For a n-section continuum robot, the full forward kinematics is

$$\begin{aligned}
\mathbf{T}_0^{\mathbf{tip}} &= \mathbf{T}_0^1 \mathbf{T}_1^2 ... \mathbf{T}_{\mathbf{n}-1}^{\mathbf{tip}} \\
&= f(\vec{q_S}) = f(s_1, \theta_1, \varphi_1, ..., s_n, \theta_n, \varphi_n) \\
&= f(\vec{q_L}) = f(l_{11}, l_{12}, l_{13}, \ldots, l_{n1}, l_{n2}, l_{n3}) \\
&= \begin{bmatrix} \boldsymbol{\Theta}_\mathbf{n} & \vec{\Psi}_n \\ 0_{1\times 3} & 1 \end{bmatrix}
\end{aligned} \tag{3.2}$$

where $\boldsymbol{\Theta}_\mathbf{n} \in SO(3)$ is the rotation matrix and $\vec{\Psi}_n = \left[\Psi_{nx}, \Psi_{ny}, \Psi_{nz}\right]^T \in \Re^{3\times 1}$ is the position vector. The Jacobian is then defined as $\mathbf{J} = [\mathbf{J}^\mathbf{v}; \mathbf{J}^{\boldsymbol{\omega}}] \in \Re^{6\times 3n}$ where $\mathbf{J}^\mathbf{v} = \vec{\Psi}_{n,\vec{q_L}}$ and $\mathbf{J}^{\boldsymbol{\omega}} = (\boldsymbol{\Theta}_{\mathbf{n},\vec{q_L}}\ \boldsymbol{\Theta}_\mathbf{n}{}^T)^\vee$. The operator $D_{,x}$ corresponds to the partial derivative of D with respect to x. In the case where D is a matrix or a vector, the operator $D_{,x}$ indicates taking the partial derivative for each element of D with respect to x. The operator $(\mathbf{A})^\vee$ is to construct a 3×1 vector from non-zero

elements of a skew symmetric matrix $\mathbf{A}$. Given these operators we then have for example,

$$
\begin{aligned}
(\boldsymbol{\Theta}_{\mathbf{n}},_{l_{11}}\boldsymbol{\Theta}_{\mathbf{n}}{}^{T})^{\vee} &= \left(\begin{bmatrix} \Theta_n(1,1),_{l_{11}} & \Theta_n(1,2),_{l_{11}} & \Theta_n(1,3),_{l_{11}} \\ \Theta_n(2,1),_{l_{11}} & \Theta_n(2,2),_{l_{11}} & \Theta_n(2,3),_{l_{11}} \\ \Theta_n(3,1),_{l_{11}} & \Theta_n(3,2),_{l_{11}} & \Theta_n(3,3),_{l_{11}} \end{bmatrix} \begin{bmatrix} \Theta_n(1,1) & \Theta_n(2,1) & \Theta_n(3,1) \\ \Theta_n(1,2) & \Theta_n(2,2) & \Theta_n(3,2) \\ \Theta_n(1,3) & \Theta_n(2,3) & \Theta_n(3,3) \end{bmatrix} \right)^{\vee} \\
&= \begin{bmatrix} 0 & -\mathrm{Z}_{3l_{11}} & \mathrm{Z}_{2l_{11}} \\ \mathrm{Z}_{3l_{11}} & 0 & -\mathrm{Z}_{1l_{11}} \\ -\mathrm{Z}_{2l_{11}} & \mathrm{Z}_{1l_{11}} & 0 \end{bmatrix}^{\vee} \\
&= \begin{bmatrix} \mathrm{Z}_{1l_{11}} \\ \mathrm{Z}_{2l_{11}} \\ \mathrm{Z}_{3l_{11}} \end{bmatrix}
\end{aligned}
\tag{3.3}
$$

where $\Theta_n(i,j)$ is the i^{th} row and j^{th} column element of matrix $\boldsymbol{\Theta}_{\mathbf{n}}$. The complete Jacobian matrix is then shown below,

$$
\mathbf{J} = \begin{bmatrix} \Psi_{nx,l_{11}} & \Psi_{nx,l_{12}} & \Psi_{nx,l_{13}} & \cdots & \Psi_{nx,l_{n1}} & \Psi_{nx,l_{n2}} & \Psi_{nx,l_{n3}} \\ \Psi_{ny,l_{11}} & \Psi_{ny,l_{12}} & \Psi_{ny,l_{13}} & \cdots & \Psi_{ny,l_{n1}} & \Psi_{ny,l_{n2}} & \Psi_{ny,l_{n3}} \\ \Psi_{nz,l_{11}} & \Psi_{nz,l_{12}} & \Psi_{nz,l_{13}} & \cdots & \Psi_{nz,l_{n1}} & \Psi_{nz,l_{n2}} & \Psi_{nz,l_{n3}} \\ \mathrm{Z}_{1l_{11}} & \mathrm{Z}_{1l_{12}} & \mathrm{Z}_{1l_{13}} & \cdots & \mathrm{Z}_{1l_{n1}} & \mathrm{Z}_{1l_{n2}} & \mathrm{Z}_{1l_{n3}} \\ \mathrm{Z}_{2l_{11}} & \mathrm{Z}_{2l_{12}} & \mathrm{Z}_{2l_{13}} & \cdots & \mathrm{Z}_{2l_{n1}} & \mathrm{Z}_{2l_{n2}} & \mathrm{Z}_{2l_{n3}} \\ \mathrm{Z}_{3l_{11}} & \mathrm{Z}_{3l_{12}} & \mathrm{Z}_{3l_{13}} & \cdots & \mathrm{Z}_{3l_{n1}} & \mathrm{Z}_{3l_{n2}} & \mathrm{Z}_{3l_{n3}} \end{bmatrix}
\tag{3.4}
$$

Given the complete Jacobian for the n-section continuum robot, we then constructed damped least-squares Jacobian, $\mathbf{J_{damped}} = \mathbf{J}'(\mathbf{J}\mathbf{J}' + \lambda_{damp}^2\,\mathbf{I})^{-1}$, where $\mathbf{J}'$ is the Jacobian transpose. The damped least-squares Jacobian provides better robustness against divergent behavior near singularity compared to the pseudo-inverse Jacobian. However, one still needs to pick appropriate damping coefficient λ_{damp} to prevent the system from exploding. We use variable damping factor as investigated in[77] to pick the value of λ_{damp} at each iteration.

$$\lambda_{damp}^2 = \begin{cases} 0 & when \quad \sigma_{min} > \varepsilon_\lambda \\ \left(1 - \left(\frac{\sigma_{min}}{\varepsilon_\lambda}\right)^2\right) \lambda_{max}^2 & otherwise, \end{cases} \tag{3.5}$$

where σ_{min} is the smallest singular value of $\mathbf{J}$ obtained from singular value decomposition, ε_λ defines the size of the singular region, and λ_{max} is left at user's disposal. Starting from arbitrary initial values we iterated through the expression below until norm of the error was smaller than some tolerance value (0.01) or if the maximum number of iteration (5000) has been reached.

$$\vec{q_L}^{\,i+1} = \vec{q_L}^{\,i} + \mathbf{J_{damped}} * [\vec{e_p}; \vec{e_o}]^T, \tag{3.6}$$

where e_p and e_o are the 3×1 position and orientation error vectors respectively, and $\vec{q_L}$ is the tendon lengths vector. Position error is defined as the substraction of current tip position from desired tip position while the orientation error is defined as the necessary rotation that will bring current tip orientation to the desired tip orientation, represented in axis-angle form. The current tip position and orientation as a function of tendon lengths are defined by the forward kinematics of multi-section continuum robot.

We opted for an optimization-based method to achieve smooth trajectory control due to more freedom available in controlling the behavior of the robot in addition to tracking the desired path. More importantly, no gain tuning is required, which we found to be a significant contributor to the behavior of simpler damped least squares gradient descent solutions. Furthermore, we can use constraint functions to ensure that the solutions are within the actuator limits determined experimentally during calibration. We define the specific optimization problem to be solved as:

$$\begin{aligned} \min_{\vec{q_L}} \quad & C \\ \text{s.t.} \quad & q_{Lmin} \leq \vec{q_L} \leq q_{Lmax}, \end{aligned} \tag{3.7}$$

where C is the cost function and q_{Lmin} and q_{Lmax} are the minimum and maximum tendon lengths, respectively. We investigated three different cost functions defined below:

$$\begin{aligned} Cost\,1 &= w_p \left|\vec{e_p}\right|^2 + w_o \left|\vec{e_o}\right|, \quad w_p + w_o = 1 \\ Cost\,2 &= \textstyle\sum_{i=1}^{n} (l_{i1} - l_{i2})^2 + (l_{i1} - l_{i3})^2 + (l_{i2} - l_{i3})^2 \\ Cost\,3 &= \textstyle\sum_{i=1}^{n} (l_{i1} - l_{i1\_prev})^2 + (l_{i2} - l_{i2\_prev})^2 + (l_{i3} - l_{i3\_prev})^2 \end{aligned} \tag{3.8}$$

where w_p and w_o are some scalar weighting for the error terms, (l_{i1}, l_{i2}, l_{i3}) are the tendon lengths for the i^{th} module, and $(l_{i1\_prev}, l_{i2\_prev}, l_{i3\_prev})$ are the tendon lengths for the i^{th} module obtained in previous iteration. We investigated three different cost functions that minimize: the difference between the actual and desired robot tip pose in $SE(3)$ while satisfying the actuator's constraint (Cost 1: Minimize Pose Error), the curvature for each module (Cost 2: Minimize Curvature), and the change in cable lengths between the solution guess steps hence allowing for a smoother result (Cost 3: Minimize Step). Furthermore, equality constraints of $\vec{e_p} = 0$ and $\vec{e_o} = 0$ were introduced to the second and third cost functions. In other words, Cost 1 minimizes the tracking error and uses constraints to limit the solutions to reachable sets, while Cost 2 and Cost 3 aim to minimize shape changes and use constraints to converge to the desired tip poses. We utilized the optimization solver function `fmincon` of MATLAB for all of our optimization problem formulations discussed previously.

The solutions of inverse kinematic solvers from different methods discussed above are presented in Figure 3.5(a). Here we show representations of the tendon lengths of a single continuum module (Figure 3.5(b)) for a clear comparison, with each method color coded (with the complete tendon variations shown in Figure 3.6). At first glance, we can see that the solutions provided by the gradient descent and the third cost function (minimize step) are smoother than the rest. We focus on achieving smooth cable-length transients, since rapid changes would cause vibrations and re-

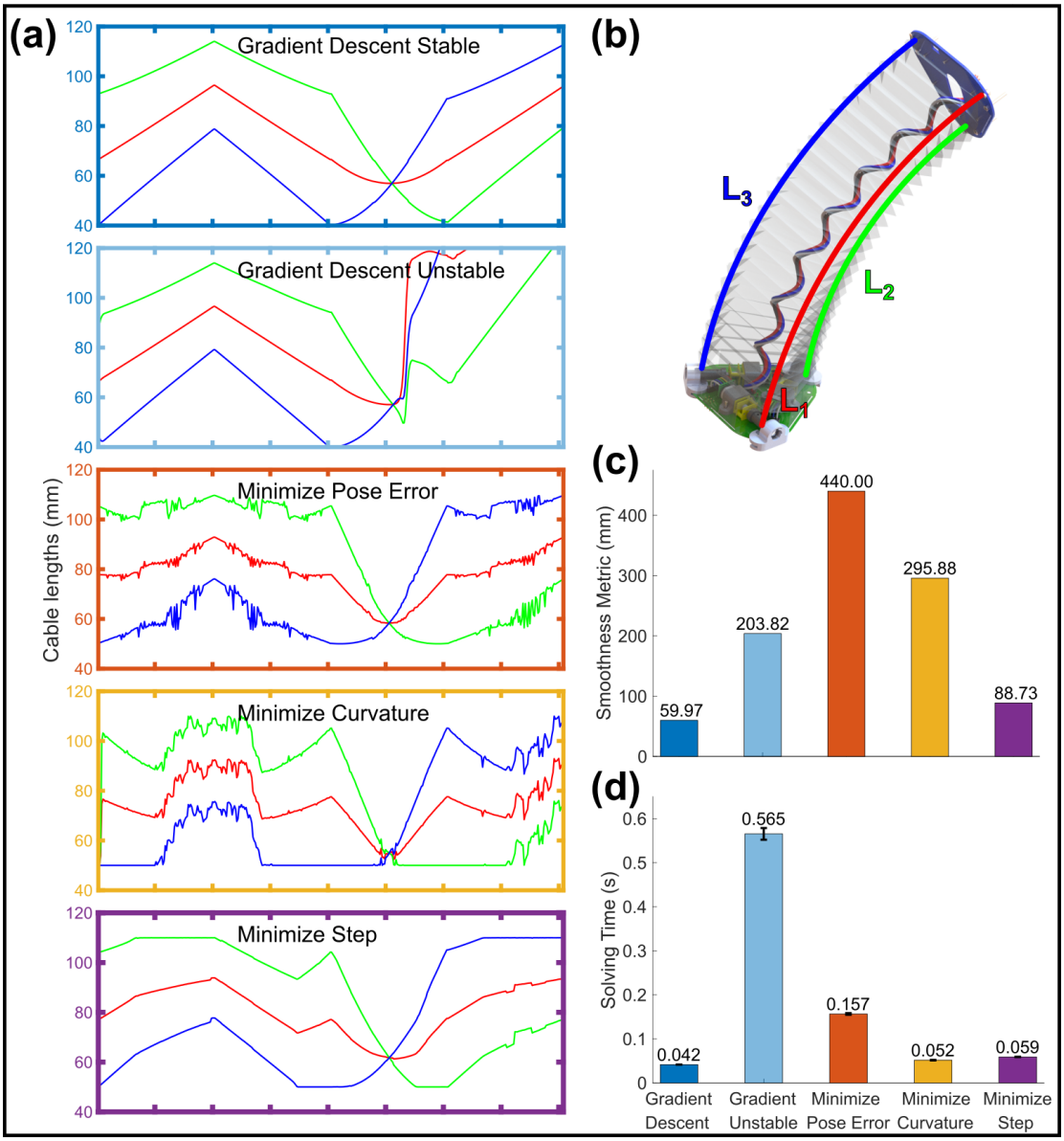

Figure 3.5: (a) Inverse kinematics solution for a single origami module provided by different methods. (b) Schematic showing definition of joint configuration for a single module. (c) Comparison of solutions smoothness. (d) Average solving time per step for each inverse kinematics method.

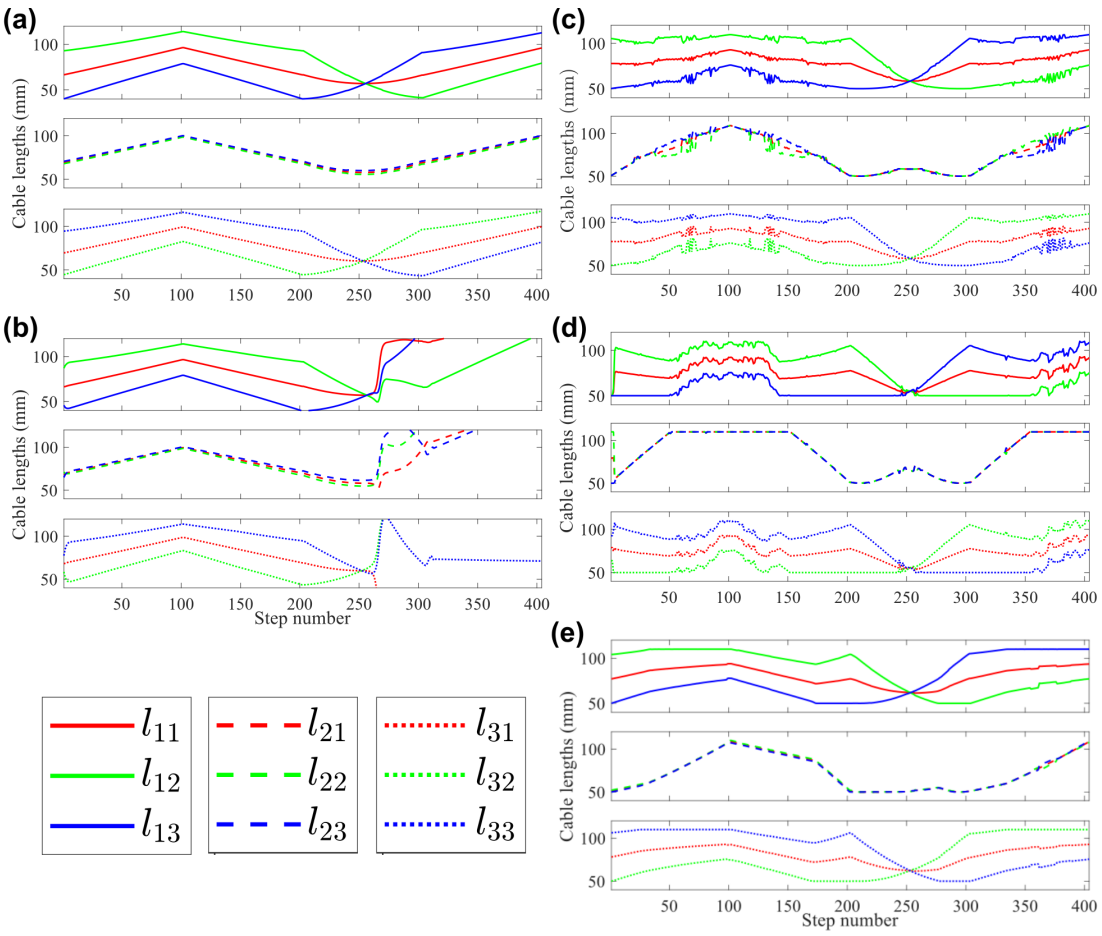

Figure 3.6: The complete solution of tendons variation generated by the inverse kinematics solver with different approaches: (a) gradient descent stable, (b) gradient descent unstable, (c) optimization with pose error as the cost function, (d) optimization to minimize curvature, (e) optimization to minimize change in tendon lengths between iterations.

duce precision. To further quantify the quality of the solution, we defined jerkiness metric as the sum of cable lengths differences between iteration steps with the results shown on the bar chart (Figure 3.5(c)). As seen in this panel, the solution provided by the gradient descent method is the smoothest when stable; however, when the gain is not carefully chosen the system may become unstable. The third smoothness optimizing cost function outperformed the other cost functions while still slightly lagging behind the best-case gradient descent method.

We also evaluated the solving time of the inverse kinematic solvers. For each method we used the solvers to find necessary tendon lengths that will achieve the same tip path. The mean and standard deviation of the solving time for 50 repetitions each are summarized in the bar chart (Figure 3.5(d)). The gradient descent method with suitable damping coefficient performed the best with 0.042 seconds per step while the gradient descent method with unsuitable damping coefficient performed the worst with 0.565 seconds. The second and third cost functions performed similarly with the former being slightly faster at 0.052 seconds. Given the similar smoothness and time performance to the gradient descent method minus the instability problem, we decided to pick the third cost function as the final inverse kinematics solver. Figure 3.7(a) shows the complete tendon lengths variation over time solved with our proposed inverse kinematics solver. The solution corresponding to the robot's motion for a pick-and-place application is depicted in Figure 3.7(b) (simulated in MATLAB). The robot is shown approaching the object, picking it up, and then transporting it to another location while maintaining its orientation parallel to the ground.

3.4 Feedback Control

Two common approaches used to achieve the control of robotic system include model-based and feedback control through sensing. Unfortunately, a perfect mathematical model is rarely available and there is a trade-off between the model accuracy and complexity. Furthermore, the problem is

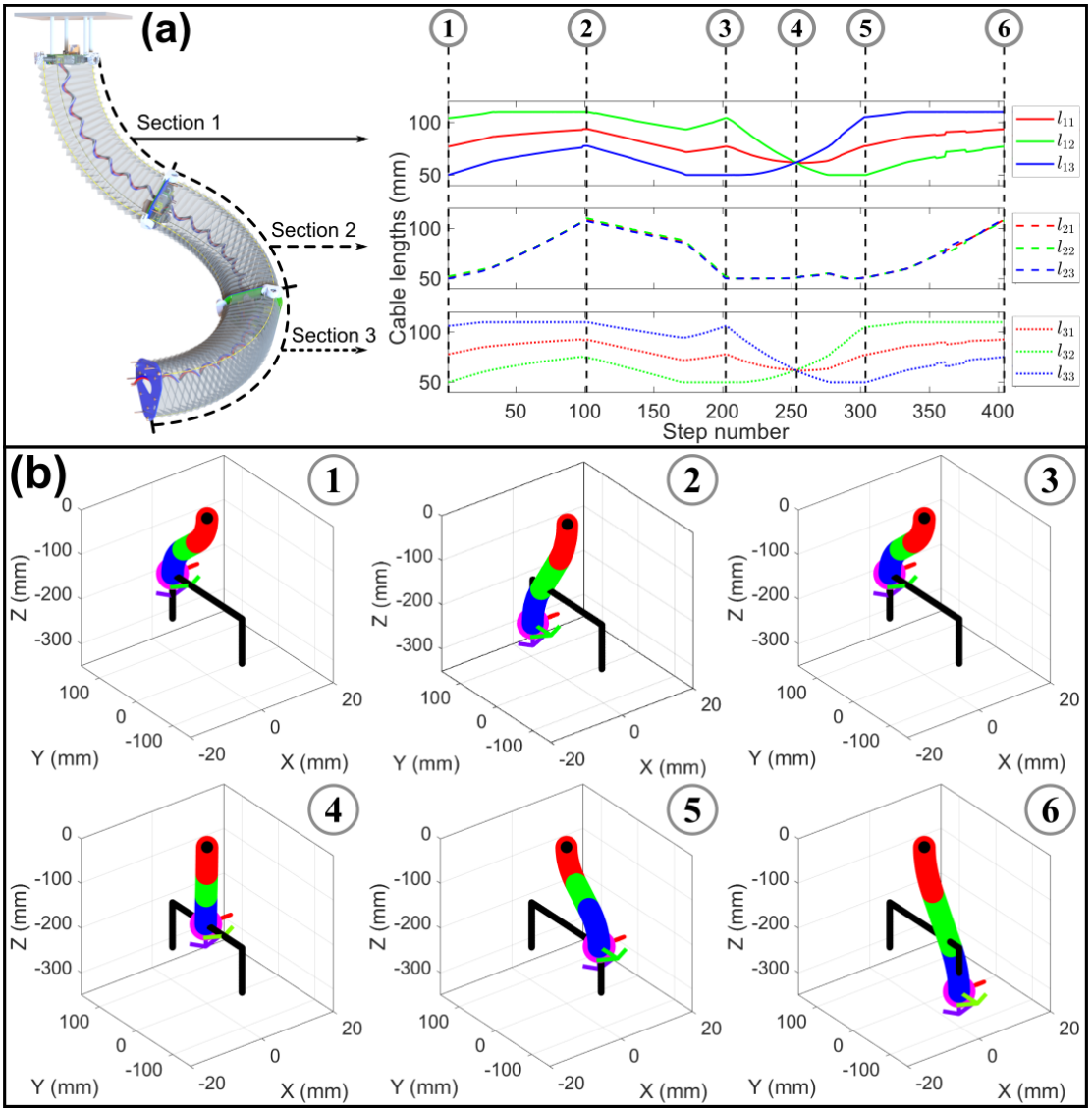

Figure 3.7: (a) Inverse kinematics solution for the three-section continuum manipulator executing a pick-and-place motion. (b) Snapshot of the robot motion in simulation with the cost function that minimize motion between time steps.

amplified by the low-repeatability of soft actuators due to small variations in the manual fabrication process. In contrast, feedback sensing alone is often not enough, especially if the sensors are noisy and high feedback gain will tend to make the system unstable. Moreover, a proprioceptive sensing methodology is essential if we plan to eventually deploy the robotic system outside the laboratory environment. The real world is very complex, and it is impossible to account for everything in the model. However, with a sufficiently accurate model combined with a feedback system, we can expect to achieve improved performance.

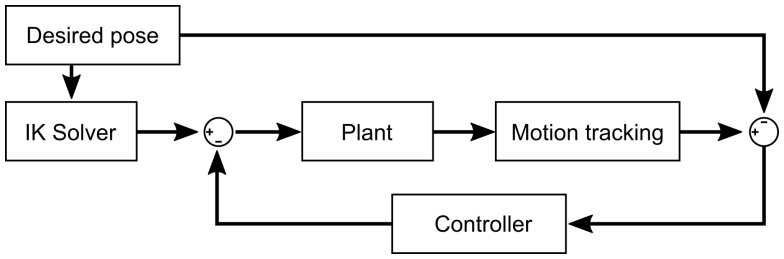

Figure 3.8: Feedback control architecture. The multi-segment inverse kinematics solver returns the initial control signal for the robot based on the desired pose. The error signal is obtained by taking the difference between the desired and measured robot's tip position and orientation. The error signal is then multiplied by the Jacobian of multi-segment continuum manipulator and fed back to the control plant.

In this work we provided the feedback to the robot using the OptiTrack motion capture system. It is important to note that our long term goal is to deploy the proposed continuum robot outside the lab; however, the motion capture system was used to illustrate how feedback control could be implemented and how beneficial it would be in reducing positioning errors. On the other hand, it is reasonable to assume that some industrial applications may find ways to use camera systems to monitor the robot motion. A proprioceptive sensor such as one to be introduced in the later chapter could be used to replace the external motion tracking system. We fixed the robot at the base and mounted four IR-reflective markers to the distal end allowing us to track the robot end point. The difference between the tracked robot's tip pose and desired pose was then used as the error signal. As traditionally done in robot manipulator control, we multiply the error signal by the robot Jacobian

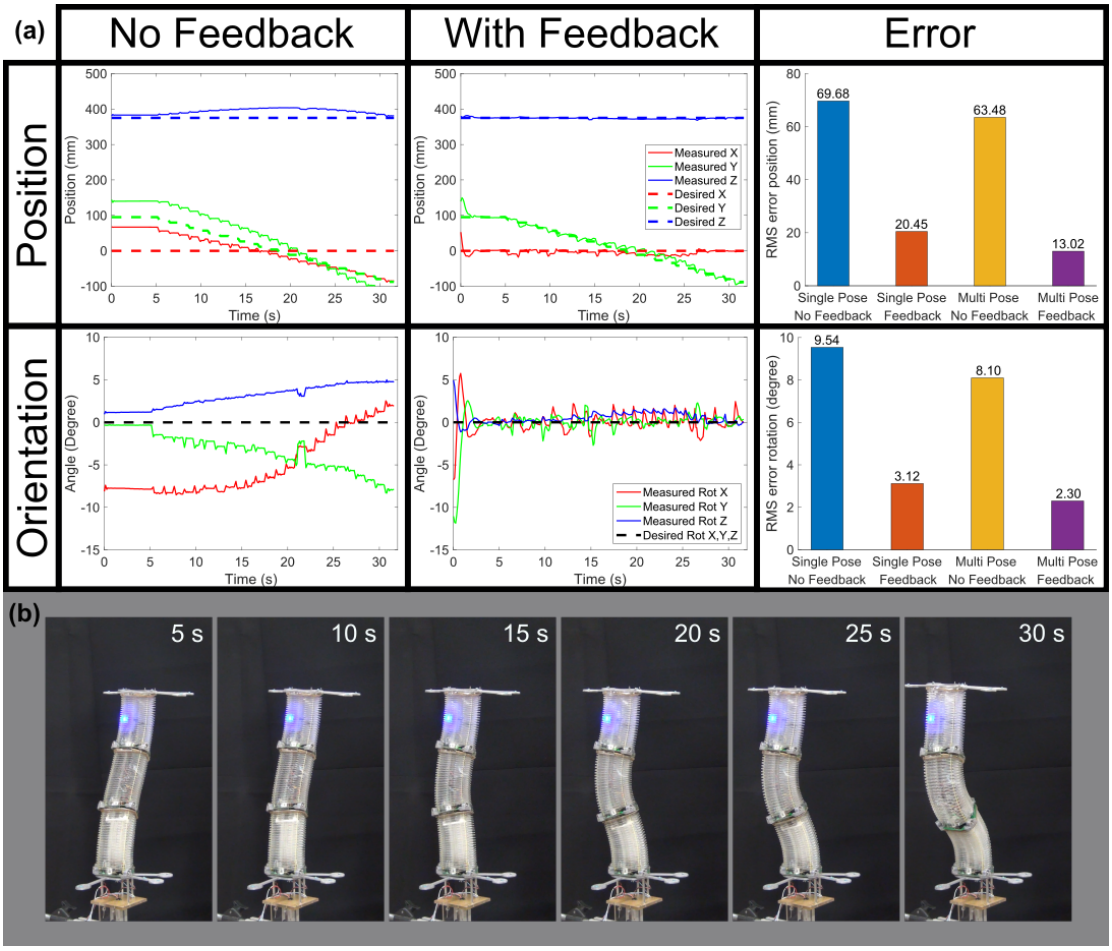

Figure 3.9: (a) Evolution of robot's tip position and orientation without and with feedback for multi-pose tracking. Root-mean-square errors for position and orientation are summarized on the bar charts. (b) Snapshot of the robot following a straight line path while maintaining tip orientation parallel to the ground (multi-pose tracking).

discussed in the previous section to drive the system to zero error in configuration space (Figure 3.8).

Figure 3.9(a) shows the evolution of the robot's tip pose without feedback (left) and with feedback (center). Using feedback, the robot was able to traverse in a straight line while maintaining the top plate parallel to the ground as shown in Figure 3.9(b). The feedback is able to reduce the error about 5-fold for the position and 2.5-fold for orientation tracking. Moreover, the system converged to steady state within 2 seconds.

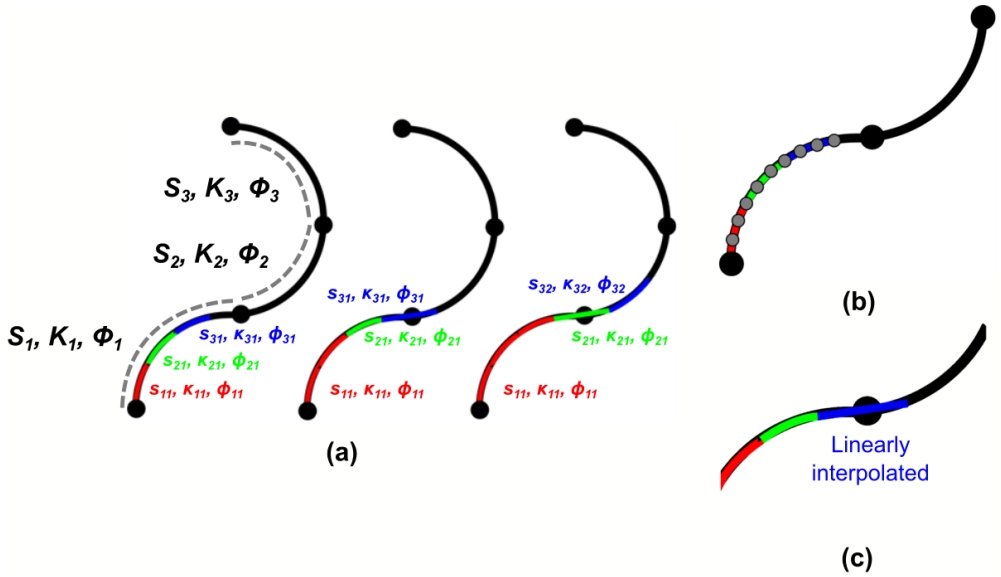

Figure 3.10: (a) Grow-to-shape motion at which the growth starts at the base module, (b) optimization approach in which the desired path and robot modules are discretized into M points, (c) heuristic approach in which the transitioning module linearly interpolates the parameters (curvature and bending direction) describing two adjacent desired path segments.

3.5 Grow-to-Shape Algorithms

A significant advantage of the proposed origami continuum arm is its ability to change length, which enables functions that are simply not possible with existing rigid arms. We propose an algorithm we call "Grow-to-Shape" that will allow the continuum robot to incrementally increase its length while following a certain desired shape and minimizing the deviation from a path, which also becomes the final shape of the robot. Continuum robots with collapsible modules can benefit from a smaller deviation in path-following compared to their inextensible counterparts. In this work, we assume that the continuum robot will grow from the base to the tip module (Figure 3.10(a)).

Growing the base module first is intuitive because then a shorter (tip) section will go through the transition between the desired path segments. If we grow the tip module first then a longer (tip) section will have to go through the transition, this will contribute to a larger deviation from the path.

Alternatively, if we want to grow the tip module first then we can re-shrink it back before the transition. However, due to the additional motions from the module is necessary, this approach is less efficient. Moreover, the desired robot path consists of constant curvature arcs within the curvature limits of the modules, and pre-determined by some other path planning algorithm.

We defined the desired robot path/shape to be a set of arc parameters,

$$P = \vec{q_S}_{desired} = \{S_1, K_1, \Phi_1, ..., S_n, K_n, \Phi_n\}$$

and formulated the optimization problem as below,

$$\begin{aligned} \min_{\vec{q_S}} \quad & \lambda_{path}\, e_{path} + \lambda_{tip}\, e_{tip} \quad , \\ \text{s.t.} \quad & \vec{q_{Smin}} \leq \vec{q_S} \leq \vec{q_{Smax}} \end{aligned} \tag{3.9}$$

where e_{path} and e_{tip} are the path and tip errors respectively while λ_{path} and λ_{tip} are scaling factors for each error term with a constraint of $\lambda_{path} + \lambda_{tip} = 1$. Moreover,

$$\vec{q_{Smin}} = \{\min\{K_1, ..., K_n\}, \min\{\Phi_1, ..., \Phi_n\}\}$$

$$\vec{q_{Smax}} = \{\max\{K_1, ..., K_n\}, \max\{\Phi_1, ..., \Phi_n\}\}.$$

We utilized the forward kinematics of the continuum robot as a function of arc parameters ($\vec{q_S}$) for the optimization problem formulation. The solution (arc parameters) was then converted to appropriate tendon length configuration. To define the e_{path}, we discretized each robot segment into M points along the continuum backbone and subtracted their coordinates from coordinates of equivalent points on the desired path (Figure 3.10(b)). In our study, we chose $M = 10$ and $\lambda_{path} = 0.8$.

As an alternative to the optimization-based method, we also devised a heuristic approach (Fig-

ure 3.10(c)) with which we command the module transitioning from one segment to the other by linearly interpolating the arc parameters of the two neighboring desired segments as given below,

$$\begin{cases} \varphi_{mi} = \frac{\sum_{j=1}^{i} S_j - \sum_{k=1}^{m-1} s_k}{\sum_{k=1}^{m} s_k - \sum_{k=1}^{m-1} s_k} \cdot (\Phi_i + \pi) + \frac{\sum_{k=1}^{m} s_k - \sum_{j=1}^{i} S_j}{\sum_{k=1}^{m} s_k - \sum_{k=1}^{m-1} s_k} \cdot \Phi_{i+1} \\ \kappa_{mi} = \frac{\sum_{j=1}^{i} S_j - \sum_{k=1}^{m-1} s_k}{\sum_{k=1}^{m} s_k - \sum_{k=1}^{m-1} s_k} \cdot (-K_i) + \frac{\sum_{k=1}^{m} s_k - \sum_{j=1}^{i} S_j}{\sum_{k=1}^{m} s_k - \sum_{k=1}^{m-1} s_k} \cdot K_{i+1} \qquad \textit{when } |\Phi_i - \Phi_{i+1}| > \pi/2 \\ \\ \varphi_{mi} = \frac{\sum_{j=1}^{i} S_j - \sum_{k=1}^{m-1} s_k}{\sum_{k=1}^{m} s_k - \sum_{k=1}^{m-1} s_k} \cdot \Phi_i + \frac{\sum_{k=1}^{m} s_k - \sum_{j=1}^{i} S_j}{\sum_{k=1}^{m} s_k - \sum_{k=1}^{m-1} s_k} \cdot \Phi_{i+1} \\ \kappa_{mi} = \frac{\sum_{j=1}^{i} S_j - \sum_{k=1}^{m-1} s_k}{\sum_{k=1}^{m} s_k - \sum_{k=1}^{m-1} s_k} \cdot K_i + \frac{\sum_{k=1}^{m} s_k - \sum_{j=1}^{i} S_j}{\sum_{k=1}^{m} s_k - \sum_{k=1}^{m-1} s_k} \cdot K_{i+1} \qquad \textit{otherwise}, \end{cases} \tag{3.10}$$

where φ_{mi} and κ_{mi} are the m^{th} module's bending direction and curvature when transitioning from desired i^{th} to $i+1^{th}$ path segments. S_j is arc length of j^{th} desired path segment, s_k is the arc length of k^{th} module, Φ_i is the i^{th} desired segment bending direction, and K_i is the i^{th} desired segment curvature. While not transitioning, the continuum module will trace the arc parameters of the desired segment where the module currently resides.

Figure 3.11 show the experimental results of the grow-to-shape algorithms implemented on the three-segment origami continuum robot for the full optimization and heuristic methods respectively. We plotted the tracked robot tip position (P3) as the robot grew to the desired "inverted-S" shape in X-Z plane (Figure 3.11(a)). Furthermore, we also tracked the tip position of two proximal segments (P1, P2) to help illustrate the overall shape of the continuum robot as we do not currently have a method to measure the complete shape of the continuum robot. The arc parameters for the final shape are $S_1 = S_2 = S_3 = 0.16\ m, K_1 = K_2 = K_3 = 4.9087\ m^{-1}, \Phi_1 = 0, \Phi_2 = \pi, \Phi_3 = \pi$. We repeated the grow and shrink motion three times for each of five trials, the first using using the optimization and the second using the heuristic methods. The diamond plot points represent the average tip positions of the distal segment for five trials with the shaded areas as standard deviations. We observed that both methods generated similar paths and the robot was able to track them with

maximum tip error of 34 mm in X axis. Figure 3.11(a) shows the snapshot of the grow-to-shape motion with the gravity vector pointing downward.

We investigated the effect of reducing the initial (minimum) continuum module length on the

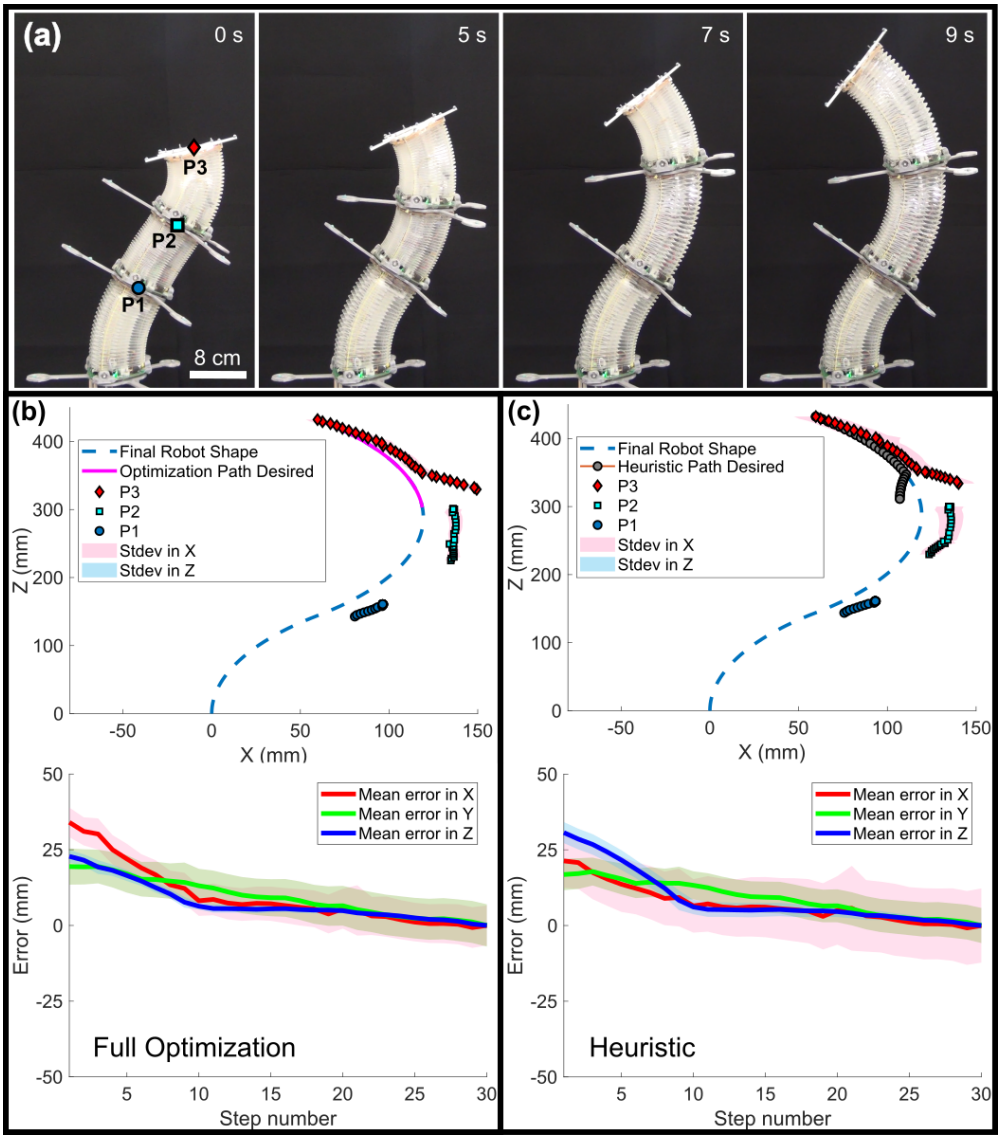

Figure 3.11: (a) Snapshot of grow-to-shape motion. (b) Experimental result of the full optimization method where the modules' tip position (P1, P2, P3) were tracked. (c) Experimental result of the heuristic method. The error plot only denotes the distal most section.

tip error, which simulates the limit of the origami module's compressed length. As expected the tip error for the heuristic method decreases for shorter initial module lengths as shown in Figure 3.12(a). In fact, the error appears to converge to the tip error obtained using the optimization method (about 0.0041 mm). This suggests that the heuristic method will work as well as the optimization approach for continuum robot capable of collapsing to 0 mm length (e.g. concentric tubes with insertion rail). We also investigated the effect of increasing the desired arc segment lengths while keeping the initial module length constant. A similar trend of decrease in tip error can be observed, although with less pronounce effect (about 2.06 mm decrease).

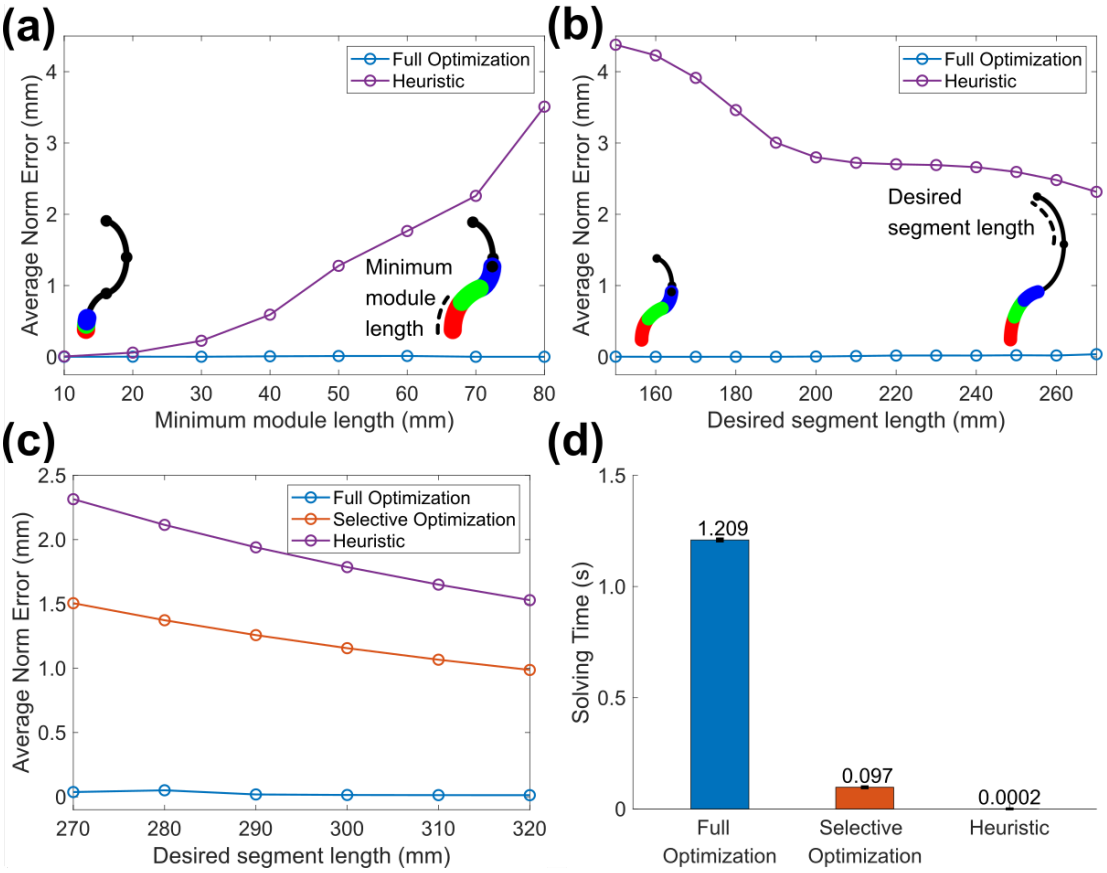

Figure 3.12: (a) Error analysis on the effect of decreasing the minimum module length, (b) and increasing the desired the segment length independently. (c) Error and, (d) solving time comparison from the three different methods.

While experimenting with the two previously discussed methods, we realized that we might be able to only do "selective optimization" for modules that are transitioning between the desired segments. However, this still requires that the desired arc segments will consist of circular arcs with constant curvature. For more complex curves, one may try to convert them first into constant curvature segments using some distance metrics. Furthermore, the selective optimization only makes sense if the desired segment length is longer than the combined initial length of the modules, otherwise full optimization is necessary. Figure 3.12(c) shows that the selective optimization method outperforms the heuristic method (about 50% lower error) while still having lower performance than the full optimization method. Moreover, the error decreases as the desired segment lengths increase (Figure 3.12(b)). While the work done in[73] does not provide a solving time measurement, we collected the solver time per step for each method for comparison (Figure 3.12(d)). The full optimization method has the least error but requires the most time due to the module discretization and redefinition of the cost function at every time step. By doing the selective optimization we can speed up the solver time about 12-fold, but there is only a small improvement in the tip error compared to the heuristic approach, which runs much faster. It is quite trivial to replace the constant curvature model used in this work with a non-constant curvature model for the optimization-based approach. However, that most likely will result in a much longer solver time.

3.6 Origami Continuum Robot Capabilities

We validate possible applications of our origami continuum robot to achieve manipulation and exploration/inspection tasks which utilize the smoothness-optimization-based inverse kinematics solver and the grow-to-shape algorithm. One potential application of continuum robots for manipulation task is to complete a pick-and-place routine. Despite possibly having a much lower accuracy compared to traditional rigid manipulators, continuum robots could be beneficial for ap-

plications where human-robot synergy is necessary e.g. collaborative assembly or packaging. In this paper, we showed that our continuum robot is capable of transporting a 0.5 kg cylindrical object (Figure 3.13(a)). The robot is equipped with a small vacuum-driven suction cup at the distal end and follows a trajectory similar to the one discussed for the pick-and-place simulation results. We observed deviation of the modules from constant curvature arcs due to the external load. This problem could be mitigated by introducing sensors that can detect non-constant curvature shapes for feedback control, however this is beyond the scope of this dissertation work.

Figure 3.13(b-d) highlights the exploration/inspection applications of our continuum robot in which it "grows-to-shape" traversing through tortuous paths. The robot successfully navigated through mockup walls with holes (Figure 3.13(b,c)) and a maze (Figure 3.13(d)). We introduced translational motion using a linear stage at the base of the continuum robot to simulate the insertion routine typically done in minimally invasive surgeries. It is important to note that we could achieve the same effect by using additional origami module at the base. Lastly, we attached a blue light-emitting diode (LED) to the robot's end effector and took a long-exposure photography of it tracing the WPI letters using the maximum-smoothness inverse kinematics solver as shown in Figure 3.13(e). The green letters are conveniently generated from the LEDs of the embedded motor encoders at the end of each module.

Discussion

The proposed origami-inspired continuum robot offers significant length change and is highly resistant in torsion while having minimal weight. A high torsional strength is beneficial to resist offset loads, which would reduce positioning accuracy even under the weight of the robot itself. Lower mass is favorable to mitigate sagging problem typically present in continuum robots. Furthermore lighter mass contributes to lower inertia which yields a more stable and safer system. We observed

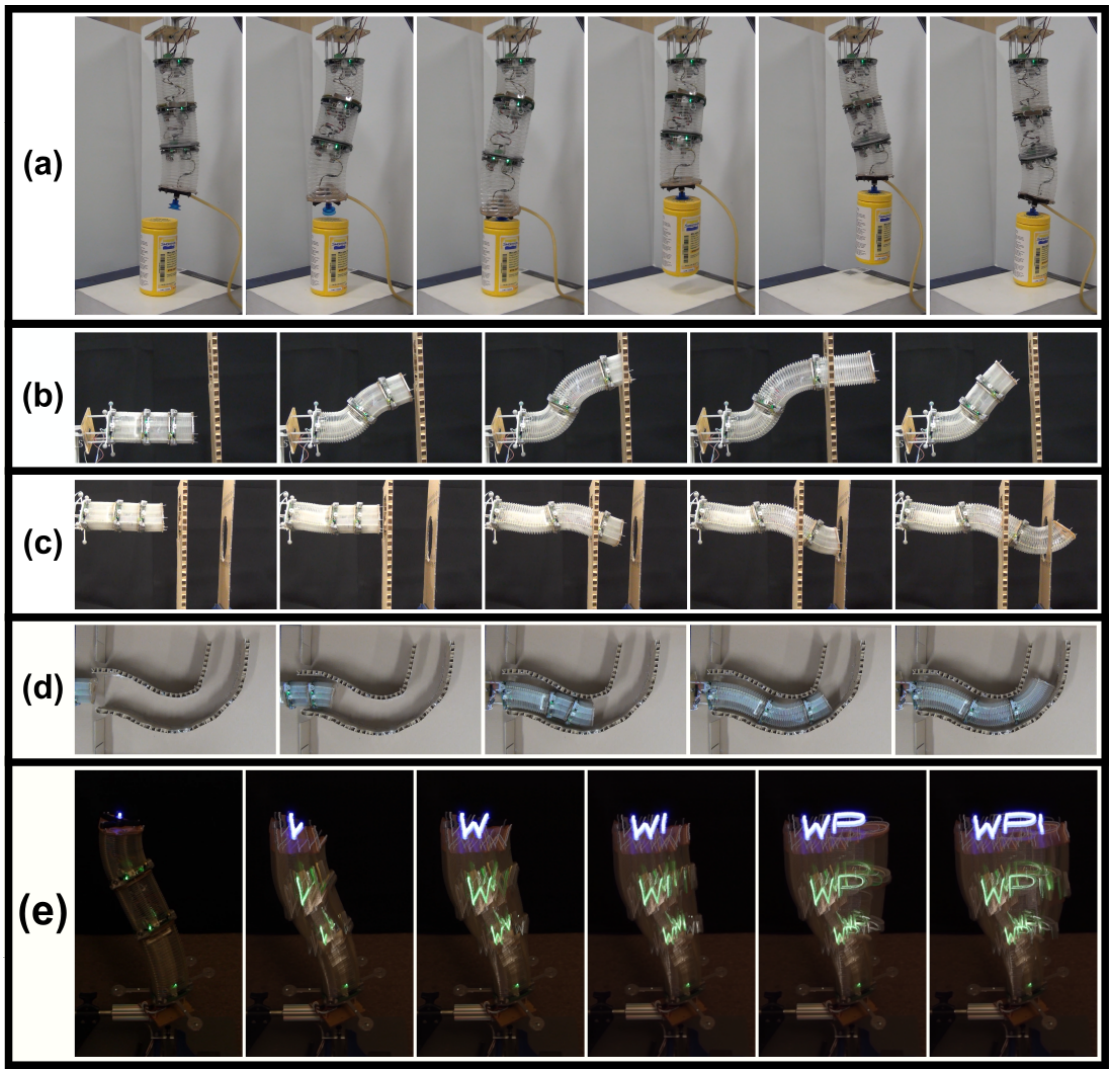

Figure 3.13: Snapshots showing capabilities of the continuum robot: (a) pick-and-place, (b) traversing through a mockup wall with a single hole (side view), (c) traversing through walls with two holes (side view), (d) grow-to-shape routine with linear slider at the base (top view), (e) end-effector path following to trace WPI letters. The direction of gravity is all pointing downward except for row d where the gravity direction is pointing into the page.

small variations in the modules' axial and torsional stiffness values suggesting good reproducibility. Additionally, the cyclic loading experiment illustrates the origami module's durability, although more rigorous testing in the range of hundred thousands cycle may be necessary.

The modular property of our robot allows for easy scalability. In order to increase its workspace, one may connect additional shorter modules in series or introduce a longer origami body for each module while keeping the same number of modules. However, stronger motors may be required as the moment arms increase as the body gets longer. In contrast with other continuum robots in which the actuators are kept at the base, the distributed actuators of our robot enable easy replacement of the broken modules. Additionally, electric powered actuation provides possibility for deployment of our soft robot outside the laboratory environment.

The optimization-based inverse kinematics solver presented in this chapter allows for the control of a multi-section continuum robot. The proposed method shows similar performance to the damped-least-squares gradient descent approach in terms of the solving time and smoothness of the cable-length (and hence robot tip) trajectories. Furthermore, the optimization method eliminates the need to tune the damping coefficient required by the gradient descent approach. The development of the inverse kinematics solver is the first step toward the possibility of a wide variety of robotic applications requiring path tracing capability. However, for time and force sensitive applications an inverse dynamic solver could be more appropriate.

We have shown the benefit of introducing feedback into the control of our robot. The initial solutions provided by the inverse kinematics solver allow for more stable system as the output of the system is already very close to the desired one. The feedback term was then used to compensate the remaining error not captured by the model. The results show that the performance of the robot was greatly improved through the addition of a motion tracking system. However, a visual-based motion tracking system tends to suffer from occlusion problems and is inherently dependent on an established system of localized cameras. A more ideal solution would be to develop a proprioceptive shape sensor that would allow for a fully deployable robotic platform.

Grow-to-Shape highlights the main benefit of a collapsible continuum manipulator compared to traditional rigid robots, which allows for navigation through tortuous paths typically present in

search-and-rescue, medical, and inspection applications. We have shown that our robot can grow to the desired shape by executing joint configurations given by the developed algorithms. We observed insignificant difference between the experimental data obtained with both full optimization and heuristic methods which is in agreement with the simulation results. We did not conduct an experiment using the selective optimization method as our modules in their current state are not capable of extending three times their minimum length (necessary for the selective optimization method) at the desired curvature value.

Lastly, we have shown the capability of the robot in various validation scenarios. Even though we focused mostly on the application of the origami continuum robot as a manipulator, the bending modules themselves are not limited only to manipulator use cases. Due to their versatility, we envision the modules could be used for bio-inspired robotic applications such as snake, worm, and flexible appendages. In fact, a hybrid robot capable of both locomotion and manipulation tasks does not seem implausible. One can imagine a snake robot capable of latching itself onto a structure and transforming into a manipulator.

4

Proprioceptive Sensing

This chapter describes the development of a sensing methodology to estimate the shape of the origami continuum robot. We start with a brief survey of current state of the art sensors specifically tailored for continuum robots and highlight their differences compared to the work proposed in this research. We continue our discussions with the details of the proposed method. In particular, we utilize a magnetic sensor to measure the deformation of the origami compliant body. Furthermore, two well known machine learning regression models are utilized to predict the robot shape both with and without external load. The model performance is then evaluated and recommendations are presented for future work.

4.1 Background and Related Work

Perception is essential for achieving a more reliable and capable robotic system. Sensing modality generally can be divided to exteroception and proprioception at which the former concerns about surrounding information while the latter focuses on measurement of robot's internal state. The focus of this research will be on the latter as it will allow for a more deployable robotic system. Proprioceptive sensing in soft robots is challenging due to the fact that a soft system has theoretically infinite degrees of freedom, and the addition of sensors is desirably not to alter this behavior. In our case, sensing is even more challenging because the origami module is capable of significant length change so methods that depend on limited strain reading for example cannot be employed.

Various existing sensing modalities for soft robots include: resistivity[78,79], capacitance[80,81], inductance[82], optical fiber[83,84], magnetic[85,86,87,88], vision[89,90,91]. Recent review can be found in[92]. As the name suggests, the resistive based method involves measuring changes in resistance typically caused by application of strain to the materials. Chen et al. for example utilize polyurethane embedded with carbon black to transform the strain measurement into resistance value[78]. As previously mentioned, a resistive based method is not suitable for the proposed origami continuum robot which can undergo significant change in length. Furthermore, resistive based sensors tend to suffer from drift and hysteresis problems. Similarly, measurement of other electrical properties such as capacitance and inductance has been employed and shown promising results[80,81,82]. However, capacitance and inductance measurements are not as straight forward as for resistance and are sensitive to the presence of conductive objects. Generally, additional electrical circuitry is required thus increasing the system complexity.

Optical fibers, which are typically flexible, have been used in[83,84] due to their superior capability in measuring strain even in micrometer scale. However, it is difficult to implement them into an embedded system due to generally bulky back-end hardware (interrogator) required to collect and

process the data. Thus optical fiber based sensing is more appropriate for stationary applications (e.g. minimally invasive surgery). Furthermore, since the origami module can undergo significant compression, the chosen sensor needs to be able to accommodate that. A more complex arrangement of fiber optics e.g. spiral or helical might be necessary.

Camarillo et al. presented vision based shape sensing using three camera in a green-screen environment[89]. The system bandwidth of the system is limited to 1-2 Hz range and it is unclear if the sensing performance would extend well to the real world environment where there are other objects nearby. Additionally, although external sensors can provide accurate results, they are large and require either line-of-sight for cameras or special environments without magnetic objects in the case of electromagnetic sensors.

Sensing methodology utilizing magnetic measurement to measure bending curvature has been explored in[85,86], in which a Hall effect sensing integrated circuit (IC) is embedded into a soft silicone module. Other magnetic based sensing involves external magnet detectors which typically have a limited workspace. Song et al. estimated the arc parameters through analytical model of Bezier curve of second and third order[87,88]. But this approach requires knowing the position and direction of the proximal and distal plates of the robot. Furthermore, the length of the robot needs to be known (fixed length) while our origami continuum robot is capable of significant length change that needs to be predicted as well. Magnetic sensors provide several advantages such as contactless operation, compact in size, low cost, and easy to integrate with embedded systems. However, the adverse effect of exposure to external magnetic interference and ferromagnetic object needs to be addressed.

In terms of modeling, there are typically two approaches: analytical and numerical (finite element analysis) with the former providing a more exact solution than the latter. However, analytical model is usually difficult to come by. Numerical method on the other hand usually requires huge computation resource and most models are application dependent. More recently, machine learning models have shown promising results in helping researchers to construct predictive models for sensing pur-

poses[83,90,91,93,94]. The problem of neural network learning can be seen as a function optimization problem, where we are trying to determine the best network parameters (weights and bias values) in order to minimize network error. There is a trade off between machine learning model and analytical model. As the complexity of the analytical model increases the solving time will also increase. In contrast, for the machine learning model it maybe more time consuming in the beginning due to the data collection and training of the model, but the solving time could be faster because the model most likely will come in the form of a linear combination of weighted sum of the inputs plus bias. Using the trained model, the input from sensor will then be translated to a predicted output.

The novel contributions presented in this chapter are:

- Development of a proprioceptive magnetic-based shape sensing suitable for extensible continuum robots.
- Machine learning predictive models to estimate the robot shape parameters.
- Validation of the sensor accuracy both with and without external load.

4.2 Methodology

As discussed in the previous chapter, a closed-loop control of the origami continuum robot is achieved through the use of a motion tracking system. The following sections will describe in detail the components necessary for the proposed proprioceptive sensing methodology.

4.2.1 Sensor Design

The shape sensing proposed in this work consists of two 7/16" × 1/32" Neodymium magnets and the Melexis 90393 magnetometer board (Adafruit Industries). This particular magnetometer board is chosen for the magnetic sensing due its wider sensitivity range (± 5-50 mTesla) and is capable of

measuring the magnetic flux density in 3 orthogonal directions (B_x, B_y, B_z). The magnet and the sensor are suspended inside the origami foldable body by utilizing 3-D printed centerpieces and detachable arms as shown in Figure 4.1. The centerpieces house the magnet and magnetometer while the arms allow for ease of mounting. The arms feature compliant tips which are inserted into the holes at the corners of the origami body. Furthermore, an appropriate slot at the tip of the arms allows for the actuation cables to pass through. Once the sensor placement is finalized, the supporting platforms can be further secured by hot-gluing the tips onto the origami body.

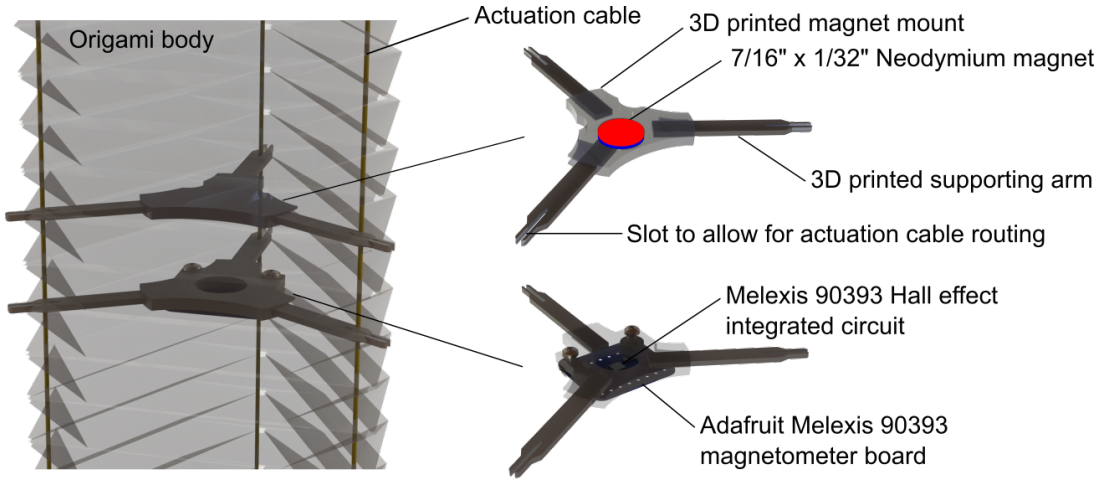

Figure 4.1: Sensor design and placement. The red and blue colors on the magnet signify the north and south magnetic poles respectively.

Optimal Placement of Magnet and Hall Effect IC

The optimal magnet and sensor placement is crucial for generating reliable sensor data since the magnetometer has an inherent limit on its sensitivity. The sensor would be quickly saturated if the magnet is placed too closely. In contrast, weak and noisy reading would be the case if the magnet is too far from the sensor. Thus, the parameters to be optimized include the air gap distance between the magnet and the sensor, and also the magnet dimension (diameter and height). The dimension of the magnet is directly correlated to the magnetic flux hence affecting the air gap distance.

We simulated readily available off-the-shelf cylindrical permanent magnets with various dimensions in COMSOL to qualitatively analyze the change in magnetic flux density with varying magnet dimension as shown in Figure 4.2. The magnet is simulated with the remanent flux density of 1.32 Tesla. The magnetic flux within the sensitive range of the magnetometer is shown and the value for B_y is omitted since the magnet is axially magnetized (B_x and B_y are symmetric about Z axis). The simulation shows that the magnetic flux increases proportionally as the magnet dimension grows. Larger diameter of magnet is preferable due to a more uniform magnetic field directly under the magnet at which the sensor will be located. This can mitigate the error due to magnet and sensor misalignment. Furthermore, thicker magnet is preferable as it allows for larger distance between the magnet and the sensor. Larger distance between the two will act as a lever that will amplify the change in tangential magnetic flux reading when the origami module bends. We settled with the $7/16" \times 2/32"$ cylindrical magnet by stacking two $7/16" \times 1/32"$ magnets. Furthermore, the magnet and the sensor are separated with a distance of 15 mm when the origami module is at its straight configuration and maximum length as shown in Figure 4.1.

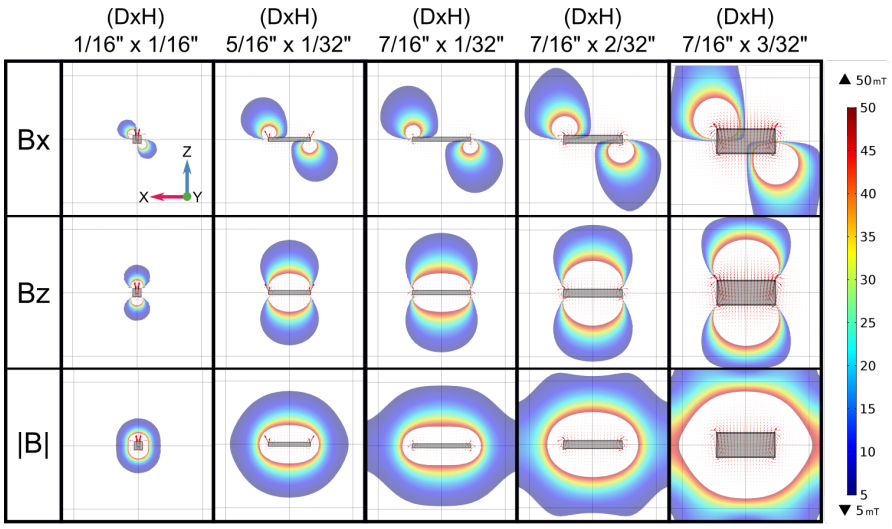

Figure 4.2: Visualization of magnetic flux distribution for different magnet size simulated in COMSOL finite element analysis software. Only magnetic flux within the sensor's sensitivity range (5-50 mTesla) is shown.

4.2.2 Data Collection

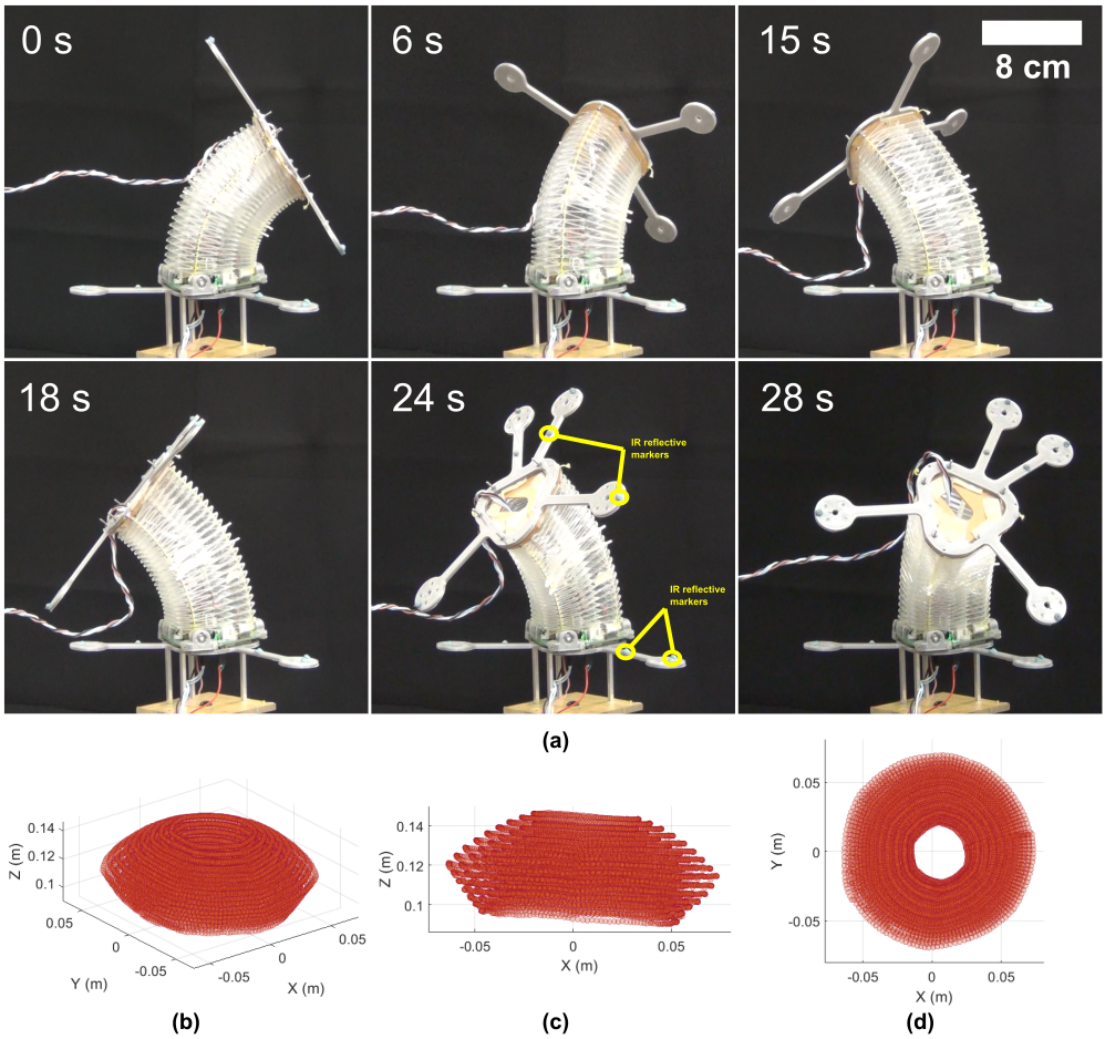

Figure 4.3: (a) Snapshot of origami module executing spiral motion for training data collection. Infra-red (IR) reflective markers are mounted on both ends of the module to measure the robot's shape parameters (s, θ, φ), while the encoder and magnetic data are internally measured by the module's controller board. Tracked tip position: (b) isometric view, (c) side view, and (d) top view.

The feature and label data are collected using the setup as shown in Figure 4.3. The feature data, which includes motor encoder ticks and magnetic reading, were internally measured by the robot's

controller board and the magnetometer respectively. The label data (s, θ, φ) was obtained using the OptiTrack motion tracking system. Infra-red (IR) reflective markers were mounted onto 3-D printed platforms at each end of the origami module. The encoder data is collected by the module's controller board while the magnetic reading is obtained by the Adafruit magnetometer and transfered through I2C communication protocol. A moving average filter was implemented to obtain smoother magnetic reading. The origami module was commanded to follow a spiral path by incrementally changing its arc length (s), bending angle (θ), and bending direction (φ). The tracked robot's tip position is shown in Figure 4.3(b-d). Spiral path allowed for faster training data collection, since the origami module is swept about φ so a small change happened at the time (smooth motion) except when changing the s and θ. The label data collected is within the ranges of [0.12, 0.15] m, $[\pi/9, \pi/4]$ rad, and $[0, 2\pi]$ rad for arc length, bending angle, and bending direction respectively. A time delay of 50 ms is used between each data point during the increment of φ, and a time delay of 5 s is used when the module changes its length significantly from 0.15 to 0.12 m. Data collection is completed in about 15 minutes.

4.2.3 Regression Model Training

Two well known machine learning methods for regression, K-nearest neighbor (KNN) search and multilayer perceptron (MLP), are investigated in this work. The K-nearest neighbor (Figure 4.4(a)) is one of the simplest classifiers among the machine learning algorithms hence can be easily implemented. The trade off between nearest neighbor search vs the multilayer perceptron is that the nearest neighbor search is limited by the amount of memory to search the lookup table if we want to eventually deploy the system. In other hand, MLP model (Figure 4.4(b)) will come in the form of an multi-input multi-output equation, but we may still need to store the model's graph structure of weights and bias values as well. The machine learning models were built using the MATLAB neural network toolbox functions, specifically `knnsearch` and `feedforwardnet`. Furthermore,

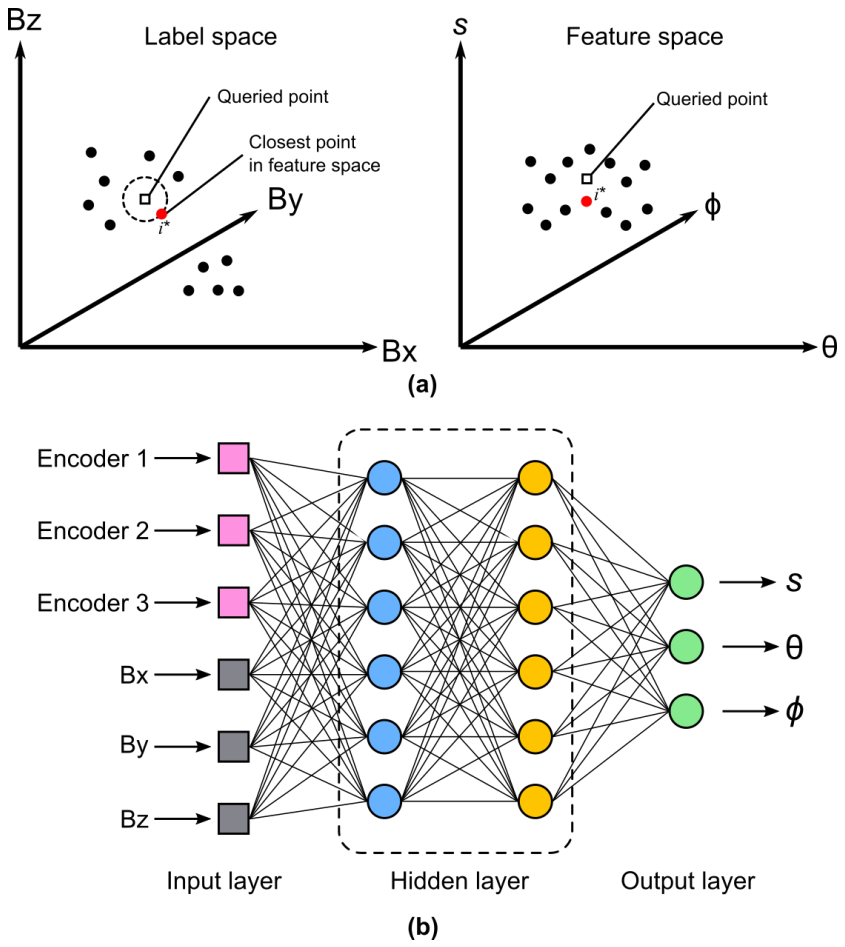

Figure 4.4: (a) K-nearest neighbor (KNN) search algorithm. (b) Multi-layer perceptron (MLP) also known as fully connected neural network.

we the trained machine learning models with different training data sets: encoder only data, magnet only data, and combination of the two. The hyper-parameters for the model are summarized in Table 4.1.

Mean squared error is used for the performance measure and radial basis function (`radbas`) is employed as the transfer function for each hidden layer. Model training is done in MATLAB with parallel computing in which 4 number of workers is used. The `trainbr` function is used for the training function due its effectiveness in creating a more regularized model. Regularization is es-

Table 4.1: Best model hyperparameters for the machine learning methods investigated in this work.

Model	Hyperparameters
KNN	Num of neighbors = 1 Distance = Euclidean
MLP (encoder only)	Hidden layers = 2 Neurons = [30, 15]
MLP (magnet only)	Hidden layers = 2 Neurons = [30, 30]
MLP (encoder and magnet)	Hidden layers = 3 Neurons = [36, 18, 9]

sential to prevent a model that overfits. This function employs a method called Bayesian regularization which tries to minimize both the square errors and the weights in order to create a network that generalizes well. Furthermore, Bayesian regularization allows for skipping of the lengthy cross-validation process[95].

4.2.4 Experimental Validation

We evaluated the performance of the machine learning models in predicting arc parameters of two origami modules under no load condition. We collected test data in similar fashion as for the training data with coarser increments on the desired arc parameters and still within the range of the training data. We also evaluated the performance of the models to predict the curvature of the origami module under external load. Furthermore, this experiment evaluates the ability of the models to predict arc parameters outside the range of the training data. 3-D printed curvature templates as shown in Figure 4.5 are used to facilitate repeatable applications of external load. The curvature of the templates ranges from [3.74, 11.22] m^{-1} and correspond with arc length of 0.14 m and increasing bending angle of $[\pi/6, \pi/2]$ radian. The origami module was initially commanded to reach arc length of 0.14 m, bending angle of $\pi/9$, and bending direction of 0 radian. The module is then pushed

against each curvature template until it passively conforms to the desired shape. The encoder values and magnetic reading were then collected after waiting for 10 seconds for each curvature template. Furthermore, the experiment was repeated three times for each curvature values.

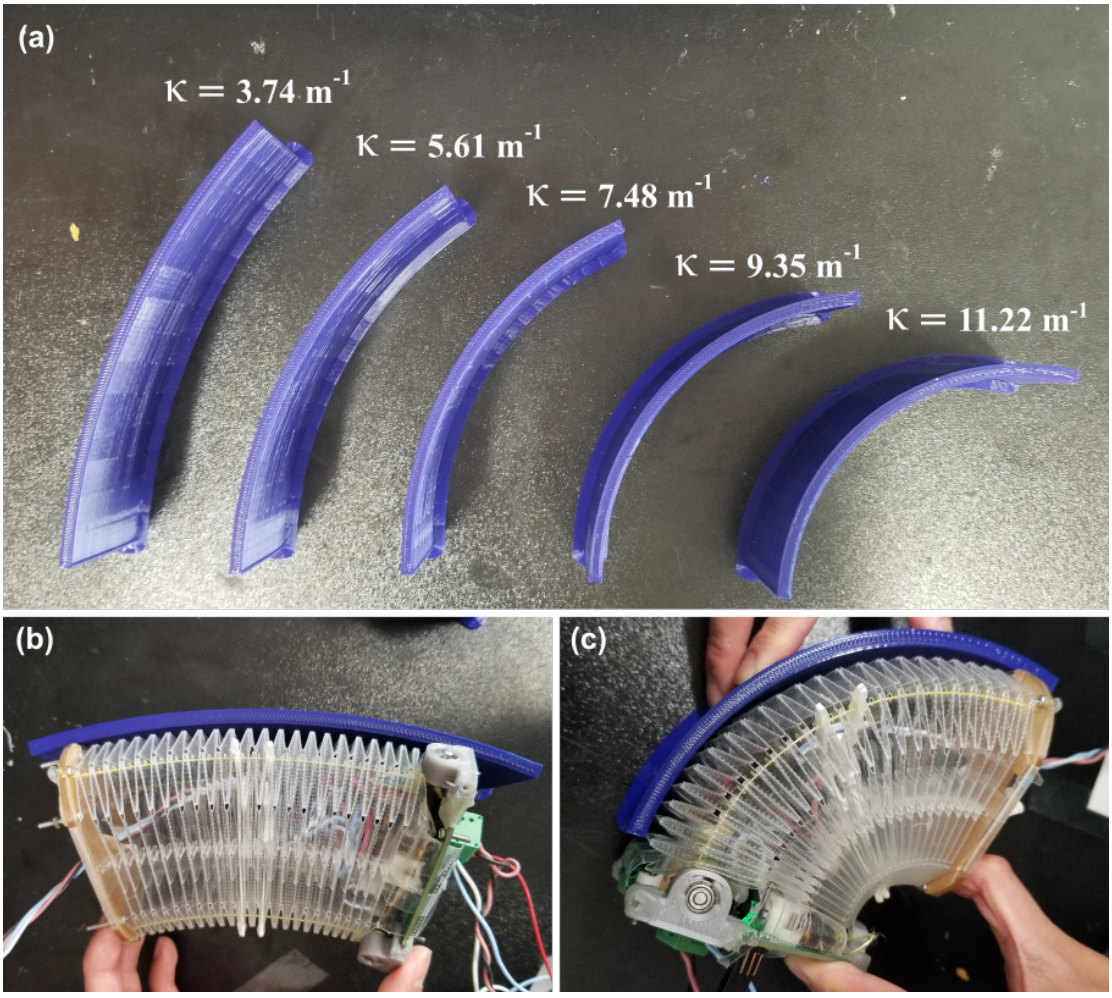

Figure 4.5: (a) 3-D printed curvature templates. Origami module pushed against the template with (b) the lowest curvature, (c) against the template with the highest curvature.

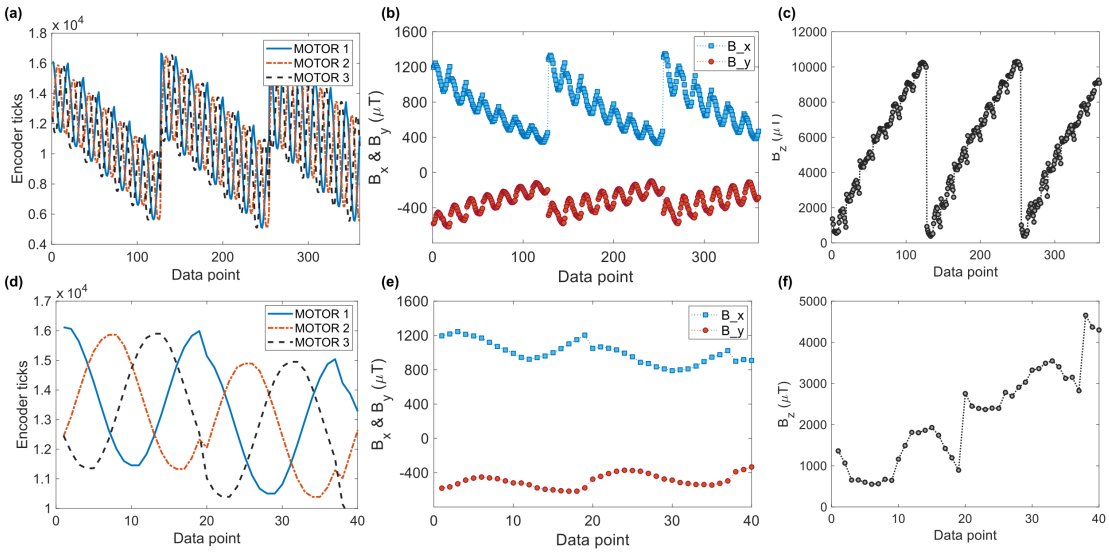

Figure 4.6: (a-c) Zoom-out view of the encoder and magnetic reading. (d-e) Zoom-in view of the data.

4.3 Results

Figure 4.6 shows the representatives of encoder and magnetic data collected for the model training. The top row (a-c) shows the zoomed-out view of the data and the bottom row (d-e) shows the zoomed-in view. Furthermore, we can plot the feature and label data in 3-D plot as shown in Figure 4.7. The plotted encoder data resembles a slanted cylindrical tower while the magnetic data has a tapered feature. The cone-like shape of the magnetic data is caused by the decrease in magnetic flux reading as the magnet and the sensor become farther apart. In our case B_z value becomes smaller (more negative), while B_x and B_y become more positive as the sensor and the magnet pair become closer. Figure 4.7(c,f) show the range of robot shape parameters used for the training.

Figure 4.8 shows an example of the prediction results for the robot's arc parameters under no external condition. The prediction shown in the figure was done using both machine learning methods and encoder data for the training dataset. Furthermore, the results for different datasets and origami modules are summarized in the barcharts shown in Figure 4.9. The barcharts show that the

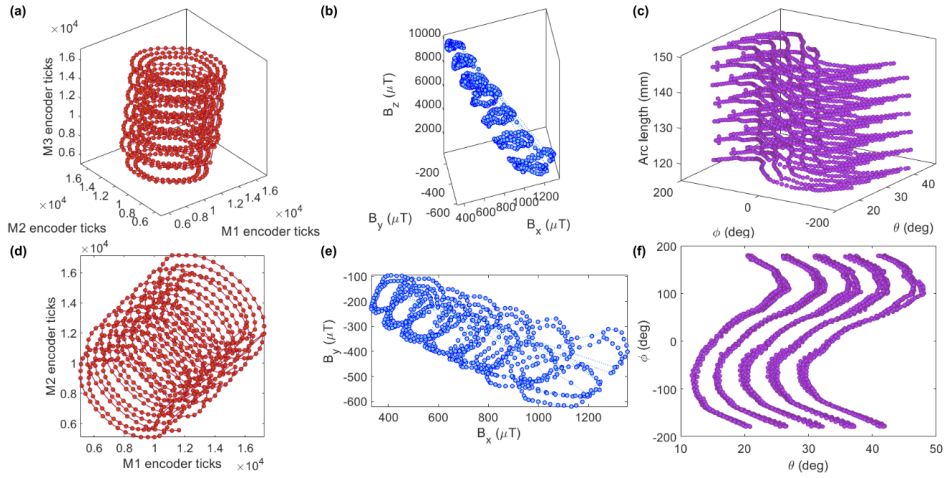

Figure 4.7: Isometric view of the feature space that includes (a) encoder and (b) magnetic data, and (c) label space. (d,e) Top view of the feature space, and (f) label space.

models are capable of predicting the arc length with maximum root-mean-squares (RMS) error of 15.48 mm. Similarly, the bending angle could be predicted with maximum error of 13.37 degrees. In contrast, the worst performance is shown when predicting the bending direction with maximum error of 110.2 degrees. The best and worst performances of the models are summarized in Table 4.2.

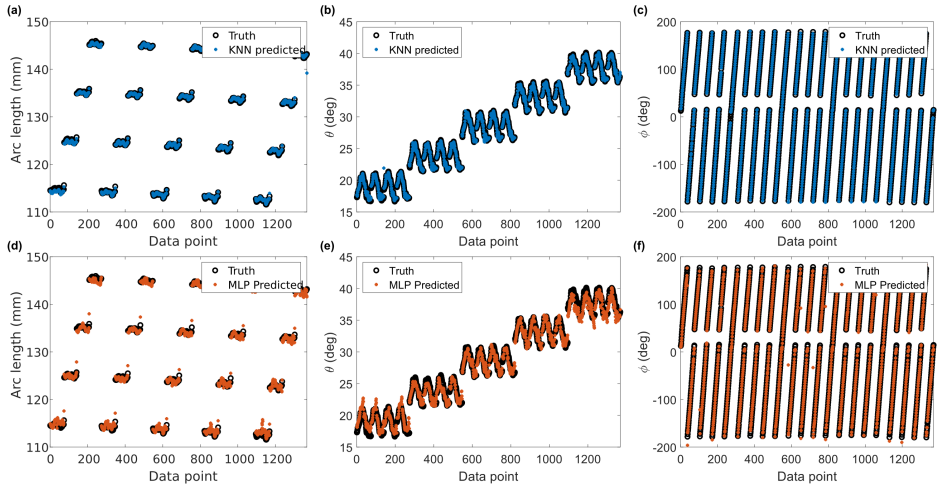

Figure 4.8: (a,d) Prediction results for arc length, (b,e) bending angle, and (c,f) bending direction for KNN and MLP models trained using encoder data only.

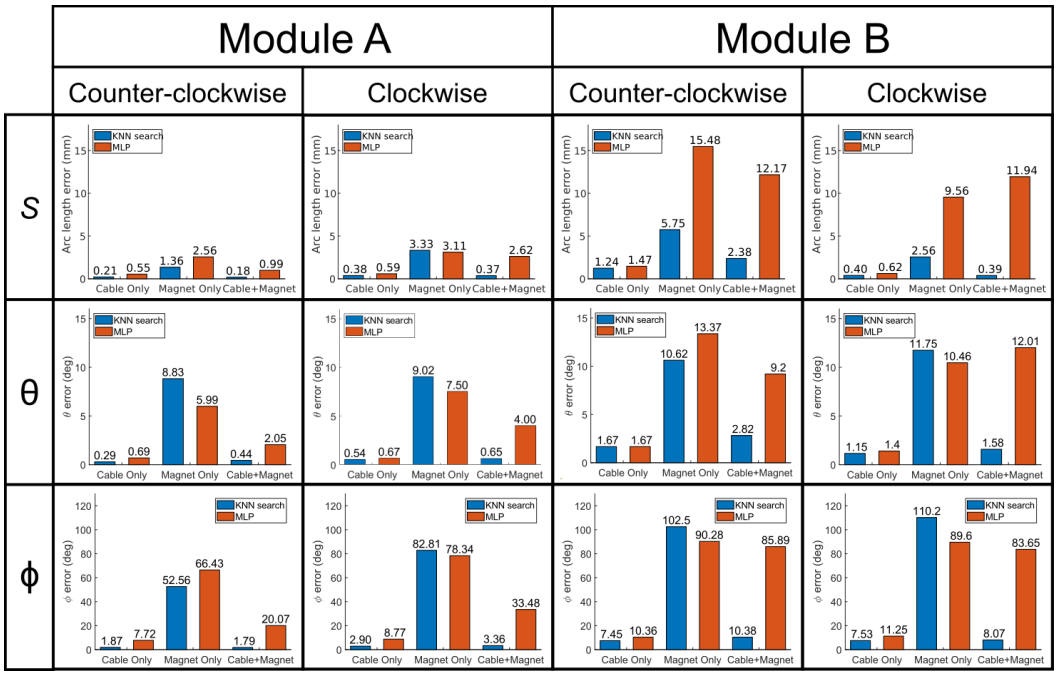

Figure 4.9: Summary of the prediction RMS error for different training datasets and origami modules.

Table 4.2: Summary of the best and worst performing predictive models for each arc parameter.

Arc parameters	Minimum error	Maximum error
s	KNN - CM = 0.18mm (0.12%)	MLP - M = 15.48mm (10.32%)
θ	KNN - C = 0.29° (0.73%)	MLP - M = 13.37° (33.43%)
φ	KNN - C = 1.87° (1.04%)	MLP - M = 110.2° (61.2%)

Figure 4.10 shows an increase in RMS error as the density of the feature data decreases, suggesting a decrease in prediction accuracy of the KNN search caused by a sparser training data set. The less dense dataset is obtained by selecting every 10^{th}, 20^{th}, 30^{th}, 40^{th}, 50^{th} data points from the densest dataset. The percent changes of RMS error between the most and least dense datasets are summarized in Table. 4.3. The results show that the KNN search utilizing magnetic data gets affected the least by the change in feature data density despite performing the worse in terms of

prediction accuracy. KNN search models with encoder only data and combined data show similar performance degradation with slightly higher value for the former.

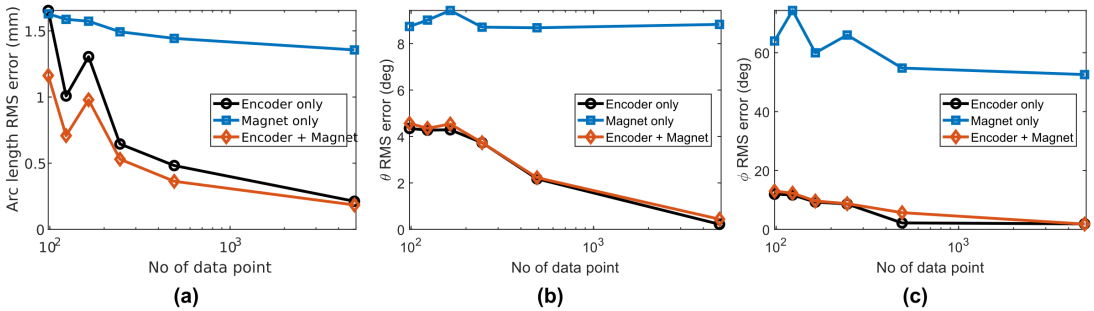

Figure 4.10: RMS error of (a) arc length prediction, (b) bending angle θ, and (c) bending direction φ, as a function of feature data density for KNN search.

Table 4.3: Percent change in RMS error of the predicted parameters for the most dense and sparsest data set.

Parameters	Percent change (%)		
	Encoder only	Magnet only	Encoder + magnet
s	87.2	16.8	84.2
θ	94.9	-1.0	90.4
φ	84.4	17.8	86.2

Figure 4.11 shows the prediction results for the external load scenarios using the known curvature templates. The RMS errors for the machine learning models and different data set as follows: encoder only (KNN, MLP) = (5.891, 5.855) m^{-1}, magnet only (KNN, MLP) = (4.337, 3.014) m^{-1}, encoder and magnet (KNN, MLP) = (5.524, 3.198) m^{-1}.

4.4 Discussion

Several insights can be gathered from the results: first, arc length is the robot's shape parameter that can be predicted most reliably followed by bending angle and bending direction respectively. Sec-

ond, it appears that the magnet data alone is less reliable due to the very small changes in B_x and B_y corresponding to very small changes in magnet position when the origami module changes its shape. This is shown by the worst performance of the models trained with magnet data only. In contrast, the models constructed only with encoder data perform the best across the different modules. Possible increases in the prediction error for even the best model is likely caused by small variability in origami modules' stiffness due to fabrication process. We can also observe a certain bias in the error with respect to the direction in which the module rotates (clockwise vs counter-clockwise), despite the bias being negligible.

Moreover, as shown in Figure 4.11 the models with encoder data only could not predict the

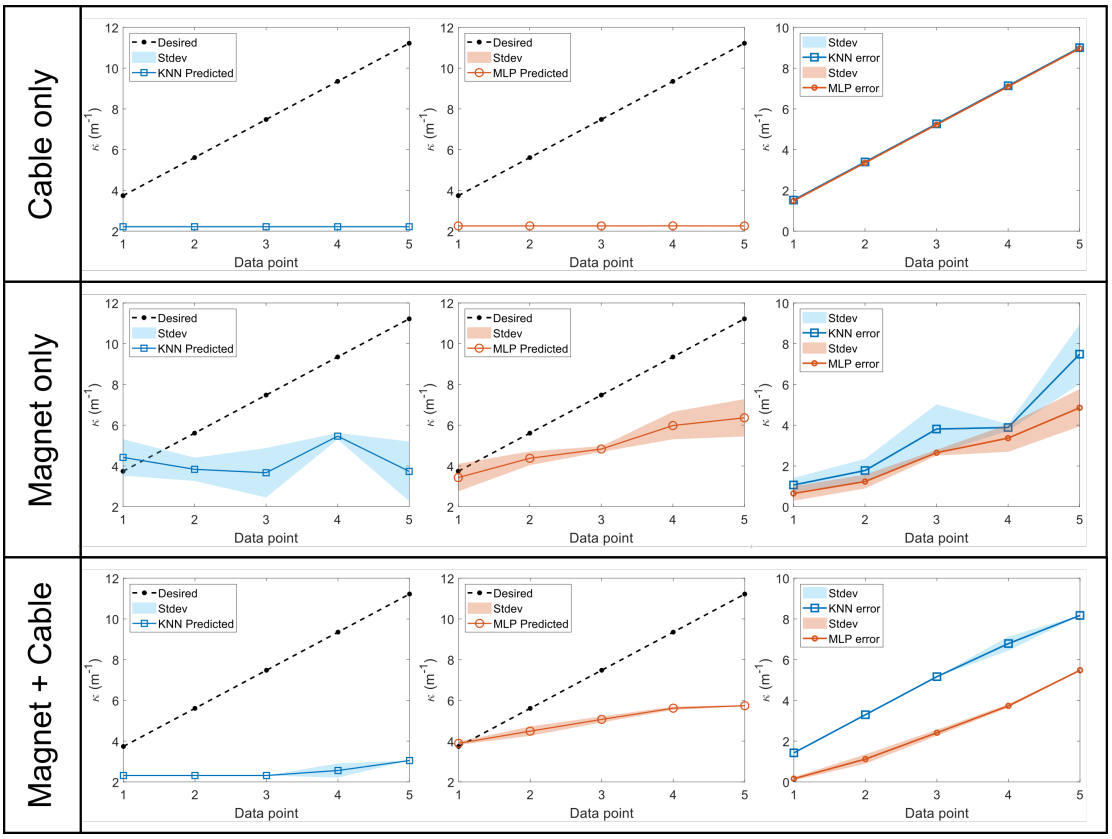

Figure 4.11: Prediction results for the origami module under external load.

changes in curvature when the origami module is exposed to an external load. The external load caused the compliant body to bend while also making the actuation cable untaut/slacked, thus this change was not being recorded by the encoders. The addition of magnetic data decreases the performance of the predictive model with encoder only data for the no external load scenario. In contrast, the MLP model with combined magnet and encoder data performs the best for the experiment with external load. Moreover, the addition of magnetic data to the MLP model for the external load scenario reduces the standard deviation of the curvature prediction.

In summary, one should utilize KNN model trained with only encoder data for no external load scenarios while MLP model with combined magnet and encoder should be used when external load is expected. As shown in the earlier section, the magnetic reading in normal direction with respect to the magnetometer IC (B_z) shows the largest sensitivity against the change in robot shape, thus in the future improvement can be made by utilizing 3 magnetometer ICs placed at the three corners where the actuation cables are instead of only using a single magnetometer IC in the middle. This will allow for richer measurement as now the change in magnetic field value read by each sensor is analogous to the change in the actuation cable length but without the previously discussed drawback caused by untaut cables. However, this will increase the overall complexity of the sensor as more magnetometer IC and magnet pairs are required. Additionally, a custom made printed circuit board would be necessary. Furthermore, since the shape estimation obtained through encoder data appears to be the most accurate one, it would be interesting to explore the possibility of developing a routine in which the origami module would get out of the slack cable condition by slowly decreasing the cable length until tension is recovered/detected. However, this will require some sort of force sensor attached to the actuation cable. The routine could be triggered by the change in magnetic field when at the same no change in cable length is measured.

4.5 Conclusion and Future Work

This chapter introduces the development of a sensing methodology to estimate the shape of an origami continuum robot. The arc parameters corresponding to the robot shape can be accurately predicted with maximum RMS error of 0.98 %, 4.17 %, and 4.36 % for the arc length, bending angle, and bending direction respectively. These results are obtained using the best performance model trained with encoder only data. Furthermore, KNN model consistently performs much better compared to the MLP model for no-external load scenario while MLP generalizes much better when external load is present (42 % decrease in RMS error).

However, it is important to note that KNN model's performance is heavily dependent on the density of the feature data used for the search process as previously discussed. The use of denser feature data will allow for a more accurate prediction but with a trade off in longer solving time as the algorithm needs to calculate distance metric for more data points. Furthermore, if the eventual goal is to deploy the model into an embedded system for a more portable robotics platform, then the hardware memory size constraint should be taken into account.

Potential future work is to improve the performance of the magnetic reading to further reduce the estimation error, especially on the prediction of φ. The poor performance is likely due to the non-linearity in magnetic flux of a permanent magnet thus resulting in the less sensitive tangential magnetic readings (Bx and By). It would be beneficial to make the magnetic reading to be in the same magnitude in all the axes (Bx, By, Bz) as the case for the encoder data. In the current implementation, the B_z reading is about 8-25 times larger than the B_x and B_y reading. However, it would be challenging to achieve similar magnitude of magnetic measurement in normal and tangential direction since for axially magnetized magnets the magnetic flux along the magnetization axis would generally be much stronger than the tangential components. Thus, one possible way to overcome this is to introduce more magnetometer and magnet pairs that only measure magnetic flux in nor-

mal direction.

Shape estimation to predict non-constant curvature caused by multiple external forces could also be explored. This most likely will require additional sensors. One possible way to address this is to use denser magnet sensor pairs (at least two pairs) along the length of the module. This will allow for measurement of multiple slivers of the origami module. Additionally, this scenario could be re-formulated as prediction of external forces applied to the module. A more elaborate setup is necessary to provide controllable applications of external forces. Other non-static learning models such as Recurrent Neural Network (RNN) and Long Short-Term Memory (LSTM) could also be investigated. Instead of using static data, one could train a model with temporal data of the encoder and magnetometer.

Lastly, to mitigate the effect of magnetic interference typically present in magnetic based sensing one could possibly employ an electromagnet instead of permanent magnet to be paired with the magnetometer. This arrangement will allow for the desired magnetic field to be turned on and off, followed by measurement of the magnetic interference from surroundings. A more straightforward solution would be to do shielding using high permeability materials (mumetal, 60 % nickel alloy) however the shield can still get saturated, although unlikely to happen in real life scenarios.

5

Other Applications of Origami Continuum Module

This chapter highlights the potential of the origami modules to be used for robotics research platform. The two applications discussed are the 3-D origami snake robot and the experimental study on a transferable object classification by continuum wraps. We envision that the snake robot could traverse the rubble in the search-and-rescue scenario and the touch based object classification might be beneficial in a smoke-filled area (due to fire) where a vision system would not work reliably.

5.1 Origami Snake

Snake robots offer a useful and unique mobility platform for search-and-rescue applications. However, existing prototypes made of rigid links and joints have restricted flexibility, hampering their usefulness in highly cluttered, maze-like environments. Moreover, their heavy weight limits their energy-efficiency and performance in three-dimensional (3-D) tasks. To address these challenges, the work described in this chapter presents a new approach using cylindrical, origami continuum modules driven by internal cables and electric motors, as well as a local feedback control system on each module. Thus, we can distribute actuation, sensing, and control for highly scalable soft robotic continuum origami systems. Using this approach, we develop a 3-D origami robotic snake which is able to locomote using lateral undulation and sidewinding gaits similar to those used by biological snakes. The proposed snake robot is a continuously deformable, light-weight, modular, and low cost robotic system made of a folded thin plastic body. We detail the design, fabrication, and control of this 3-D origami robotic snake prototype, focusing on the analysis of locomotion parameters for each gait. We experimentally search for the optimal parameters for both types of locomotion, with maximum speeds characterized as 40.5 mm/s (0.1 body-lengths per second) for lateral undulation and 35 mm/s (0.09 body-lengths per second) for sidewinding locomotion.

A range of snake robots have been developed using traditional robotic kinematics comprising rigid links and discrete joints. Wright et al. developed a modular snake robot made of servo motors

---

The material presented in this chapter is adopted from the following self-authored publications:
M. Luo, R. Yan, Z. Wan, Y. Qin, **J. Santoso**, E. H. Skorina, C. D. Onal, Orisnake: Design, fabrication, and experimental analysis of a 3-d origami snake robot. IEEE Robotics and Automation Letters 3, 1993–1999 (2018).[96]
H. Mao, **J. Santoso**, C. Onal, J. Xiao, in International Symposium on Experimental Robotics (ISER) 2018 (2018).[97]

mounted in series, capable of climbing up the inside of a pipe[98]. Crespi et al. developed a larger, more complex snake robot with DC motors and detachable wheels capable of locomotion on land and in water[99]. Snake robots can use different methods of locomotion, including most frequently serpentine locomotion (or lateral undulation) and sidewinding locomotion [100,101,102,103].

Rigid robotic snakes, though capable of snake-like motion [104,105], suffer from a number of problems. Since rigid snakes only possess discrete joints, they can only emulate the smooth continuum body motions of biological snakes by moving many small links simultaneously. This may reduce the effectiveness of their locomotion, increase energy consumption and control complexity, and make it difficult to access unpredictable and highly-constrained environments.

To address this problem, prior work focused on developing soft pressure-operated robotic snakes [106,107]. These soft robotic snakes use pneumatic pressure to actuate silicone rubber segments that make up the body of the snake, resulting in a constant-curvature deformation along the length of each segment. This results in a flexible, safe, and realistic motion, effectively mimicking the gait of a biological snake. Unfortunately, soft pneumatic actuators also have disadvantages. They can be inefficient, constantly venting their motive pressure to the environment. In addition, the compressors required to generate the input pressure used in pneumatic actuators tend to be heavy and bulky, reducing the effectiveness of this type of actuation for autonomous mobile robotic applications.

In this chapter, we introduce a self-contained, light-weight, low cost and flexible origami robotic snake (OriSnake). OriSnake is constructed of origami modules that resemble bellows and actuated via cables connected to electric motors. Thus, we combine the flexibility of soft robotics and the portability and efficiency of traditional electrical actuation.

5.1.1 Experimental

The OriSnake shown in Figure 5.1 consists of 4 origami modules connected in series and a master controller board located at its head. The passive wheels provide anisotropic friction allowing the

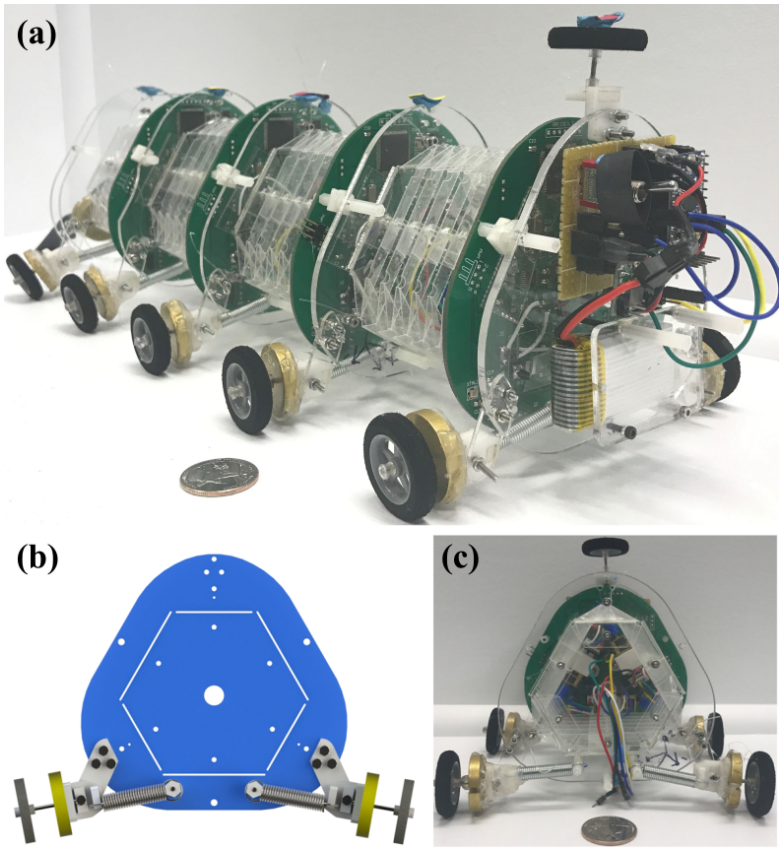

Figure 5.1: (a) The origami snake (OriSnake) robot constructed using 4 origami modules connected in series. Front view of the snake robot (b) in rendered in CAD software and (c) actual.

robot to produce motion in a particular direction (along the body length). A simple but effective suspension system was incorporated into the robot design to allow for constant contact between the wheels and the surface while traversing (Figure 5.1(b-c)).

Two typical snake gaits are investigated: lateral undulation (serpentine) and sidewinding. The lateral undulation gait achieves motion through generation of traveling wave while the sidewinding gait requires the body of the robot to be lifted off the ground. The undulation gait can be described with the function below,

$$\kappa_i(t) = \frac{\beta}{s} \sin(\gamma t + i\alpha) \tag{5.1}$$

where $\kappa_i(t)$ denotes the instantaneous curvature of i^{th} module, β is the maximum bending angle, γ is the bending rate, s is the module's arc length, and α is the offset angle. Similarly, the sidewinding gait can be formulated as,

$$\begin{aligned} \kappa_i(t) &= \frac{\beta}{s} = constant \\ \theta_i(t) &= \omega t + \alpha i \end{aligned} \tag{5.2}$$

where $\varphi_i(t)$ is the instantaneous bending direction of i^{th} module, and ω is the angular velocity of the bending plane orientation. For the sidewinding gait we define the offset angle α to be $\pi/2$.

5.1.2 Results

Figure 5.2(a-d) shows the results for the optimal parameter search of the serpentine gait while the snapshot of the robot motion is shown in Figure 5.2(e). The optimal parameters found are 45 degrees for the maximum bending angle (β) and 50 degrees for the offset angle (α). Furthermore, the robot is capable of traveling with 40.5 mm/s (0.1 body-lengths per second).

Similarly, Figure 5.3 shows the results for the sidewinding gait. The fastest traveling speed of 35 mm/s (0.09 body-lengths per second) is obtained with 45 degree bending angle and angular velocity of 276 degree/s. Although the sidewinding gait produces a slightly slower traveling speed, it will be more robust against uneven terrain compared to the serpentine gait as the robot's body is lifted above the ground with this particular gait.

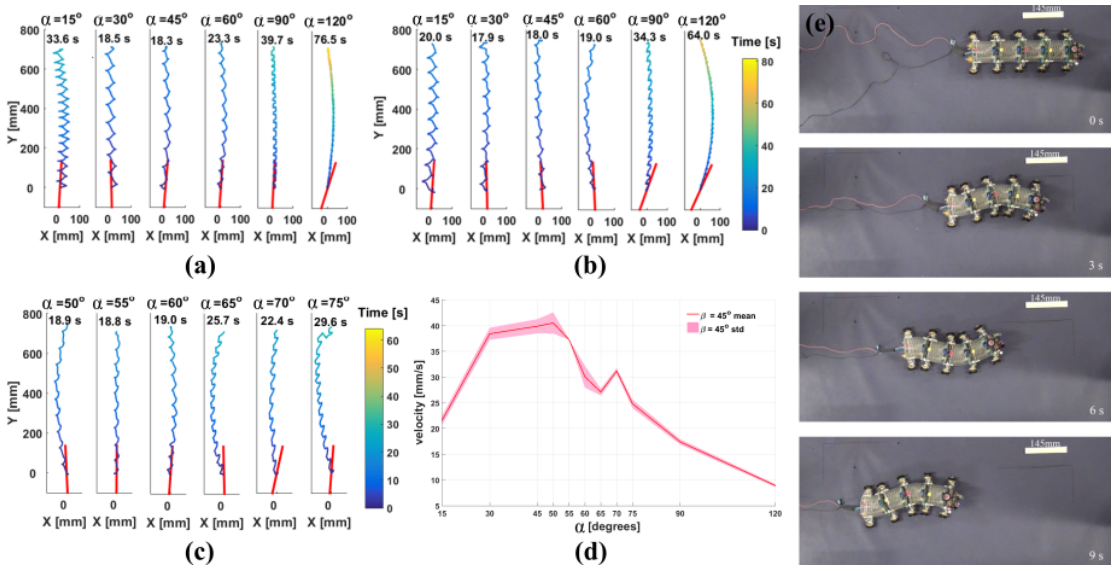

Figure 5.2: Optimal parameter search by varying the value of offset angle α for two bending angles (a) 60 degrees and (b) 45 degrees. Shown are the Center of Mass (CoM) trajectory of the snake robot during serpentine locomotion. Trajectories are rotated for more concise plotting, with the initial position of the snake shown with red lines. The color bar on the right shows the time of each data point, with the final time shown for each trajectory. (c) Further search with a finer increment in α. (d) The mean and standard deviation of the velocity of the center of mass of the OriSnake with β = 45 degrees for varying offset angles α on the horizontal axis. The results were calculated using 3 separate experiments. (e) Top view snapshots of lateral undulation gait over 9 seconds.

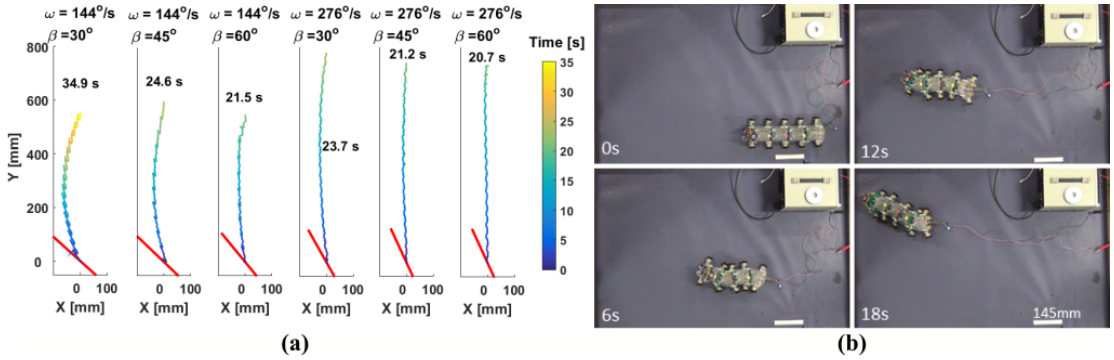

Figure 5.3: (a) The Center of Mass (CoM) trajectory of the snake robot during sidewinding locomotion with various bending angle magnitude (β) and angular velocity (ω). Trajectories are rotated to improve the visualization, with the initial pose of the snake shown as a red line. The color bar on the right shows the time of the data point, with the final time shown for each trajectory. (b) Top view snapshots of sidewinding gait over 18 seconds.

5.1.3 Conclusion and Future Work

This section introduces the WPI Origami Robotic Snake (WPI OriSnake) that is capable of executing both lateral undulation (serpentine) and sidewinding locomotion modes. This robot is a low-cost, light-weight, modular system, where each module has its own slave controller, distributed sensing, and actuation. It was found that a maximum velocity of 40 mm/s (0.1 body-lengths per second) and a maximum velocity of 35 mm/s (0.09 body-lengths per second) could be achieved during serpentine and sidewinding locomotion respectively.

The OriSnake used an external power supply to drive the motors. This was mainly done for the sake of simplicity to control the maximum current during testing. The use of on-board batteries is unlikely to negatively impact the performance of the snake. In fact, during initial testing, we found that the snake body was too light. This is partially caused by the high torsional stiffness of the origami modules. When a module has a slight rotation around its axis or at its end-plates due to imperfections in fabrication, the torsional stiffness of the module would be too high for the next module to fully make contact with the ground. This was particularly a factor in serpentine locomotion, and the additional weight of on-board batteries might improve the robot's performance.

For future work, the mechanical design of this snake robot can be optimized. The velocity of the current snake robot is slow compared to other snake robots. One cause of this is that the current gear motors we used are able to generate large torques, but at a much slower speed. Additional work can be done to choose a motor that has the speed and torque capabilities to make the OriSnake faster while still having a small enough profile to fit inside the modules. This can be combined with a replacement for the passive wheels to bring the OriSnake closer to studies in real world search-and-rescue.

The unique combination of the low-cost and light-weight origami-inspired design and manufacturing with soft robotic locomotion offers advantages in applications that require robots to

go through tight passages and navigate cluttered environments autonomously without tethers. Since the OriSnake can lift its modules off the ground, operation in 3-D environments is achievable. Further investigation on these conditions and the efficacy of the two gaits on rough terrain is planned for future study. For example, the serpentine gait can go faster in some environments but the sidewinding gait is likely to be more versatile. Future work will also include motion planning and decision making algorithms, which will need to take these and other complex factors into account.

5.2 Learning Touch Manipulation

In order to broaden the real-world application of robotics, the importance of advancing the capability of robotic manipulation is unquestionable. Most of the existing research in robotic manipulation assumes that the target object is known or visible, or can be made visible by adding a light source. However, in many real-world scenarios, such as underwater or in a smoke-filled room (in a building on fire), a target object may not be made visible. Therefore, it is necessary to investigate robotic manipulation based on other sensing modalities.

Tactile or force sensing can be very useful in providing more information about surrounding objects. Indeed, there is recent research on using tactile sensing for object recognition [108], exploration and manipulation [109,110,111], and shape estimation [112,113]. Touch sensors are usually mounted on the finger tips of the grippers, which are used to touch a target object to collect contact points. Object recognition is achieved solely based on the collected contact points [108] or in combination with visual perception [114]. Such touch-based perception is especially useful for perceiving transparent objects, which can be missed by visual sensing.

Continuum manipulators are more flexible for manipulating objects of a wide range of shapes and sizes in cluttered environments due to their compliant and soft nature. In particular, a contin-

uum manipulator can get into a small hole to fetch an object that a conventional, articulated manipulator cannot[115]. Since it is often dark in such a hole and difficult to bring in an extra light source, touch-based continuum manipulation is most desirable. If the target object is not visible, then object perception (i.e., classification and/or recognition) is also needed from touch-based continuum manipulation.

In a recent work[116], the authors introduced a shape-based approach for object classification and recognition through continuum manipulation. The main idea is to use the continuum robot as a tool to indirectly "measure" the object shape. That is, the shape of a continuum arm during whole-arm wraps of a target object, which can be transparent (and thus not visible), is used to indirectly characterize the shape of the object and this information is used for classification and recognition. For an object of any shape, a continuum wrap is generated automatically by a touch-based approach. However, the work is tested only in simulation with the assumption that the continuum arm is covered by tactile sensors. In reality, existing continuum manipulators are often not equipped with tactile sensors. One difficulty is that the body of the robot is deformable. A kinematics-based contact detection and localization approach for continuum robots is presented by Bajo et al. for which an external tracking system is required[117], but this may not always be available in real-world scenarios.

In this work, we study touch-based identification of object categories using a new form of continuum manipulator consisting of origami-based modules[43] and tactile sensors attached at each section. Using these new manipulators with sparse tactile sensing, we aim to achieve touch-based wrapping of objects and experimentally validate the following conjecture: the shape-based classifier introduced by Mao et al. and trained in simulation can be readily transferred to classifying real objects with real touch-based continuum manipulation[116]. We envision the robot to be used in a search-and-rescue scenario where it could be exposed to low-light environment hence could benefit from the touch-based manipulation.

5.2.1 Technical Approach

We next explain the manipulators and sensors used for this study, the touch-based motion planning strategy for generating continuum wraps, and the classification method of unknown objects.

5.2.2 Manipulators and Sensors

The continuum manipulators used for this study consist of multiple origami continuum modules connected in series. Each continuum module contains a foldable origami body, three brushed DC micro-motors, and a controller board that offers on-board sensory measurements, feedback control, and module-to-module communication. The foldable body is made out of Polyethylene Terephthalate (PET) sheets and constructed based on the Yoshimura crease pattern. This unique tubular structure with a diameter of 7 cm is capable of bending in two directions and extending/retracting, while maintaining its structure and resisting torsion. The foldable structure is connected to an acrylic plate on the top and to the PCB on the bottom where the motors are secured. Three nylon cables secured to the motor shafts and spanning the length of the structure along the edges are used to drive the segment. Each motor is equipped with a magnetic encoder for position control.

We built two continuum manipulators for this study. Figure 5.4(a) shows the 3-section manipulator used in the experiments with planar wraps, and each section has an active white module with motors on it and a passive green foldable body to expand the robot workspace. Improved from the 3-section manipulator, Figure 5.4(b) shows the 4-section manipulator used for generating spatial wraps benefiting to its more compact and light-weight modules and larger touch sensor contact areas.

Each section is characterized using three parameters (s, κ, φ), where s is the section length, κ is the curvature, and φ is the orientation angle[43,115]. Using the inverse kinematics of a continuum section discussed in my earlier work[43], we can then find the required cable lengths (l_1, l_2, l_3), that will shape

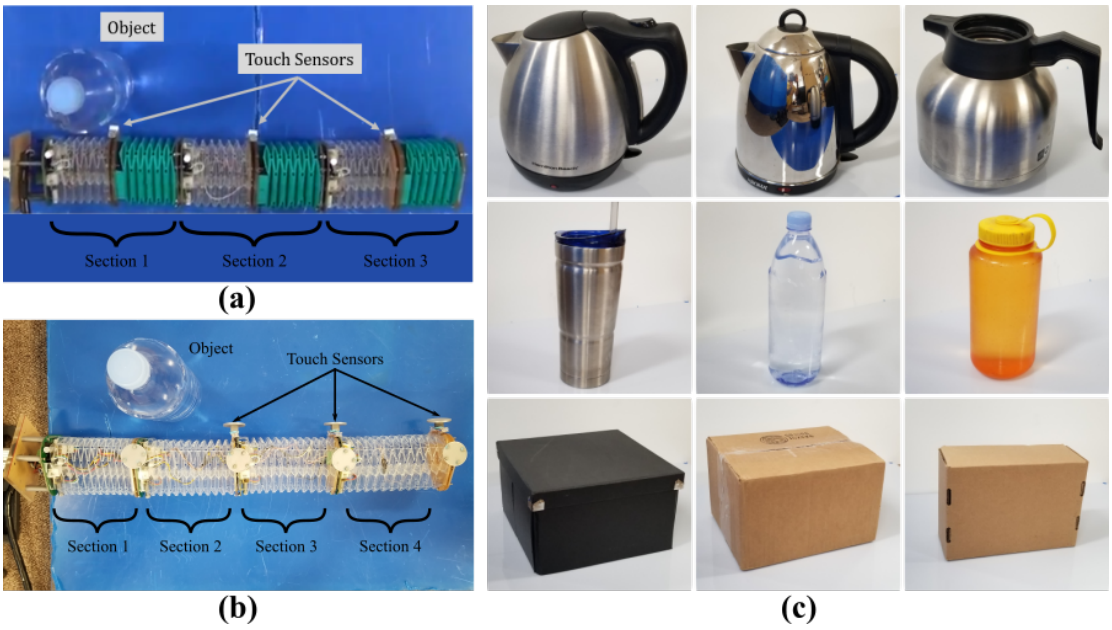

Figure 5.4: An object (a transparent water bottle) was placed near the base of arms for manipulation: (a) a touch sensor was mounted in the middle of each origami module in a 3-section arm, (b) a touch sensor was mounted at the distal end of each module in a 4-section arm. The diameter of the continuum section is 7 cm. (c) A list of objects used in the experiments.

the module into the desired configuration $(s_d, \theta_d, \varphi_d)$. The cable lengths are converted into encoder positions, which are then sent to the low-level controller as reference signals.

We constructed the touch sensors acting as bumper switches using two copper sheets adhered onto a parallel plate structure made out of the same material used for the origami collapsible body. One copper sheet is connected to the control board's digital I/O pin while the other is connected to ground reference. When the copper sheets touch each other due to depression of the structure, an electrical circuit is completed hence signaling a touch on the continuum section. For each continuum section we place the touch sensor at the end of each module and sandwiched between consecutive modules as shown in Figure 5.4.

5.2.3 Touch-based Continuum Wrapping

A general touch-based motion planning strategy is introduced by Mao et al. for a continuum manipulator to progressively generate wraps around an object under the guidance of the contacts made along the way without knowing the object model [116] . Starting from the initial configuration, the robot motion alternates between the *enclosing motion step* to make contacts with the object, and the *advancing motion step* to move forward towards wrapping around the object, until a wrap is formed or no further motion is feasible due to the physical limits of the manipulator. Such continuum wraps can be efficiently generated within hundreds of milliseconds (time of planning and collision checking combined) in simulation [116].

To achieve an *advancing motion step*, contact localization and estimation of the tangential and normal directions of the local contact patches are required [116]. We relaxed this requirement through extrapolating the robot section endpoints based on their local frames. Therefore, our planner only needs to know whether each manipulator section is in contact or not to plan the next move, which makes it more effective to guide the manipulator hardware to achieve touch-based continuum wraps.

5.2.4 Classification of Unknown Objects

As introduced earlier, this study aims to experimentally validate a shape-based classifier using continuum wraps [116]. The shape of the continuum robot wrapping around an object is described by a chord histogram descriptor, which approximates the robot shape using many 3-D chords and statistically captures its shape based on the chord parameters. We first trained a linear Support Vector Machine (SVM) classifier in simulation using wraps generated around the simulated objects and then applied the trained model to classify the real-world objects using real-world wraps. The objects in simulation were scaled to roughly match the dimensions of the real-world objects.

5.2.5 Experimental Results with Planar Wraps

In our experiments with planar wraps, we used the 3-section manipulator as shown in Figure 5.4(a). The robot manipulator is initially set at a straight-line configuration with full contraction, and the testing object is placed near the arm base. The minimum and maximum limits of the arc parameters for each section are as follow,

$$s \in [0.085, 0.145](\text{m}), \kappa \in [-10.69, 10.69]\text{m}^{-1}, \text{and } \varphi \in [-\pi, \pi].$$

A linear SVM classifier is trained in simulation using wraps from 10 water bottles, 10 boxes, and 6 teapots. For each object one wrap was generated. Figure 5.5 shows a few planar continuum wraps around the objects in simulation. We next conducted classification of three different real-world objects: a teapot, a water bottle, and a card box, through real-world continuum wraps.

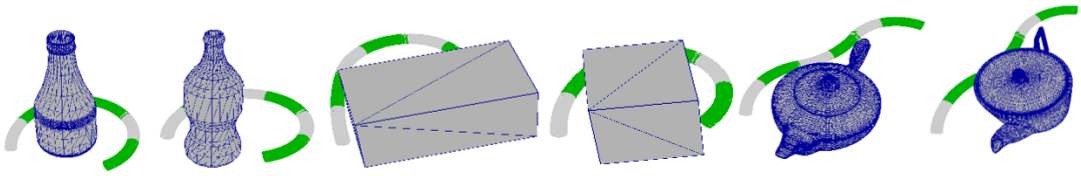

Figure 5.5: A few examples of the planar continuum wraps generated on different objects in simulation. The simulated arm has 3 sections and each section is colored in white for the first half and in green for the second half.

Figure 5.6 shows a few motion snapshots of the robot wrapping the real-world objects. Note that the goal of the continuum wraps is to encode the shape of an unknown object into the shape of the manipulator, as opposed to achieving tight grasps of objects with known models [115]. Therefore, the wraps do not need to be enclosing.

The final robot configurations commanded by the planner were used for classification. Table 5.1 summarizes object and wrap information and the classification results. Note that the classifier which learned solely from simulation is already effective in classifying the real-world objects, as the

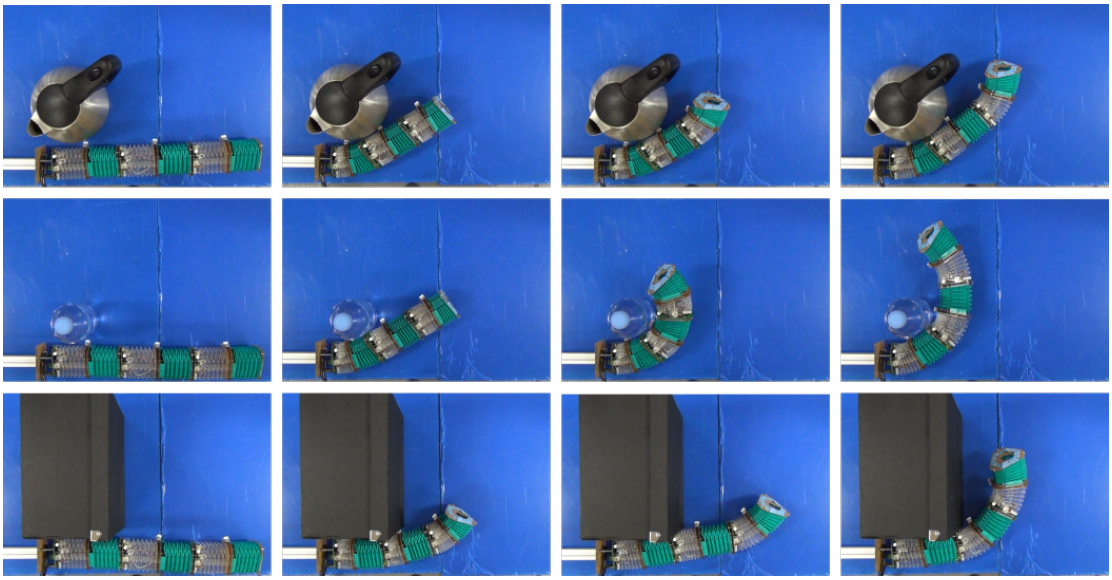

Figure 5.6: The motion snapshots of the continuum wraps generated on the real objects. The rightmost sub-figure in each row shows the final wrapping configuration.

probabilities of correct classification are more than two times higher than that of a random guess (about 0.33). However, the box was misclassified to be a bottle because the contact on section 1, which was closest to the base, was missed by the sensor, and therefore the planner kept commanding section 1 to bend more while it was actually stopped by the contact. Since the curvature of section 1 is a distinctive feature for classification, as shown in Figure 5.6, the classifier with the inaccurate data of a larger curvature resulted in the misclassification.

Table 5.1: Object dimension, number of intermediate configurations to generate the wraps, SVM prediction and its probability using 1 planar wrap for each object.

Object	dimension(cm)	# of configurations	SVM Prediction	Probability
bottle	$8 \times 8 \times 24$	59	bottle	0.81
box	$27 \times 16 \times 26$	61	bottle	0.83
teapot	$24 \times 18 \times 21$	42	teapot	0.71

5.2.6 Experimental Results with Spatial Wraps

We use the 4-section robot arm (Figure 5.4(b)) to conduct spatial continuum wraps around the objects to collect spatial shape information. The arm sections of this robot are more compact (rather than having two modules connected as one robot section) and light-weight, which makes it more suitable for spatial wraps. It also overcame the problems of missed contacts with increased contact areas of the touch sensors. Different wraps covering different areas on the objects were conducted to collect object spatial shape information. The 3-D chords generated from different wraps are accumulated into one histogram as an overall representation of the object shape. We next explain how the robot arm is lifted to conduct spatial wraps and present the object classification results.

5.2.7 Robot Arm Lifting

The arm is lifted by keeping the first module of the robot at a certain configuration during the experiment and then changed when switching to other wrapping planes (see Figure 5.8(b) for examples). The benefit of having this additional module is that the other modules (section 2, 3 and 4) can be fully used for generating the wraps, and they only need to undergo less strain and stress when wrapping around the objects. Alternatively, the modules could be mounted vertically to minimize the effect of gravity. However, this configuration is not always possible in a real life scenario, hence we decided to proceed with the former.

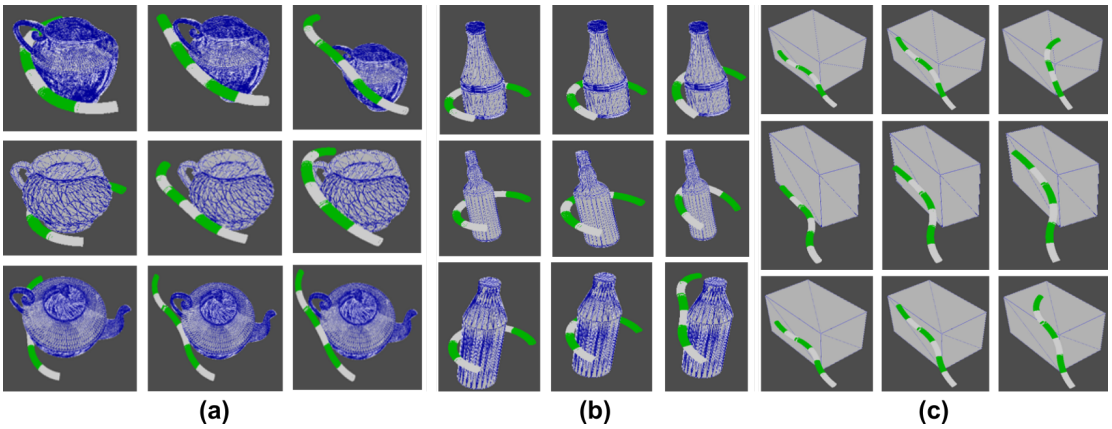

Figure 5.7: The spatial wraps in simulation for different object types: (a) teapots, (b) bottles, and (c) boxes. Each row in each subfigure is the three wraps around the same object. The simulated arm has 3 sections and each section is colored in white for the first half and in green for the second half.

5.2.8 Classification Results

We trained a linear SVM classifier using the same set of training objects used earlier, and the shape of each object was captured using 3 wraps. Figure 5.7 shows the wraps around the training objects generated in simulation. Figure 5.8 shows examples of such planar and spatial wraps around the real world objects. For testing dataset, we considered 3 object categories and 3 objects from each category (Figure 5.4(c)).

Figure 5.8 shows the motion process of the continuum wraps. As mentioned earlier, such wraps are the result of local motion generation, and they are only used to encode the object shape onto the robot arm shape. Therefore, some (for instance the wraps around the boxes) may only locally conform to the object shape and achieve partial wrapping of the object.

We noticed that the robot final wrapping configurations deviate from the robot motion commands sent by the motion planner (major cause for the misclassification of the box in planar case. There are two main reasons. First, our robot arms currently do not have the proprioceptive sensors to achieve precise closed-loop control. Second, some contacts may be missed by the current sparse

touch sensing on our robot arms. Therefore, in order to more precisely identify the final robot shape, we used an external vision tracking system to identify the robot final configuration when

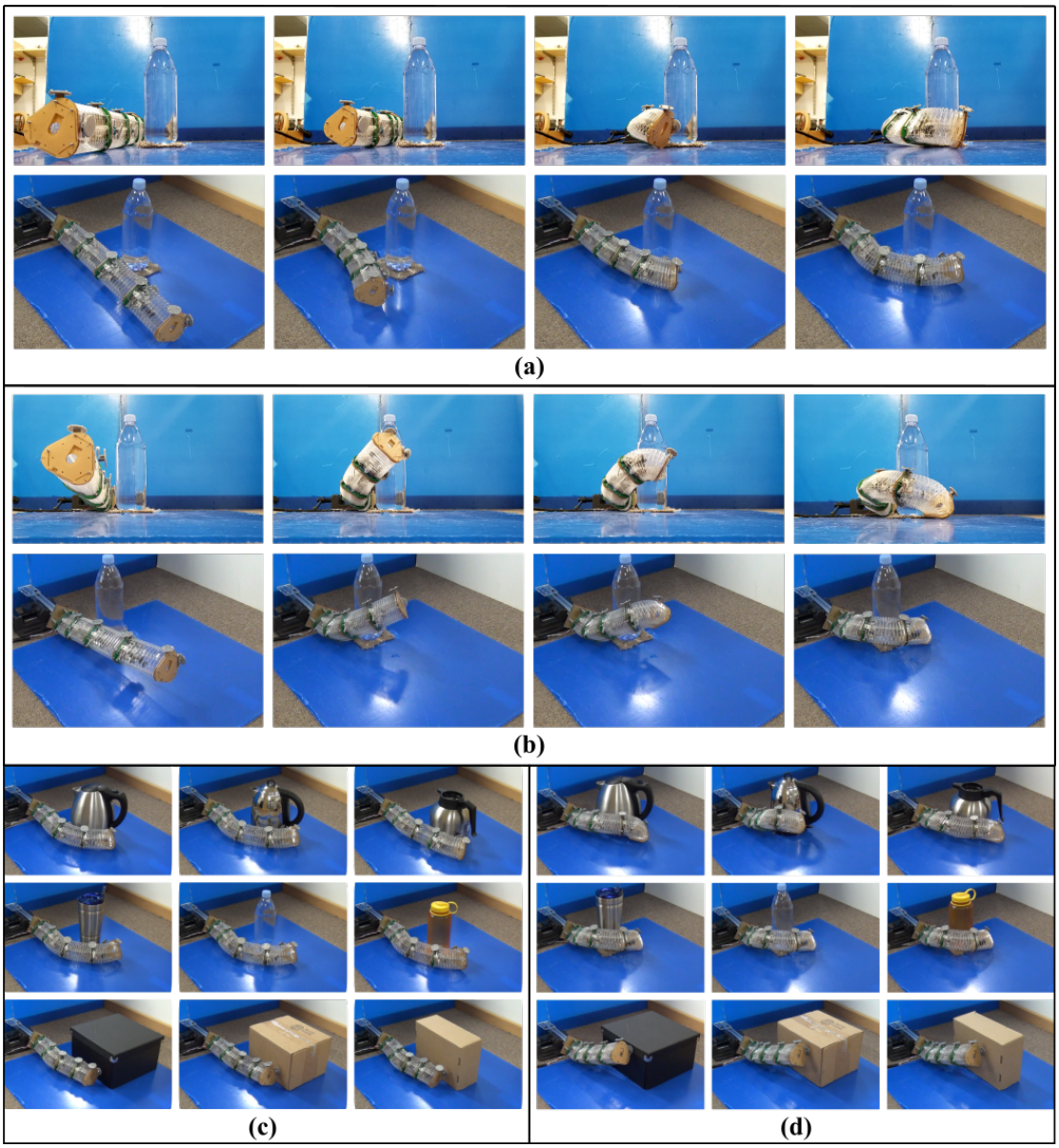

Figure 5.8: The motion snapshots of (a) planar and (b) spatial continuum wraps around the bottle, where the top and bottom rows show the motion of the same wrap from two view angles respectively. (c) Final configurations for the remaining objects with planar wraps. (d) Spatial wrap final configurations.

the wrapping process is terminated. This wrapping configuration is next used for generating the 3-D chords and conducting the final object category classification.

Table 5.2: Object dimension, average number of intermediate configurations to generate one wrap, SVM prediction and its probability using 3 spatial wraps for each object.

Object	dimension(cm)	avg. # of config.	SVM Prediction	Probability
bottle1	$8 \times 8 \times 24$	45	bottle	0.52
bottle2	$9 \times 9 \times 21$	43	teapot	0.56
bottle3	$8 \times 8 \times 21$	40	bottle	0.51
box1	$27 \times 16 \times 26$	12	box	0.74
box2	$25 \times 21 \times 17$	10	box	0.71
box3	$27 \times 10 \times 18$	15	box	0.78
teapot1	$24 \times 18 \times 21$	36	teapot	0.46
teapot2	$21 \times 15 \times 21$	40	teapot	0.51
teapot3	$22 \times 16 \times 16$	38	bottle	0.51

Table 5.2 summarizes the objects used, the average number of robot configurations to generate the wraps, and the SVM prediction results. Overall, the classifier was able to correctly recognize 2 bottles, 3 boxes, and 2 teapots. The boxes are easier to be correctly identified since the robot arm conforms to the side surfaces of the boxes and therefore has distinctive straight sections in contact. The wraps of the bottles and the teapots typically have more curved robot sections but differ in lengths due to their dimensions. The confusion of classifying the bottles and the teapots is because sometimes the handles of the teapots (more distinctive features) are not captured. This can be improved by using longer robot sections and more dense touch sensing.

5.2.9 Experimental Insights

Our results have demonstrated that the shape-based classifier trained solely from simulation is able to generalize to real-world objects. This confirms our two key hypotheses. First, because object clas-

sification is based on the shapes of the continuum arm wrapping around the objects and not the shapes of the objects directly, the classifier has the advantage of avoiding direct sensing and perception of the shape of an unknown target object as well as the associated limitations (such as low object visibility) and all the sensing uncertainties involved that can negatively affect classification accuracy. Second, the continuum wraps generated on objects in the same category have similar shapes, which are captured by the intrinsic parameters of the continuum arm, no matter if the objects wrapped are virtual or real.

Since conducting many real-world continuum wraps would be time-consuming, it is significant that the classifier trained purely in simulation showed considerable effectiveness in classifying real objects. This could make classifier training more efficient and feasible for classifying a large number of categories of real objects from touch-based continuum wrapping.

5.2.10 Future Improvement

The overall system can be improved in multiple ways for better results and robustness. First, soft modules with longer length and more dense touch sensing can help better capture the unique features of the object shapes, for instance, the handles of the teapots. Moreover, more dense touch sensing can also help reduce the cases where the motion planner kept curving the robot sections while the actual contacts are blocking the robot motion. Second, more sophisticated gravity compensation should be considered in order to better lift the robot arm and form spatial wraps around different areas on the objects. Third, since the final robot configuration is the result of both desired motion commands and the contacts with the object, the final shape of the robot can be better identified by equipping robots with proprioceptive sensors and feedback control rather than relying on an external tracking system. The manipulators we built for this study are for object perception purposes and hence have limited payloads. Once the unknown objects are recognized via touch wraps, force-closure continuum grasps can be generated for further manipulation of the objects using the

algorithms in [115]. We would also like to enable handling heavy objects by further improving the robot payloads.

6

Conclusion and Future Research Direction

A complete suite of a continuum robotic platform is presented in this dissertation. The complete system consists of a novel actuator, sensing methodology, and motion planning algorithms. The proposed continuum module utilizes a compliant origami structure and is capable of resisting a significant torsional load. The electrically driven actuator provides an advantage in a specific domain compared to pneumatic driven actuators e.g. outer space application due to the limited amount of available air. Furthermore, a more deployable system can be achieved through the use of batteries as the power source. The single module's performance is first evaluated before it is implemented in a multi-segment manipulator. Through a comparison with the state of the art for continuum robots listed in Table 6.1 we claim that our origami continuum module possesses both high compression ratio and torsional stiffness while also being light-weight (See Appendix A.1 for the more complete

Table 6.1: List of the current state of the art continuum robots. Act. column indicates the actuation method: Pneumatic (P), Tendon (T), Hybrid (H), Vacuum (V). The weight information is approximately calculated when not directly provided by the research papers and only includes the bending/compliant parts. Some loading capability information is missing (N/A) and highly dependent on the actuator specifications e.g. motor rated torque. Arch. column indicates the robot actuation architecture: centralized (cent.) vs modularized (modular.). Ext. column indicates the robot extensibility, missing information means that the robot is inextensible.

Literature	**Act.**	**Wgt. (g)**	**Load. cap. (N)**	**Max. bend. (deg)**	**Arch.**	**Ext. (%)**	**Tor. stiff. (Nm/rad)**
Jones et al. (2005)	H	94.4	N/A	180	Cent.	246.2	N/A
McMahan et al. (2006)	P	1034.9	80	90-180	Cent.	60-75	N/A
Srinivas et al. (2007)	H	231.2	N/A	227.7	Cent.	34	N/A
Mahl et al. (2014)	P	1250	4.9	N/A	Cent.	46.7	N/A
Marchese et al. (2015)	P	600	0.75	40	Cent.	-	N/A
Zhang et al. (2016)	T	5.9	N/A	> 180	Cent.	100	N/A
Qi et al. (2016)	T	10	N/A	160	Cent.	43	0.37
Dong et al. (2016)	T	62	4.4	90	Cent.	-	48.55
Jiang et al. (2016)	P	1500	2.8	30	Cent.	64.5	N/A
Robertson et al. (2017)	V	11.1	0.9	27.3	Modular.	-	N/A
Jeong et al. (2018)	T	358.3	11.1	185	Cent.	60	N/A
Our approach	**T**	**48**	**4.9**	**95.5**	**Modular.**	**125**	**25.67**

table). Although the work by Dong et al. possesses much higher torsional stiffness, it is not extensible in contrast to the work presented in this work. Furthermore, the actuation system at the base is significantly larger than its cylindrical compliant arm. Note that, some information regarding the actuator weight of the other continuum robots is missing thus it is possible for them to be significantly heavier than our continuum robot (135 gram for each module).

We developed and implemented an optimization-based inverse kinematics solver to achieve smoothness-preserving motions of a multi-segment continuum manipulator. This allows for similar solving time and tracking performance compared to the commonly used gradient descent method, without the need for fine-tuning the damping coefficient. Furthermore, we achieved a task-space control of the manipulator using a kinematic model and further reduced the error by introducing sensor feedback. Additionally, a heuristic, grow-to-shape algorithm is proposed to allow for continuum robot navigation in a constrained environment. Additionally, the robot's capabilities in

various applications including pick and place, search and rescue, and robotic painting, are showcasing this work's potential for field deployment and collaborative research. Lastly, we present a preliminary evaluation of an embedded proprioceptive sensor for the robot.

Additional work is required before the system can be reliably deployed. For instance, the sensor model requires integration into the controller board to achieve closed-loop control independently of an external sensing architecture. Dynamic control would be the next step in achieving predictable robot behavior. This has not been the focus of my dissertation work because the robot is not yet capable of direct torque and force control. The use of a gearbox and a brushed motor for actuation makes it difficult to achieve a clean and reliable measurement of motor current. A brushless motor would be better for this purpose but it requires more complex circuitry and control signals. Nevertheless, we have shown the robot's capability achieved only with kinematic control. It is also expected that the addition of a proprioceptive sensor would improve the performance further.

Future research directions could be to explore different morphology of the origami structure to possibly achieve optimal actuator operation e.g. investigating the effect of increasing the number of edges to approximate the cylindrical shape of the actuator. A tapered version of the origami structure, which more closely resembles octopus arms or an elephant trunk, could also be explored. The tapered structure would likely require a non-constant curvature model even on the absence of an external load. Moreover, the origami module's compliant behavior under compression could be considered as a double-edged sword. On the one hand, the inherent compliance allows for constantly safe interaction between the robot and its environment; on the other hand, the compliance also restricts manipulation tasks that require pushing action from the robot. A more robust solution would allow for controllable stiffness. Depending on the intended applications, a solution can be devised so that the robot can be either inherently compliant or stiff when activated and vice versa when not actuated. A possible solution is to incorporate a locking or jamming mechanism into the origami structure to prevent any deformation when not intended. Another possibility is to incor-

porate stiffness into the actuation method as the current tendon-driven system is only stiff under tension.

Investigation of the whole-arm grasping capability would also be beneficial as it would provide a new method of manipulation and further validate the effectiveness of torsional stiffness against an offset load. Assistive bi-manual manipulation research is also of interest in which the continuum manipulator can be used as a stowable third "helping" hand to improve productivity and enable multitasking. Other human-limb augmentations such as a self-balancing tail are worth exploring as well. To conclude, I believe the research work laid out in this dissertation can be a stepping stone for further research related to manipulation, safe human-robot collaboration, and numerous bio-inspired robotic applications.

Table A.1: List of the current state of the art continuum robots. The dimension information (diameter × length) is only for a single segment. The weight information is approximately calculated when not directly provided by the research papers and only includes the bending/compliant parts. Some loading capability information is missing (N/A) and highly dependent on the actuator specifications e.g. motor rated torque. Arch. column indicates the robot actuation architecture: centralized (cent.) vs modularized (modular.). Ext. column indicates the robot extensibility, missing information means that the robot is inextensible. No of segment column indicates the number of robot segments which have been successfully connected in the corresponding publications. This does not imply the maximum number of segments that can be connected.

Literature	**Actuation Method**	**Dimension (cm) [Diam. × Len.]**	**Weight (g)**	**Load. cap. (N)**	**Max. bend. (deg)**	**Arch.**	**Ext. (%)**	**Tor. stiff. (Nm/rad)**	**No of segment**
Jones et al. (2005)	Hybrid	9 × 13	94.4	N/A	180	Cent.	246.2	N/A	2
McMahan et al. (2006)	Pneumatic	8.4 × 25	1034.9	80	90-180	Cent.	60-75	N/A	3
Srinivas et al. (2007)	Hybrid	2.8 × 64	231.2	N/A	227.7	Cent.	34	N/A	1
Mahl et al. (2014)	Pneumatic	27 × 75	1250	4.9	N/A	Cent.	46.7	N/A	4
Marchese et al. (2015)	Pneumatic	5 × 50	600	0.75	40	Cent.	-	N/A	1
Zhang et al. (2016)	Tendon	2.3 × 12	5.9	N/A	> 180	Cent.	100	N/A	1
Qi et al. (2016)	Tendon	2.9 × 14.3	10	N/A	160	Cent.	43	0.37	3
Dong et al. (2016)	Tendon	1.5 × 10	62	4.4	90	Cent.	-	48.55	1
Jiang et al. (2016)	Pneumatic	7 × 63	1500	2.8	30	Cent.	64.5	N/A	3
Robertson et al. (2017)	Vacuum	4.5 × 4.5	11.1	0.9	27.3	Modular.	-	N/A	5
Jeong et al. (2018)	Tendon	9 × 25.4	358.3	11.1	185	Cent.	60	N/A	5
Our approach	**Tendon**	**8 × 18**	**48**	**4.9**	**95.5**	**Modular.**	**125**	**25.67**	**3**

References

[1] S. Li, D. M. Vogt, D. Rus, R. J. Wood, Fluid-driven origami-inspired artificial muscles. *Proceedings of the National academy of Sciences* **114**, 13132–13137 (2017).

[2] R. F. Shepherd, A. A. Stokes, R. M. Nunes, G. M. Whitesides, Soft machines that are resistant to puncture and that self seal. *Advanced Materials* **25**, 6709–6713 (2013).

[3] E. J. Markvicka, M. D. Bartlett, X. Huang, C. Majidi, An autonomously electrically self-healing liquid metal–elastomer composite for robust soft-matter robotics and electronics. *Nature materials* **17**, 618 (2018).

[4] M. W. Hannan, I. D. Walker, Kinematics and the implementation of an elephant's trunk manipulator and other continuum style robots. *Journal of robotic systems* **20**, 45–63 (2003).

[5] W. S. Rone, P. Ben-Tzvi, Mechanics modeling of multisegment rod-driven continuum robots. *Journal of Mechanisms and Robotics* **6**, 041006 (2014).

[6] R. J. Roesthuis, S. Misra, Steering of multisegment continuum manipulators using rigid-link modeling and fbg-based shape sensing. *IEEE transactions on robotics* **32**, 372–382 (2016).

[7] I. S. Godage, G. A. Medrano-Cerda, D. T. Branson, E. Guglielmino, D. G. Caldwell, Dynamics for variable length multisection continuum arms. *The International Journal of Robotics Research* **35**, 695–722 (2016).

[8] S. Neppalli, B. A. Jones, in *2007 IEEE/RSJ International Conference on Intelligent Robots and Systems* (IEEE, 2007), pp. 1503–1507.

[9] R. Xu, A. Yurkewich, R. V. Patel, Curvature, torsion, and force sensing in continuum robots using helically wrapped fbg sensors. *IEEE Robotics and Automation Letters* **1**, 1052–1059 (2016).

[10] K. K. Smith, Trunks, tonques, and tentacles: moving with skeletons of muscle. *Am. Scientist* **77**, 28–35 (1989).

[11] S. Sanan, P. S. Lynn, S. T. Griffith, Pneumatic torsional actuators for inflatable robots. *Journal of Mechanisms and Robotics* **6**, 031003 (2014).

[12] G. Olson, Y. Mengüç, in *2018 IEEE International Conference on Soft Robotics (RoboSoft)* (IEEE, 2018), pp. 214–221.

[13] J. Yan, X. Zhang, B. Xu, J. Zhao, A new spiral-type inflatable pure torsional soft actuator. *Soft robotics* **5**, 527–540 (2018).

[14] W. McMahan, V. Chitrakaran, M. Csencsits, D. Dawson, I. D. Walker, B. A. Jones, M. Pritts, D. Dienno, M. Grissom, C. D. Rahn, in *Proceedings 2006 IEEE International Conference on Robotics and Automation, 2006. ICRA 2006.* (2006), pp. 2336–2341.

[15] F. Corporation, Bionic handling assistant (2011).

[16] A. Grzesiak, R. Becker, A. Verl, The bionic handling assistant: a success story of additive manufacturing. *Assembly Automation* **31**, 329–333 (2011).

[17] T. Mahl, A. Hildebrandt, O. Sawodny, A variable curvature continuum kinematics for kinematic control of the bionic handling assistant. *IEEE Transactions on Robotics* **30**, 935–949 (2014).

[18] A. D. Marchese, D. Rus, Design, kinematics, and control of a soft spatial fluidic elastomer manipulator. *The International Journal of Robotics Research* **35**, 840–869 (2016).

[19] H. Jiang, X. Liu, X. Chen, Z. Wang, Y. Jin, X. Chen, in *2016 IEEE International Conference on Robotics and Biomimetics (ROBIO)* (IEEE, 2016), pp. 350–356.

[20] F. Renda, M. Cianchetti, M. Giorelli, A. Arienti, C. Laschi, A 3d steady-state model of a tendon-driven continuum soft manipulator inspired by the octopus arm. *Bioinspiration & biomimetics* **7**, 025006 (2012).

[21] D. J. Zhang K, Qiu C, An extensible continuum robot with integrated origami parallel modules. *Journal of Mechanisms and Robotics* **8**, 0310010 (2016).

[22] P. Qi, C. Qiu, H. Liu, J. S. Dai, L. D. Seneviratne, K. Althoefer, A novel continuum manipulator design using serially connected double-layer planar springs. *IEEE/ASME Transactions on Mechatronics* **21**, 1281-1292 (2016).

[23] D. Jeong, K. Lee, Design and analysis of an origami-based three-finger manipulator. *Robotica* **36**, 261–274 (2018).

[24] W. McMahan, B. A. Jones, I. D. Walker, in *2005 IEEE/RSJ International Conference on Intelligent Robots and Systems* (IEEE, 2005), pp. 2578–2585.

[25] M. Cianchetti, M. Follador, B. Mazzolai, P. Dario, C. Laschi, in *2012 IEEE International Conference on Robotics and Automation* (IEEE, 2012), pp. 5271–5276.

[26] M. A. Robertson, J. Paik, New soft robots really suck: Vacuum-powered systems empower diverse capabilities. *Science Robotics* **2**, eaan6357 (2017).

[27] E. D. Demaine, T. Tachi, in *33rd International Symposium on Computational Geometry (SoCG 2017)* (Schloss Dagstuhl-Leibniz-Zentrum fuer Informatik, 2017).

[28] S. A. Zirbel, R. J. Lang, M. W. Thomson, D. A. Sigel, P. E. Walkemeyer, B. P. Trease, S. P. Magleby, L. L. Howell, Accommodating thickness in origami-based deployable arrays. *Journal of Mechanical Design* **135**, 111005 (2013).

[29] P. W. Rothemund, Folding dna to create nanoscale shapes and patterns. *Nature* **440**, 297 (2006).

[30] K. Kuribayashi, K. Tsuchiya, Z. You, D. Tomus, M. Umemoto, T. Ito, M. Sasaki, Self-deployable origami stent grafts as a biomedical application of ni-rich tini shape memory alloy foil. *Materials Science and Engineering: A* **419**, 131–137 (2006).

[31] J. K. Paik, A. Byoungkwon, D. Rus, R. J. Wood, in *ICMC*, no. CONF (2012).

[32] J. Paik, Reconfigurable materials: Algorithm for architectural origami. *Nature* **541**, 296 (2017).

[33] J.-L. Huang, Z. Zhakypov, H. Sonar, J. Paik, A reconfigurable interactive interface for controlling robotic origami in virtual environments. *The International Journal of Robotics Research* **37**, 629–647 (2018).

[34] Z. Zhakypov, F. Heremans, A. Billard, J. Paik, An origami-inspired reconfigurable suction gripper for picking objects with variable shape and size. *IEEE Robotics and Automation Letters* **3**, 2894–2901 (2018).

[35] T. G. Nelson, R. J. Lang, N. A. Pehrson, S. P. Magleby, L. L. Howell, Facilitating deployable mechanisms and structures via developable lamina emergent arrays. *Journal of Mechanisms and Robotics* **8**, 031006 (2016).

[36] R. J. Lang, S. Magleby, L. Howell, Single degree-of-freedom rigidly foldable cut origami flashers. *Journal of Mechanisms and Robotics* **8**, 031005 (2016).

[37] S. Miyashita, S. Guitron, M. Ludersdorfer, C. R. Sung, D. Rus, in *Proceedings of the 2015 IEEE International Conference on Robotics and Automation (ICRA)* (IEEE, 2015), pp. 1490–1496.

[38] J. Morgan, S. P. Magleby, L. L. Howell, An approach to designing origami-adapted aerospace mechanisms. *Journal of Mechanical Design* **138**, 052301 (2016).

[39] S.-J. Kim, D.-Y. Lee, G.-P. Jung, K.-J. Cho, An origami-inspired, self-locking robotic arm that can be folded flat. *Science Robotics* **3**, eaar2915 (2018).

[40] A. T. Baisch, O. Ozcan, B. Goldberg, D. Ithier, R. J. Wood, High speed locomotion for a quadrupedal microrobot. *The International Journal of Robotics Research* **33**, 1063–1082 (2014).

[41] S. G. Faal, F. Chen, W. Tao, M. Agheli, S. Tasdighikalat, C. D. Onal, Hierarchical kinematic design of foldable hexapedal locomotion platforms. *JMR* **3**, 1 (2015).

[42] D. Rus, M. T. Tolley, Design, fabrication and control of origami robots. *Nature Reviews Materials* **3**, 101 (2018).

[43] J. Santoso, E. H. Skorina, M. Luo, R. Yan, C. D. Onal, in *Proceedings of the 2017 IEEE/RSJ International Conference on Intelligent Robots and Systems (IROS)* (IEEE, 2017), pp. 2098–2104.

[44] M. Cianchetti, T. Ranzani, G. Gerboni, T. Nanayakkara, K. Althoefer, P. Dasgupta, A. Menciassi, Soft robotics technologies to address shortcomings in today's minimally invasive surgery: the stiff-flop approach. *Soft Robotics* **1**, 122–131 (2014).

[45] P. Polygerinos, Z. Wang, K. C. Galloway, R. J. Wood, C. J. Walsh, Soft robotic glove for combined assistance and at-home rehabilitation. *Robotics and Autonomous Systems* **73**, 135–143 (2015).

[46] M. T. Tolley, R. F. Shepherd, B. Mosadegh, K. C. Galloway, M. Wehner, M. Karpelson, R. J. Wood, G. M. Whitesides, A resilient, untethered soft robot. *Soft Robotics* **1**, 213–223 (2014).

[47] C. Laschi, B. Mazzolai, M. Cianchetti, Soft robotics: Technologies and systems pushing the boundaries of robot abilities. *Science Robotics* **1**, eaah3690 (2016).

[48] M. Cianchetti, C. Laschi, A. Menciassi, P. Dario, Biomedical applications of soft robotics. *Nature Reviews Materials* **3**, 143 (2018).

[49] D. Trivedi, D. Dienno, C. D. Rahn, Optimal, model-based design of soft robotic manipulators. *Journal of Mechanical Design* **130**, 091402 (2008).

[50] T.-D. Nguyen, J. Burgner-Kahrs, in *2015 IEEE/RSJ International Conference on Intelligent Robots and Systems (IROS)* (IEEE, 2015), pp. 2130–2135.

[51] E. Vander Hoff, D. Jeong, K. Lee, in *Proceedings of the 2014 IEEE/RSJ International Conference on Intelligent Robots and Systems* (IEEE, 2014), pp. 1421–1426.

[52] M. Follador, M. Cianchetti, C. Laschi, in *Proceedings of the 2012 4th IEEE RAS & EMBS International Conference on Biomedical Robotics and Biomechatronics (BioRob)* (IEEE, 2012), pp. 640–645.

[53] J. H. Crews, G. D. Buckner, Design optimization of a shape memory alloy–actuated robotic catheter. *Journal of Intelligent Material Systems and Structures* **23**, 545–562 (2012).

[54] C. Laschi, M. Cianchetti, B. Mazzolai, L. Margheri, M. Follador, P. Dario, Soft robot arm inspired by the octopus. *Advanced Robotics* **26**, 709–727 (2012).

[55] R. J. Webster, B. A. Jones, Design and kinematic modeling of constant curvature continuum robots: A review. *The International Journal of Robotics Research* (2010).

[56] E. W. Hawkes, L. H. Blumenschein, J. D. Greer, A. M. Okamura, A soft robot that navigates its environment through growth. *Science Robotics* **2**, eaan3028 (2017).

[57] G. Gerboni, T. Ranzani, A. Diodato, G. Ciuti, M. Cianchetti, A. Menciassi, Modular soft mechatronic manipulator for minimally invasive surgery (mis): overall architecture and development of a fully integrated soft module. *Meccanica* **50**, 2865–2878 (2015).

[58] T. Ranzani, M. Cianchetti, G. Gerboni, I. De Falco, A. Menciassi, A soft modular manipulator for minimally invasive surgery: design and characterization of a single module. *IEEE Transactions on Robotics* **32**, 187–200 (2016).

[59] M. Luo, E. H. Skorina, W. Tao, F. Chen, S. Ozel, Y. Sun, C. D. Onal, Toward modular soft robotics: Proprioceptive curvature sensing and sliding-mode control of soft bidirectional bending modules. *Soft Robotics* **4**, 117–125 (2017).

[60] P. Corporation, Micro metal gearmotors (2019).

[61] C. D. Onal, R. J. Wood, D. Rus, An origami-inspired approach to worm robots. *IEEE/ASME Transactions on Mechatronics* **18**, 430–438 (2013).

[62] C. D. Onal, M. T. Tolley, R. J. Wood, D. Rus, Origami-inspired printed robots. *IEEE/ASME Transactions on Mechatronics* **20**, 2214-2221 (2015).

[63] B. A. Jones, I. D. Walker, Practical kinematics for real-time implementation of continuum robots. *IEEE Transactions on Robotics* **22**, 1087–1099 (2006).

[64] I. S. Godage, G. A. Medrano-Cerda, D. T. Branson, E. Guglielmino, D. G. Caldwell, Modal kinematics for multisection continuum arms. *Bioinspiration & Biomimetics* **10**, 035002 (2015).

[65] B. A. Jones, I. D. Walker, Kinematics for multisection continuum robots. *IEEE Transactions on Robotics* **22**, 43–55 (2006).

[66] S. Neppalli, M. A. Csencsits, B. A. Jones, I. D. Walker, Closed-form inverse kinematics for continuum manipulators. *Advanced Robotics* **23**, 2077–2091 (2009).

[67] T. G. Thuruthel, E. Falotico, M. Cianchetti, C. Laschi, in *Proceedings of the Symposium on Robot Design, Dynamics and Control* (Springer, 2016), pp. 47–54.

[68] O. Lakhal, A. Melingui, A. Chibani, C. Escande, R. Merzouki, in *Proceedings of the 2014 IEEE/ASME International Conference on Advanced Intelligent Mechatronics* (IEEE, 2014), pp. 1337–1342.

[69] I. Singh, O. Lakhal, Y. Amara, V. Coelen, P. M. Pathak, R. Merzouki, in *Proceedings of the 2017 IEEE International Conference on Robotics and Biomimetics (ROBIO)* (IEEE, 2017), pp. 264–269.

[70] H. Choset, W. Henning, A follow-the-leader approach to serpentine robot motion planning. *Journal of Aerospace Engineering* **12**, 65–73 (1999).

[71] H. B. Gilbert, J. Neimat, R. J. Webster, Concentric tube robots as steerable needles: Achieving follow-the-leader deployment. *IEEE Transactions on Robotics* **31**, 246–258 (2015).

[72] D. Palmer, S. Cobos-Guzman, D. Axinte, Real-time method for tip following navigation of continuum snake arm robots. *Robotics and Autonomous Systems* **62**, 1478–1485 (2014).

[73] M. Neumann, J. Burgner-Kahrs, in *Proceedings of the 2016 IEEE International Conference on Robotics and Automation (ICRA)* (IEEE, 2016), pp. 917–923.

[74] B. Kang, R. Kojcev, E. Sinibaldi, The first interlaced continuum robot, devised to intrinsically follow the leader. *PlOS One* **11**, e0150278 (2016).

[75] Y. Qin, Z. Wan, Y. Sun, E. H. Skorina, M. Luo, C. D. Onal, in *Proceedings of the 2018 IEEE International Conference on Soft Robotics (RoboSoft)* (IEEE, 2018), pp. 77–82.

[76] P. Qi, C. Qiu, H. Liu, J. S. Dai, L. D. Seneviratne, K. Althoefer, A novel continuum manipulator design using serially connected double-layer planar springs. *IEEE/ASME Transactions on Mechatronics* **21**, 1281–1292 (2015).

[77] S. Chiaverini, B. Siciliano, O. Egeland, Review of the damped least-squares inverse kinematics with experiments on an industrial robot manipulator. *IEEE Transactions on Control Systems Technology* **2**, 123–134 (1994).

[78] Y. Chen, J. M. Oliveira, I. W. Hunter, in *2013 IEEE International Conference on Robotics and Automation* (IEEE, 2013), pp. 704–710.

[79] K. Elgeneidy, N. Lohse, M. Jackson, Bending angle prediction and control of soft pneumatic actuators with embedded flex sensors–a data-driven approach. *Mechatronics* **50**, 234–247 (2018).

[80] C. Lucarotti, M. Totaro, A. Sadeghi, B. Mazzolai, L. Beccai, Revealing bending and force in a soft body through a plant root inspired approach. *Scientific reports* **5**, 8788 (2015).

[81] M. C. Yuen, H. Tonoyan, E. L. White, M. Telleria, R. K. Kramer, in *2017 IEEE international conference on robotics and automation (ICRA)* (IEEE, 2017), pp. 5511–5518.

[82] W. Felt, M. J. Telleria, T. F. Allen, G. Hein, J. B. Pompa, K. Albert, C. D. Remy, An inductance-based sensing system for bellows-driven continuum joints in soft robots. *Autonomous robots* **43**, 435–448 (2019).

[83] I. Van Meerbeek, C. De Sa, R. Shepherd, Soft optoelectronic sensory foams with proprioception. *Science Robotics* **3**, eaau2489 (2018).

[84] H. Liu, A. Farvardin, R. Grupp, R. J. Murphy, R. H. Taylor, I. Iordachita, M. Armand, Shape tracking of a dexterous continuum manipulator utilizing two large deflection shape sensors. *IEEE sensors journal* **15**, 5494–5503 (2015).

[85] S. Ozel, N. A. Keskin, D. Khea, C. D. Onal, A precise embedded curvature sensor module for soft-bodied robots. *Sensors and Actuators A: Physical* **236**, 349–356 (2015).

[86] S. Ozel, E. H. Skorina, M. Luo, W. Tao, F. Chen, Y. Pan, C. D. Onal, in *2016 IEEE International Conference on Robotics and Automation (ICRA)* (IEEE, 2016), pp. 4963–4968.

[87] S. Song, Z. Li, M. Q.-H. Meng, H. Yu, H. Ren, Real-time shape estimation for wire-driven flexible robots with multiple bending sections based on quadratic bézier curves. *IEEE Sensors Journal* **15**, 6326–6334 (2015).

[88] S. Song, Z. Li, H. Yu, H. Ren, Shape reconstruction for wire-driven flexible robots based on bézier curve and electromagnetic positioning. *Mechatronics* **29**, 28–35 (2015).

[89] D. B. Camarillo, K. E. Loewke, C. R. Carlson, J. K. Salisbury, in *2008 IEEE International Conference on Robotics and Automation* (IEEE, 2008), pp. 2940–2947.

[90] A. Reiter, A. Bajo, K. Iliopoulos, N. Simaan, P. K. Allen, in *2012 4th IEEE RAS & EMBS International Conference on Biomedical Robotics and Biomechatronics (BioRob)* (IEEE, 2012), pp. 829–834.

[91] R. Wang, S. Wang, E. Xiao, K. Jindal, W. Yuan, C. Feng, Real-time soft robot 3d proprioception via deep vision-based sensing. *arXiv preprint arXiv:1904.03820* (2019).

[92] H. Wang, M. Totaro, L. Beccai, Toward perceptive soft robots: Progress and challenges. *Advanced Science* **5**, 1800541 (2018).

[93] G. Soter, A. Conn, H. Hauser, J. Rossiter, in *2018 IEEE international conference on robotics and automation (ICRA)* (IEEE, 2018), pp. 2448–2453.

[94] T. G. Thuruthel, B. Shih, C. Laschi, M. T. Tolley, Soft robot perception using embedded soft sensors and recurrent neural networks. *Science Robotics* **4**, eaav1488 (2019).

[95] F. Burden, D. Winkler, in *Artificial neural networks* (Springer, 2008), pp. 23–42.

[96] M. Luo, R. Yan, Z. Wan, Y. Qin, J. Santoso, E. H. Skorina, C. D. Onal, Orisnake: Design, fabrication, and experimental analysis of a 3-d origami snake robot. *IEEE Robotics and Automation Letters* **3**, 1993–1999 (2018).

[97] H. Mao, J. Santoso, C. Onal, J. Xiao, in *International Symposium on Experimental Robotics (ISER) 2018* (2018).

[98] C. Wright, A. Johnson, A. Peck, Z. McCord, A. Naaktgeboren, P. Gianfortoni, M. Gonzalez-Rivero, R. Hatton, H. Choset, in *2007 IEEE/RSJ International Conference on Intelligent Robots and Systems* (IEEE, 2007), pp. 2609–2614.

[99] A. Crespi, A. J. Ijspeert, in *Proceedings of the 9th international conference on climbing and walking robots (CLAWAR 2006)* (2006), pp. 19–27.

[100] S. Hirose, M. Mori, in *2004 IEEE International Conference on Robotics and Biomimetics* (IEEE, 2004), pp. 1–7.

[101] F. Matsuno, K. Suenaga, in *2003 IEEE International Conference on Robotics and Automation (Cat. No. 03CH37422)* (IEEE, 2003), vol. 2, pp. 2061–2066.

[102] K. L. Paap, T. Christaller, F. Kirchner, in *Proceedings. 2000 IEEE/RSJ International Conference on Intelligent Robots and Systems (IROS 2000)(Cat. No. 00CH37113)* (IEEE, 2000), vol. 3, pp. 2079–2082.

[103] Z. Bing, L. Cheng, G. Chen, F. Röhrbein, K. Huang, A. Knoll, Towards autonomous locomotion: Cpg-based control of smooth 3d slithering gait transition of a snake-like robot. *Bioinspiration & biomimetics* **12**, 035001 (2017).

[104] P. Liljebäck, K. Y. Pettersen, Ø. Stavdahl, J. T. Gravdahl, *Snake robots: modelling, mechatronics, and control* (Springer Science & Business Media, 2012).

[105] S. Ma, N. Tadokoro, B. Li, K. Inoue, in *2003 IEEE International Conference on Robotics and Automation (Cat. No. 03CH37422)* (IEEE, 2003), vol. 2, pp. 2073–2078.

[106] C. D. Onal, D. Rus, Autonomous undulatory serpentine locomotion utilizing body dynamics of a fluidic soft robot. *Bioinspiration & biomimetics* **8**, 026003 (2013).

[107] M. Luo, Y. Pan, E. H. Skorina, W. Tao, F. Chen, S. Ozel, C. D. Onal, Slithering towards autonomy: a self-contained soft robotic snake platform with integrated curvature sensing. *Bioinspiration & biomimetics* **10**, 055001 (2015).

[108] M. M. Zhang, N. Atanasov, K. Daniilidis, in *IEEE/RSJ International Conference on Intelligent Robots and Systems (IROS)* (2017).

[109] N. Sommer, M. Li, A. Billard, in *International Conference on Robotics and Automation (ICRA)* (IEEE, 2014).

[110] Q. Li, C. Schürmann, R. Haschke, H. J. Ritter, in *Robotics: Science and systems* (2013).

[111] Z. Yi, R. Calandra, F. Veiga, H. van Hoof, T. Hermans, Y. Zhang, J. Peters, in *IEEE/RSJ IROS* (2016).

[112] Y.-B. Jia, J. Tian, Surface patch reconstruction from one-dimensional tactile data. *IEEE Transactions on Automation Science and Engineering* **7(2)** (2010).

[113] H. Mao, J. Xiao, in *International Symposium of Robotics Research(ISRR)* (2017).

[114] P. Falco, S. Lu, A. Cirillo, C. Natale, S. Pirozzi, D. Lee, in *IEEE ICRA* (2017).

[115] J. Li, J. Xiao, Progressive planning of continuum grasping in cluttered space. *IEEE Transactions on Robotics(TRO)* **32(3)** (2016).

[116] H. Mao, J. Xiao, M. M. Zhang, K. Daniilidis, in *2017 IEEE/RSJ International Conference on Intelligent Robots and Systems (IROS)* (IEEE, 2017), pp. 456–463.

[117] A. Bajo, N. Simaan, Kinematics-based detection and localization of contacts along multisegment continuum robots. *IEEE TRO* **28(2)** (2012).